

IMPROVING THE SELECTIVITY OF HIGH PRESSURE MASS SPECTROMETRY

Andrew Hampton

A dissertation submitted to the faculty at the University of North Carolina at Chapel Hill in partial fulfillment of the requirements for the degree of Doctor of Philosophy in the Department of Chemistry.

Chapel Hill
2016

Approved By:

J. Michael Ramsey

James Jorgenson

Leslie Hicks

Joanna Atkin

Elias Rosen

©2016
Andrew Hampton
ALL RIGHTS RESERVED

ABSTRACT

Andrew Hampton: Improving the Selectivity of High Pressure Mass Spectrometry
(Under the direction of J. Michael Ramsey)

This work describes several strategies for improving the selectivity of high pressure mass spectrometry (HPMS). HPMS is the central strategy for developing hand portable MS instrumentation, which is useful in many field applications including rapid threat detection. A drawback to operating at high pressures is a degradation of resolution, adversely affecting selectivity. Improving resolution and selectivity at high pressures would further advance the field of HPMS. The focus of this work was incorporating tandem mass spectrometry (MS/MS) in a HPMS system and also demonstrating the feasibility of coupling HPMS with gas chromatography (GC).

Tandem MS requires ion isolation and fragmentation, followed by mass analysis and detection. Initial work studied the behavior of trapped ions at high pressures (~1 Torr). Stability regions were measured at high and low pressures. Mass windows were found to be smaller at 1 mTorr, but the overall regions were generally steady from 500–1500 mTorr. Higher pressures dampened resonant behavior, thus requiring higher voltages to effect resonant ejection. Also, to improve the sensitivity of a high pressure system, two strategies were tested for creating differentiated sites for ion injection and ejection. The tapered SLIT geometry was shown to affect ion location, but adding supplemental electrodes between the ring and endcaps was demonstrated as a much more effective strategy for controlling ions.

Ion isolation was demonstrated at 1 Torr of air via apex isolation, multifrequency isolation, and partial instability scan isolation. Fragmentation via high pressure collision-induced dissociation (HPCID) was demonstrated for several compounds. To maximize the CID efficiency, several variables were investigated. Increasing drive RF frequency was shown to be beneficial over the range tested (up to 25 MHz). Reductions in trap size, as expected, lowered pseudopotential well depth and hindered conversion efficiency. Increased pressure improved conversion efficiency, as did the use of air instead of helium.

The coupling of GC to HPMS was also demonstrated with both helium and nitrogen carrier gases. A complex mixture of six chemical warfare agent simulants, which was unidentifiable with only a HPMS system, was separated and detected.

ACKNOWLEDGEMENTS

I would like to thank my advisor, J. Michael Ramsey, for the opportunities and experiences I have had while studying in his lab. His guidance and support have been critical throughout my research. The entire Ramsey group has fostered an environment for challenging intellectual discussions while also becoming friends. My time with the Caudill subgroup has been well appreciated, as I have learned much both scientifically and personally from everyone involved. This dissertation itself is only possible with the gracious help and patient editing from J.P. Alarie and Tina Stacy. My friends and family also deserve recognition for their invaluable advice and support.

TABLE OF CONTENTS

List of Figures	ix
List of Tables	xii
List of Abbreviations and Symbols	xiii
1 Introduction	1
1.1 Chemical Warfare Agents and Other Critical Threats.....	3
1.2 Quadrupole Ion Traps.....	5
1.3 Tandem Mass Spectrometry.....	11
1.4 High Pressure Mass Spectrometry.....	16
1.5 Objectives.....	21
1.6 Figures.....	23
1.7 References.....	30
2 Trapped Ion Behavior at High Pressures	37
2.1 Introduction.....	37
2.2 Stability Diagram Analysis.....	38
2.2.1 Instrumental Design.....	42

2.2.2 Pressure Effects on Stability Regions	45
2.2.3 Characterizing the Stability Regions of SLITs	50
2.3 Resonant Ejection Behavior Analysis.....	51
2.4 Conclusions.....	55
2.5 Figures.....	57
2.5 Figures.....	72
3 Ion Manipulation in High Pressure Ion Traps.....	76
3.1 Introduction.....	76
3.2 Spatial Control of Ion Ejection from SLITs	78
3.2.1 Tapered SLIT Geometry	80
3.2.2 Supplementary Electrode SLIT Geometry.....	83
3.3 Targeted Ion Isolation	86
3.3.1 Apex Isolation.....	88
3.3.2 Multifrequency Isolation.....	88
3.3.3 Partial Instability Scan Isolation	90
3.4 Collision-Induced Dissociation in HPMS.....	90
3.5 Conclusions.....	95
3.6 Figures.....	97

3.7 References.....	115
4 Improving the Selectivity of High Pressure Mass Spectrometry.....	118
4.1 Introduction.....	118
4.2 Improving CID Efficiency	119
4.2.1 Role of Pseudopotential Well Depth.....	121
4.2.2 Role of Pressure	127
4.2.3 Role of Buffer Gas	131
4.3 Gas Chromatography – High Pressure Mass Spectrometry.....	133
4.4 Conclusions.....	136
4.5 Tables & Figures.....	138
4.6 References.....	149
5 Conclusions and Future Directions	152
5.1 Conclusions.....	152
5.2 Future Directions	155
5.3 References.....	159

LIST OF FIGURES

1.1	Chart of chemical warfare agents	23
1.2	Electrodes in a hyperbolic geometry.....	24
1.3	Theoretical stability diagram.	25
1.4	Detailed stability area	26
1.5	Triple quadrupole instrumentation.....	27
1.6	Isopotential lines resulting from electrodes	28
1.7	CIT electrodes and SLIT electrodes	29
2.1	Detailed stability area	57
2.2	Components in a differential pressure mass spectrometer.....	58
2.3	Control diagram for mass spectrometer.....	59
2.4	Timing diagram for mapping stability regions	60
2.5	Stability diagram for a CIT at 1 Torr air buffer gas.....	61
2.6	Stability diagrams for a CIT at A) 500 and B) 1500 mTorr air	62
2.7	Stability diagram for a CIT at 1 Torr air buffer gas.....	63
2.8	Stability diagrams for a CIT at 10 mTorr helium buffer gas	64

2.9	Stability diagrams for a SLIT at 1 Torr air buffer gas	65
2.10	Stability diagrams for a SLIT at 10 mTorr helium buffer gas	66
2.11	Stability diagram for a SLIT, generated via SIMION	67
2.12	Trajectories of ions from SIMION simulation.....	68
2.13	Supplemental AC with trapped ions at 1 mTorr helium buffer gas.....	69
2.14	Supplemental AC with trapped ions at 300 mTorr helium buffer gas.....	70
2.15	Supplemental AC with trapped ions at 1.0 Torr helium buffer gas.....	71
3.1	Ring electrode geometries and axis nomenclature.....	97
3.2	Isopotential lines in a tapered SLIT geometry	98
3.3	Relative intensity of signal from a tapered SLIT.....	99
3.4	Ratio of the signal intensities from ends of tapered SLIT	100
3.5	Printed circuit board with supplemental electrodes	101
3.6	Mass spectra with supplementary electrodes.....	102
3.7	Mass spectra from the side with supplementary electrodes.....	103
3.8	Indirect mass spectra.....	104
3.9	Apex isolation	105
3.10	Multi-frequency isolation.....	106
3.11	Partial instability scan isolation	107

3.12	Tandem mass spectra of bromobenzene	108
3.13	Tandem mass spectra of N,N-dimethylaniline.....	109
3.14	Tandem mass spectra of tryptophan	110
3.15	Tandem mass spectra of RGEN.....	111
3.16	Series of mass spectra from 1,3-dichlorobenzene.....	112
3.17	Signal intensity heat map from spectra of N,N-dimethylaniline (CIT)	113
3.18	Signal intensity heat map from spectra of N,N-dimethylaniline (SLIT)	114
4.1	Fragmentation heat map patterns ($x_0 = 270 \mu\text{m}$)	139
4.2	Fragmentation heat map patterns ($x_0 = 170 \mu\text{m}$)	140
4.3	Conversion efficiency measured from Figures 4.1 and 4.2	141
4.4	Fragmentation heat maps (500 – 1500 mTorr)	142
4.5	Survival yield and half-persistence voltage of trichlorobenzene	143
4.6	Appearance curve of m/z 145.....	144
4.7	Appearance curve of m/z 110.....	145
4.8	Fragmentation heat maps (He vs. Air).....	146
4.9	Chromatogram of a mixture of chemical warfare agent simulants (He)	147
4.10	Chromatogram of a mixture of chemical warfare agent simulants (N_2).....	148

LIST OF TABLES

4.1	Table showing masses and polarizabilities of common buffer gases for CID.....	138
-----	---	-----

LIST OF ABBREVIATIONS AND SYMBOLS

Abbreviations:

BWA	Biological warfare agent
CID	Collision-induced dissociation
CIT	Cylindrical ion trap
CWA	Chemical warfare agent
CWAS	Chemical warfare agent simulant
DAPI	Discontinuous atmospheric pressure inlet
DC	Direct current
FID	Flame ionization detector
FT-ICR	Fourier transform ion cyclotron resonance
FWHM	Full width at half maximum
GC	Gas chromatograph
HPMS	High pressure mass spectrometry
IMS	Ion mobility spectrometry
IRMPD	Infrared multi-photon dissociation
LIT	Linear ion trap
MEMS	Microelectromechanical system

MS	Mass spectrometry
MS/MS	Tandem mass spectrometry
PCB	Printed circuit board
PTM	Post-translational modification
QIT	Quadrupole ion trap
Q-TOF	Quadrupole time-of-flight mass spectrometer
RF	Radio frequency
SLIT	Stretched length ion trap
SWaP	Size, weight, and power
SWIFT	Stored waveform inverse Fourier transform
TIC	Toxic industrial compound
UVPD	Ultraviolet photodissociation

Symbols:

a_u	Mathieu stability parameter in u dimension
D_z	Pseudopotential well depth
e	Charge of trapped ion in Coulombs
m	Ion mass

m/z	Ion mass-to-charge ratio
P	Pressure
q_u	Mathieu stability parameter in u dimension
r_0	Radius of ring electrode
U	Amplitude of DC voltage on ring electrode
V	Amplitude of RF voltage on ring electrode
z_0	Axial distance from center of trap to endcap
β_u	Dimensionless trapping parameter in the u dimension
Ω	Angular drive frequency
ω	Secular frequency

Special Units:

amu	Atomic mass units
sccm	Standard cubic centimeters per minute
V_{p-p}	Peak-to-peak amplitude of AC waveform

Chapter 1: Miniature Mass Spectrometry and Rapid Threat Detection

Introduction

Resolution^{1,2} and sensitivity^{3,4} are often regarded as the driving forces in cutting edge analytical instrumentation. These characteristics define the state of the art equipment for many research fields in mass spectrometry, including discovery based assays such as proteomics.^{5,6} While high throughput experiments often push for fast analysis times,⁷ rapid threat detection fundamentally requires a quick response time to identify an unknown compound.^{8,9} Generating information about unknown threats is important for initiating the appropriate response protocols, and the speed of acquiring that information is imperative. Traditional methods of bringing samples from the field to a laboratory are impractical on the timescale of a threat such as a chemical warfare agent (CWA). The solution, therefore, is to bring analytical power out of the laboratory and into the field.

Mass spectrometry (MS) has been called the gold standard of laboratory-based analytical techniques due to its speed, sensitivity, resolution, and broad range of detectable analytes. These impressive capabilities, however, are restricted to the laboratory by the large size, weight, and power (SWaP) associated with the instrumentation. The technical expertise required to operate the devices is yet another barrier. Many groups have worked towards bringing MS into a field setting¹⁰⁻¹² by re-engineering and repackaging conventional mass spectrometry techniques. Truly hand-portable forms of ion trap mass spectrometry, however, are possible only with a re-imagination of the traditional operating procedures.

High pressure mass spectrometry (HPMS) has recently been shown as a viable strategy to push the frontiers of miniaturized mass spectrometry.¹³ Operating ion traps at pressures near 1 Torr greatly reduces the vacuum requirements of the system, eliminating the need for bulky, fragile, and power-intensive turbomolecular pumps. Using air as a buffer gas, rather than helium, can further reduce overall system size and complexity by eliminating the need for a helium tank, as recently demonstrated.¹⁴ A drawback to HPMS, however, is a loss of resolution due to collisional broadening. As the resolution of an instrument decays, more species appear isobaric, necessitating other means of identification. Tandem mass spectrometry (MS/MS) with parent ion fragmentation is one such method, and it is often used to differentiate between isobaric species including structural isomers.¹⁵⁻¹⁷ Analyzing fragmentation patterns generates chemical information about bonds and connectivity beyond just the total molecular mass-to-charge ratio. Fragmentation patterns can also be used to correlate two peaks in a full mass scan and prevent misinterpretation of complex samples.¹⁸ The added information from this technique has proven extremely useful in virtually every application of mass spectrometry, from proteomics^{19,20} to environmental analysis.^{21,22} The additional chemical data can significantly improve the selectivity of an instrument. In many uses of portable MS systems, such as rapid threat detection, it is very important to reduce costly false positives^{23,24} with a highly selective instrument.

This chapter will discuss important aspects of threats such as CWAs, which mandate improved portable detection technologies, in Section 1.1. The next section will describe traditional quadrupole ion trap theory, while tandem mass spectrometry will be detailed in Section 1.3. High pressure mass spectrometry operation will be outlined in Section 1.4.

1.1 Chemical Warfare Agents and Other Critical Threats

Chemical warfare agents (CWAs) represent significant dangers, especially to those unaware of their presence.²⁵ The same is true of toxic industrial compounds (TICs),²⁶ biological warfare agents (BWAs)²⁷ and many other chemicals that may be present in harsh environments. Extensive research exists into ways to protect oneself from these threats and into methods of treating symptoms post exposure.^{23, 28, 29} Many of these proactive and reactive response protocols, however, are costly both in money and in time. Destruction of the chemical warfare agent itself can be a complicated, slow process.²⁴ Antidotes can be rare and expensive. A soldier finding, putting on, and continuing to wear a HazMat suit can be tactically hindering. It is therefore crucial to enact exactly the correct response for a given threat. A small, portable, low power device with a quick analysis time and high selectivity can deliver actionable intelligence to someone in the field, initiating the appropriate protective or curative procedure when necessary.

CWAs comprise a broad range of chemical compounds with diverse properties.²⁵ They represent any number of potentially harmful materials that might be used against soldiers or even civilians. There are several major subclasses that are useful to consider: blister agents, nerve agents, asphyxiants, pulmonary damaging agents, and incapacitating agents. These classes are largely characterized by the symptoms they produce, but they have can have drastically varying chemical compositions and physiological mechanisms. Inhalation, physical contact, and ingestion are all common means for these compounds entering the body, depending on the physical properties of the agent itself. Furthermore, the safe levels of exposure tend to be quite low, but can also diverge wildly depending on the type of threat. Lethal concentrations for rats can range from ~ 40 parts per trillion for GD agents to 50 parts per million for Lewisite.³⁰

Historically, soldiers were trained to recognize these threats via observable characteristics of the CWA. Odors and colors of the toxic compound were the most common indicators. Gas masks, gloves, and other protective equipment could be deployed on recognition, but often by the time a CWA is noticeable, the observer has already received a significant exposure. An example table from a World War II era American warship is shown in Figure 1 to demonstrate the standard expectations for soldiers in threat identification and protection. If exposure occurred, doctors and medics were able to apply antidotes or other treatments based on the collected information. While research into post-exposure biomonitoring continues,³¹ it is clearly preferable to avoid significant exposure in the first place. It is also more desirable to have information about the threat from an impartial monitor rather than a panicked victim. For these reasons, appropriate sensors can improve protection for soldiers and other potential targets with fast and reliable threat identification. Low limits of detection and quick response times can trigger the use of protective equipment, while high selectivity ensures that the appropriate response is enacted to mitigate the threat.

Accurate detection and identification is often hindered by interferences and contaminants. In complex field environments, like a battlefield, there will clearly be many chemical compounds present in the air. Beyond the normal components of air, a battlefield atmosphere likely includes emissions related to gasoline combustion from vehicles, possible compounds from weaponry, and other chemicals native to the environment. All of these potential species can possibly overwhelm or interfere with the signal of a true CWA threat and obscure detection. They may also cause the sensor to issue a false positive: the activation of an alarm when no threat is present. False positives can pose huge problems for two primary reasons. First, a response protocol will be performed when there is no necessity or advantage while incurring the full costs

in time and in money. Second, users can lose faith in the reliability of the sensor after many false positives. Existing technology for rapid threat detection has been plagued with this situation. There are stories of soldiers in the combat zone leaving their detection devices in the truck or at base due to this lost trust. A detection device that is left behind is no better than not having one in the first place. It is for these reasons that a low false positive rate is crucial to the success of a rapid threat detection device.

Existing technology for threat detection in the battlefield consists of a few primary technologies. Ion mobility spectrometry (IMS) is at the forefront of the field given its speed of analysis, low limits of detection, and low cost of implementation.³²⁻³⁴ The technology itself, however, is limited by poor inherent resolution as well as low selectivity.³⁵⁻³⁷ Peaks from a mobility spectrum tend to be quite broad, and diverse species with hugely different chemical properties may have the same or similar mobilities. These two factors contribute to a high false positive rate, even in the most advanced instruments. Mass spectrometry, however, is an inherently selective technique due to measuring the mass-to-charge ratio of a chemical compound. Portable mass spectrometry is therefore an extremely exciting and powerful option for rapid threat detection.

1.2 Quadrupole Ion Traps

Quadrupole ion traps (QITs) represent the most intriguing mass analyzer for portable instrumentation for several reasons. First, their fundamental performance in terms of resolution does not depend on the critical dimensions of the mass analyzer itself. Magnetic sectors and time-of-flight instruments, for example, rely quite heavily on having a long enough path for the

ions to separate based on their mass-to-charge ratio. The ion trap performs this separation based on interactions with an alternating potential in the trapping volume, even at small sizes. Second, ion traps, even in conventional operation, operate at much higher background pressures than other mass analyzers. Time-of-flight and Fourier transform mass spectrometry require very long mean free paths so an ion's trajectory is not disrupted by a collision with a neutral gas molecule. These types of analyzers are often operated around 10^{-9} Torr. Ion traps actually have improved sensitivity and resolution with some amount of background gas and are frequently operated near 10^{-3} Torr.³⁸ These higher operating pressures greatly reduce the pumping requirements, which represent a high percentage of the SWaP for a portable device. The benefits from higher operational pressures will be further discussed in Section 1.3.

The quadrupolar ion trap has existed for the purposes of ion storage without magnetic fields since Wolfgang Paul's work in the 1950s.^{39, 40} Fundamentally, it consists of a ring electrode and two endcaps with hyperbolic cross-sections. A radio frequency (RF) potential is applied to the ring electrode to create a quadrupolar electric field. An example of the electrodes is shown in Figure 2. These new traps represented a large improvement from previous trapping strategies which required a magnetic field and very strict vacuum conditions.⁴¹ Even before being used for mass spectrometry, electrodynamic ion traps were used by physicists to study the fundamental properties of isolated gas-phase ions as well as their interactions with neutrals.

Mathematical formulas can be derived from first principles to describe how charged particles behave within the confines of the trap.⁴²⁻⁴⁴ Although first investigated for a very different application, the solutions to the Mathieu equation⁴⁵ describe the possible trajectories of ions in these oscillating electric fields, including whether they are periodic. Periodic trajectories mean that an ion is stably trapped and will not leave the trap without a perturbation or the addition of

energy. Further derivations lead to the unitless fundamental trapping parameters, a_u and q_u , where each parameter may be calculated for either the radial, r , or axial, z , dimension of the trap, as shown in the following equations:

$$a_z = -\frac{16eU}{m(r_0^2 + 2z_0^2)\Omega^2} \quad (\text{Eq 1.1})$$

$$a_r = \frac{8eU}{m(r_0^2 + 2z_0^2)\Omega^2} \quad (\text{Eq 1.2})$$

$$q_z = \frac{8eV}{m(r_0^2 + 2z_0^2)\Omega^2} \quad (\text{Eq 1.3})$$

$$q_r = -\frac{4eV}{m(r_0^2 + 2z_0^2)\Omega^2} \quad (\text{Eq 1.4})$$

where e is the number of fundamental charges on an ion, U is the DC potential applied to the ring electrode, m is the mass of the charged particle, r_0 and z_0 are the critical dimensions of the hyperbolic trap, Ω is the angular frequency of the RF potential applied to the ring electrode, and V is the 0-Peak amplitude of that same RF potential. Based on the a and q parameters, a map showing regions of stable trapping in both r and z dimensions resulting from solutions to the Mathieu equation can be made and is shown in Figure 3. The region, labeled A, along the $a_u = 0$ axis with low q_u values is the easiest to access, the most commonly used, and the best understood region for ion trapping. A closer look at this region is shown in Figure 4. The parameter β describes how the ion falls within the trapping region, between 0 and 1. For values of $q_z < 0.4$, β_z is typically approximated as follows:

$$\beta_z \cong \sqrt{a_z + \frac{q_z}{2}} \quad (\text{Eq 1.5})$$

where a and q are the previously discussed trapping parameters. The variable β is useful for a few other calculations. The primary use is determining how ions are moving within the trap.

Trapped ions are by no means stationary within the confines of the electrodes, but are actually traversing the volume based on interactions with the oscillating electric fields. A successfully trapped ion has a trajectory that is periodic and does not move beyond the trapping volume. The primary component of this motion is known as the secular frequency, ω , which can be simply calculated as follows:

$$\omega_z = \frac{\beta_z \Omega}{2} \quad (\text{Eq 1.6})$$

This secular frequency is an important aspect of ion trapping. Due to the β term, an ion's secular frequency relies on its mass-to-charge ratio, and different mass ions will have different frequencies of motion within the trap. The implications of this phenomenon are powerful and can be exploited.

The majority of these equations so far have simply addressed whether or not an ion is trapped, but not the extent of the trapping forces. Dehmelt, through further observations and calculations, generated the following approximation of the pseudopotential well depth in an ion trap, D_z , if $q_z < 0.4$:

$$D_z = \frac{eV^2}{4mz_0^2\Omega^2} = \frac{q_z V}{8} \quad (\text{Eq 1.7})$$

D_z is a statement as to the maximum amount of kinetic energy a trapped ion may possess while maintaining a stable trajectory in the trapping volume.⁴⁶ In essence, the pseudopotential well is a time-average of the trapping forces from the oscillating electric fields. This concept also has dramatic consequences for the operation of ion traps.

Mass spectrometry only became possible in a quadrupole ion trap with the innovation of mass selective storage. Dawson and Whetten drilled holes in the endcaps of a QIT thereby

creating the opportunity for a DC pulse to eject the ion population towards an electron multiplier for detection.^{47, 48} While operating at the apex (near the intersection of the $\beta_z = 0$ and $\beta_r = 1$ lines) of the a - q stability diagram (Figure 4), only ions of a single mass-to-charge ratio were stably trapped and then detected. The process of collecting data over a broad mass range, however, was tedious and slow. Furthermore, the quadrupole mass filter was already a capable and well-entrenched instrument.

In the early 1980's, George Stafford made a groundbreaking innovation to bring QITs fully into the world of mass spectrometry. His realization that the voltage of RF on the ring electrode could be continuously adjusted during an experiment led to the mass selective instability scan.⁴⁹ A mass spectrum could be created by trapping a broad range of ions along the $a_z = 0$ axis with a constant RF potential and then sequentially ejecting the ions at the $q_z = 0.908$ boundary (Figure 4) with an increasing RF potential. As the RF voltage increases, progressively larger m/z ions reach this boundary, ejecting along the axial dimension and impacting the electron multiplier detector. The resulting signal is a mass spectrum from all of the ions that were stable under the initial trapping conditions.

This novel method led to successful commercialization of the QIT by Finnigan Corporation.⁵⁰ In its initial product launch, it was used as a compatible detector for a gas chromatograph in 1984 and provided mass information about the analytes. It was also sold as a standalone product in 1985. These devices were what defined the standard trap size of $r_0 = 1$ cm. The public availability of these products also led to the bloom of research into ion traps as mass spectrometers and related applications. QITs are now commercially available from many companies for a variety of applications. Ion traps are common components in many hybrid instruments, utilized for their experimental versatility.

The secular frequency of trapped ions was briefly discussed earlier and we now look at how this phenomenon can be used for interacting with stored ions. The secular frequency of an ion describes its path through the confines of the trapping volume. This movement can be envisioned as a harmonic oscillation but with perturbations possible under specific conditions. Collisions with neutral gas molecules introduce a damping term³⁸, while adding a dipolar supplementary AC potential at the secular frequency to the endcaps of the ion trap can cause a resonant excitation of the motion. Resonant excitation of the ion trajectory adds kinetic energy to the ion itself, changing the previously stable trajectory. It is important to remember that because ions of different mass-to-charge have different secular frequencies, they will not be resonantly excited by the same supplemental frequencies. By tuning the supplementary AC potential, specific mass-to-charge ions can be selectively targeted for ejection.

Under certain conditions, the application of supplemental AC to the endcaps can excite a trapped ion to the point that it becomes unstable in the trap and is resonantly ejected.⁵¹ A common strategy with resonant ejection is to apply a single fixed frequency to the endcaps, then ramp the voltage of the drive frequency as for a usual mass spectral scan, causing the secular frequency of each ion to change until it comes into resonance with the supplemental AC. Resonant ejection is a powerful technique in ion trap mass spectrometry where ions can be ejected at a point in the stability diagram other than the $q_z = 0.908$ boundary. This capability has some far-reaching implications. Firstly, it can easily extend the mass range of an instrument by ejecting ions that would otherwise be too large to reach the boundary point with the existing power supply maximum voltages.⁵² The boundary ejection of high mass-to-charge species can require many kilovolts of potential, which is difficult to generate and may also cause electrical breakdown within the vacuum chamber. Secondly, resonant ejection can cause larger mass-to-

charge ions to exit the trap before smaller ones. The benefits of non-sequential ejection will be discussed in more depth in the next section. Thirdly, there has been some data suggesting that resonant ejection can lead to higher resolution mass spectra than ejection under boundary conditions.⁵³

The quadrupole ion trap has made a large impact on the world of mass spectrometry because of its unique combination of low cost and high flexibility. The system design is comparatively simple, and the theoretical basis is well-studied on a fundamental level, leading to a reliable instrument. All of these characteristics are important for portable instrumentation. For these reasons, ion traps are poised to play a significant role in harsh environment mass spectrometry.

1.3 Tandem Mass Spectrometry

Tandem mass spectrometry is an important development and a large factor in why mass spectrometry has become such a dominant player in the field of analytical instrumentation. At its fundamental level, tandem mass spectrometry is the act of performing multiple mass spectrometric selections on the same set of ions. Each experiment uncovers new information if the analyte is made to undergo a structural change in between the acquisition of spectra. The most common of these is fragmentation. With mass-to-charge information about an analyte before and after a fragmentation event, it is possible to discover significant structural information. Combining the structural information with the mass data can often result in confident identification of compounds, even among compounds with the same chemical formulas, known as isomers.

One of the simplest and most common instruments for achieving tandem mass spectrometry is the triple quadrupole mass filter. An example illustration is shown in Figure 5. A generalized experiment can be performed where the first set of quadrupole rods (Q1) pass ions of a specific mass-to-charge, the second set of rods (Q2) impart energy and induce fragmentation of those ions, and the third set (Q3) then selects for the desired mass-to-charge fragment ions. Thus, two separate mass spectrometry experiments are performed: one on the injected sample and one on the fragments induced from the initially selected species. With an instrument in this configuration, however, there are still several different ways to perform experiments. Each is useful in attaining certain types of information and will be discussed in the following paragraphs. Analogous experiments are all possible within a single ion trap.

Selected reaction monitoring is perhaps the most straightforward mode of tandem mass spectrometry and shown in Figure 5B. In this method, both the first and third sets of quadrupole rods (Q1 and Q3) are set to pass specific, but different, mass-to-charge ions. This type of experiment selects one specific species, known as a precursor, with the first mass filter (Q1). The precursor is then fragmented in the second quadrupole (Q2), creating an array of product ions with new mass-to-charge values. A specific mass-to-charge ratio, corresponding to an expected product ion, is filtered through the third quadrupole (Q3). The process is useful for evaluating the extent of fragmentation as a function of imparted energy to learn more about the chemical properties of the targeted compound. The strategy can also be useful in identifying a specific molecule from a complex sample with a high degree of certainty.

A second mode, product ion scanning, is a strategy achieved by fixing the first quadrupole mass filter (Q1) to pass only a given mass-to-charge species, inducing fragmentation in Q2, and scanning the third set of rods (Q3) across a wide range of mass-to-charge ratios. In this way, a

specific precursor ion is selected and fragmented, but the results of the fragmentation need not be known before the experiment. Information about the particular fragmentation pathways can be gathered from the new data. This technique generates more information that can be used for determining the chemical identity of the precursor ion.

Parent ion scanning is a tandem MS procedure implemented by scanning the first mass filter (Q1), imparting energy in Q2, and holding the Q3 mass filter constant at a given mass-to-charge ratio. During the experiment, many different ions are fragmented and observed to see if they produce a specific product. The resulting information is useful for several reasons. First, it can provide information about the relationship between multiple peaks in the first mass spectrum. Identifying parent ions can reveal adducts compared to contaminants in the sample, for example. This can simplify the initial spectrum and aid compound assignment. Second, it is possible to learn about the compound class of the precursor ion through this method. For example, many lipids will fragment to a specific product ion which is indicative of the lipid class overall. It is now easier to identify the precursor ion species that resulted in this product due to confident understanding of its class.

Lastly, neutral loss scanning is a strategy accomplished by scanning both the first and second mass filters (Q1, Q3) at the same time, with a constant mass offset between the two. Many precursor ions may be selected, but the only species hitting the detector will be those that fragment at the mass offset between the filters. This type of experiment can also be useful for adding information about the class of precursor ions. As an example, proteins with post-translational modifications (PTMs) can be easily identified in this manner as the PTM tends to readily fragment away from the ion as a neutral loss.

Although each of these strategies was described as a method for a triple quadrupole instrument, they may be implemented in a variety of fashions. The instrument simply needs to perform at least two stages of mass spectrometry with some form of activation in between the stages. Another very common tandem mass spectrometry instrument design is the quadrupole time-of-flight (Q-TOF) in which a quadrupole mass filter acts as the primary mass spectrometer isolating the targeted analyte. The time of flight is then used as a higher resolution second mass analyzer. It has also become popular to use trapping instruments as the first stage of mass analysis due to their ability to accumulate continuously generated ions while the secondary stages are analyzing, keeping the duty cycle for ion acquisition high and enhancing sensitivity. The advantages from this strategy are highlighted when coupled to a relatively slow mass analyzer, such as a Fourier transform ion cyclotron resonance (FT-ICR) or Orbitrap.

While this discussion has focused heretofore on combining mass spectrometers, it is also advantageous to perform tandem mass spectrometry within a single ion trap. Multiple mass analyzers can be used for tandem mass spectrometry in space, while one can achieve tandem mass spectrometry in time using only a single ion trap.^{54, 55} With this strategy, a diverse sample of ions can be collected in the trap, which is then made to eject all ions not of a specific mass-to-charge ratio. The remaining trapped ions can be fragmented by a variety of methods as discussed in the following paragraphs. The resulting fragment ions remain stored in the trap and a new mass spectrum is generated as in a conventional experiment. Tandem mass spectrometry in an ion trap is advantageous as it does not require any additional space for new mass analyzers or even additional power supplies that would not be normally used for operation of the ion trap. These advantages are especially relevant when designing a portable, low power instrument.

In order to achieve tandem mass spectrometry in an ion trap, it is necessary to isolate ions of a given mass-to-charge before inducing fragmentation. Resonant ejection, as discussed earlier, is a method to eject ions of high mass while preserving lower mass ions. Scan functions can be created to sequentially eject all mass-to-charge ions except for a target by setting a single supplemental AC on the endcaps and strategically ramping the drive RF voltage such that all other ions come into resonance. Thus, every ion except a single mass-to-charge of interest are ejected from the trap and the target analyte is isolated. A similar effect can be achieved via stored waveform inverse Fourier transform (SWIFT). With this technique, an arbitrary waveform is generated such that it contains every frequency except for the secular frequency of the target ion. When the synthesized waveform is applied to the endcap, it can resonantly eject all non-targeted ions and achieve isolation.

Once ions of a specific mass-to-charge have been isolated, there are also many ways to induce fragmentation. For example, photodissociation can be accomplished by irradiating the ions with light, usually from a laser. Photons are absorbed, causing an increase in internal energy until the vibrational modes are excited to the point of breaking the chemical bonds, causing fragmentation. This process may be activated with multiple photons in the infrared (infrared multi-photon dissociation, IRMPD) or a single photon in the ultraviolet (ultraviolet photodissociation, UVPD).

The most common ion activation method by far, however, is collision induced dissociation (CID). In this process, ions are forced into collisions with neutral gas molecules. In a triple quadrupole, this is typically achieved with a DC gradient into an increased pressure region in the second set of rods (Q2). In an ion trap, this can be effected by subjecting ions to brief resonant excitation. By balancing the exciting and restoring forces in the ion trap, an ion can have kinetic

energy added without leaving the confines of the electrodes. As the ion resonantly gains kinetic energy, collisions with neutral gas molecules cause that energy to be converted into internal energy. The collisions slowly cause the ion to accumulate enough internal energy to fragment. After ion activation, the resulting fragment ions can be mass analyzed to produce the new mass spectrum.

Tandem mass spectrometry is a very useful tool for generating more information about an unknown compound. The fragmentation patterns reveal structural and chemical data about the precursor, aiding greatly in identifying a target. In an ion trap, this capability can be achieved without increasing the footprint or power needs of a device. The low time cost for additional information is very attractive for a portable instrument that seeks to maximize its selectivity.

1.4 High Pressure Mass Spectrometry

The size, weight, and power of portable mass spectrometers are traditionally dominated by the vacuum requirements. Techniques that only function at low pressure mandate low-leak chambers and heavy-duty pumps. Frequently, steel components are used for the chambers, and turbomolecular pumps are included in the system. The steel chamber is both heavy and costly compared to a small plastic chamber that is sufficient for less extreme vacuum systems. Additionally, turbomolecular pumps are expensive, power-hungry, and extremely fragile. Much work has been done in the area of miniaturizing turbo pumps, but they remain problematic for the needs of portable instrumentation. The cost from both a financial and power perspective is an extremely high percentage of practical limits for a compact device. The fragility of the component also greatly affects the ruggedness of any potential final product, essentially ruling it

out for many harsh environments. Even accidental dropping of the instrument during otherwise routine usage may cause serious damage to a spinning turbo pump. Eliminating the necessity for this type of pump is a huge competitive advantage for high pressure techniques.

A pump must be able to maintain the operational pressure while gas flows through an aperture inlet, delivering the sample. Around two mL/min of gas flow through the chamber provides sufficient analyte, without being an unnecessarily large load. Minimizing power is crucial, and a typical power budget for pumping may be only a few Watts. It was determined that a single, miniaturized scroll pump would be able to achieve these metrics, providing a vacuum condition around 1 Torr. This pressure then became the goal for making high pressure mass spectrometry a practical technology.

Some strategies to minimize the pumping load exist, but often come with tradeoffs. Discontinuous atmospheric pressure interfaces (DAPI),^{56, 57} for example, is capable of mass spectral determination at lower pressure, but it severely compromises the duty cycle of the instrument. Low duty cycles hinder sensitivity and analysis speed. In DAPI style instruments, such as from the Cooks and Ouyang labs,⁵⁸ the atmospheric inlet is only open briefly (10-20 ms) for sample introduction, then the inlet is closed to restore low pressures for the rest of the scan function. Ions are trapped as soon as they are introduced, and they are preserved through the lowering of the pressure. Mass analysis is performed at low pressures, which are calculated based on flow rates and pumping speeds. In all, the entire scan function takes ~1 second. Continuous sampling interfaces have much faster scan functions (~10-20 ms total) as well as inherently higher duty cycles for analyte collection. With very low scan times, signal averaging can be used to improve signal-to-noise while maintaining a rapid analysis.

High pressure operation, however, is not without its own fundamental tradeoffs.⁵³ Existing theory suggests that the maximum achievable resolving power is limited by the ratio of the background pressure to the drive frequency of the trap.^{59, 60} This can be stated as

$$\frac{\Delta m}{m} \propto \frac{P}{\Omega} \quad (\text{Eq 1.8})$$

where Δm is the peak width, m is the mass of the ion, P is the pressure of buffer gas, and Ω is the frequency of RF applied to the ring electrode. Simply, this equation suggests that the rate of collisions between trapped ions and neutral buffer gas disperses ions and widens spectral peaks while faster oscillation of the trapping fields can narrow spectral peaks. Experimental results have also shown increasing pressure to cause deterioration of spectral peak width.^{61, 62}

As a reference point, conventional ion trap mass spectrometers have used hyperbolic geometries with $r_0 = 1$ cm and $\Omega \approx 1.1$ MHz. As pressure increases, Equation 1.8 suggests that raising Ω will offset losses in resolution and preserve peak widths. Changing Ω is not without its own consequences as the following equation shows in calculating the maximum mass range of an ion trap:

$$\frac{m_{max}}{e} = \frac{8V}{q_z(r_0^2 + 2z_0^2)\Omega^2} \quad (\text{Eq 1.9})$$

This equation states that as Ω increases, in order to maintain a high mass range, either voltage must be increased or trap size must be decreased. Increasing voltage is a problematic route for several reasons. First, higher voltages require higher power to generate, which is not desirable in a portable instrument with minimized SWaP. Second, electrical discharge at high voltages on closely spaced electrodes can be a problem in vacuum chambers, especially with

pressures around 1 Torr, as described by Paschen's law.⁶³ Maintaining lower voltages, by reducing trap dimensions to offset frequency increase, is useful in avoiding dielectric breakdown. Electrode miniaturization has clear advantages for portability. By reducing the size of the trap to $r_0 < 500 \mu\text{m}$, the ion trap is able to achieve sufficient mass range for analysis of volatile compounds at high frequencies.⁶⁴

Fabrication of hyperbolic geometry electrodes at these small sizes, however, is difficult to say the least.^{65, 66} A suitable approximation of the hyperbolic geometry can be made with the much simpler cylindrical ion trap (CIT)⁴⁰ as shown in Figure 6. The contributions to the overall electric field from higher order components are much larger with this cylindrical geometry, but the quadrupolar effects dominate, especially near the center of the trap where ions are normally stored.⁶⁷⁻⁶⁹ The overall similarity of the generated electric fields means that operationally a cylindrical ion trap can be used for mass spectrometry in much the same way as a hyperbolic ion trap.

One of the fundamental problems stemming from reduced trap size is an inherent decrease in the number of ions that can be analyzed within a trap. A potential solution to this situation is to fabricate an array of ion traps that can be operated in parallel. The ion intensities from each trap may be added so that the sum of all the signals is the result. The underlying assumption for ion trap arrays, however, is that all of the traps are behaving identically. This can be a significant problem at smaller sizes for several reasons. First, the tiny dimensions of the traps mean that it is easy for small changes in alignment or fabrication differences to cause imperfections and variations between the traps. Different electric fields can cause different mass spectra. Second, ion distribution must also be even across the array, as the number of ions within a trap can affect the resulting mass spectrum. If two traps within the array are not operating in exactly the same

conditions, it is likely to cause broadening of the resulting peaks rather than an increase in intensity of the same width peak. This loss in resolution can be a steep price to pay for the sensitivity gains.

The stretched length ion trap (SLIT) geometry is a different approach to solving the sensitivity concern.^{70, 71} A SLIT can be fabricated in a similar fashion to a CIT, and a comparison of electrodes is shown in Figure 7. If the ring electrode of a CIT is fabricated by milling out a single hole in sheet metal, the SLIT ring electrode feature can be made by translating the drill bit through the metal for a defined distance. The resulting trap geometry has an ion capacity defined, at least in part, by its length while it has trapping characteristics defined predominantly by the narrow x and z dimensions. This combination is quite beneficial for its use in HPMS. Ions seem to populate the entire length so a much higher number of ions can be stored in a single trap. Resolution and ejection, however, are defined by the much smaller critical dimensions, with the aforementioned advantages of small traps.

The combination of these high pressure strategies results in a truly hand-portable mass spectrometer. This tool can provide new types of data in field environments and inform crucial time-sensitive decisions. In these settings, it is important to remember that the relevant figures of merit are often different than they may be in a laboratory environment. In a core facility at a proteomics lab, for example, resolution is of utmost importance for discovering new proteins in a biological sample. A large, power-hungry device that is relatively slow is quite acceptable as long as the identification of complex, trace components is possible. On the frontline of a warzone, however, rapid and reliable detection of a CWA such as mustard gas is far more important. A small, fast device, even with low resolution, is much more useful in this circumstance. These scenarios provide an illustration of how different aspects of an analytical

instrument are brought to the forefront in different applications. Even if high pressure mass spectrometry is limited in discovery applications, it is poised to make a large impact in the world of detection.

1.5 Objectives

Broadly, the research described herein focuses on improving the selectivity of high pressure mass spectrometry. As noted previously, the extreme reductions in size, weight, and power granted by HPMS come with a reduction in resolution. Many potential applications, however, require a high degree of certainty in identification of unknowns, meaning that good selectivity is an important characteristic of a final device.

To realize the full capabilities of a mass spectrometer with high operating pressure, it is necessary to understand how the pressure is affecting traditional modes of ion trapping. Chapter 2 is a discussion of experiments related to these topics. Investigations were made into how pressure, buffer gas identity, and trap geometry govern the stability regions of trapped ions. Furthermore, the impacts from these parameters on the secular frequency and resonant ejection characteristics were studied.

Beyond simply revealing the changes in behaviors of ions at high pressures, achieving ion manipulation is an impactful goal. Chapter 3 focuses on several modes of ion manipulation. First, ion isolation was achieved by apex isolation, by multi-frequency isolation, and by partial instability scan. Furthermore, manipulation of ions along the previously unconstrained axis of a stretched length ion trap was accomplished via simple alterations to electrode geometries. Additionally, collision induced dissociation was shown in high pressures with several classes of

compounds. Several volatile organic compounds were fragmented, including chemical warfare agent simulants. Fragmentation of nonvolatile analytes, such as peptides and amino acid clusters, was also demonstrated.

Enhancing the fragmentation efficiencies of collision induced dissociation is one of the strongest ways to maximize the selectivity of a high pressure mass spectrometer. The role of important parameters such as pressure, buffer gas identity, and pseudopotential well-depth was studied, and the results are discussed in Chapter 4. Another potential strategy to enhance selectivity is to couple the mass spectrometer with a separation, such as gas chromatography. This technique is also demonstrated as a feasible approach for achieving greater informing power in HPMS.

1.6 Figures

		Chemical Warfare Agents									
		REFERENCE AND TRAINING CHART					PREPARED BY U. S. OFFICE OF CIVILIAN DEFENSE, JANUARY, 1943				
CLASS	NAME	CWS SYMBOL NICKNAME	METHODS OF DISSEMINATION	PERSISTENCY	ODOR	RELEASED FORM	PHYSIOLOGICAL EFFECT	PROTEC- TION*	DECONTAMINATION	SELF-AID	
VESICANTS	MUSTARD	HS <i>Hot Stuff</i>		3-4 days in open 1 week in woods, several weeks in winter	Garlic, horse- radish, mustard	Dark, oily liquid slowly evaporates	No immediate effect; liquid or vapor burns and blisters skin and lungs; eye irritation		Use bleaching powder alone or mixed with water or earth, hypochlorite solution, green solution steam, heat, or solvents	1. Most injury from gas can be prevented if air raid instructions and certain simple self-aid rules are followed.	
	LEWISITE	M-1 <i>Mean One</i>		1 day in open, 2-3 days in woods, 1 week or more in winter	Geraniums	Dark, oily liquid slowly evaporates	Immediately irritates nasal passages; later burns skin and eyes; arsenic poisoning		Water flush or use bleaching powder alone or mixed with water or earth, hypochlorite solution, green solution, steam, heat or solvents	2. If exposed to gas: (a) Act promptly and quietly. Be calm. (b) Remain indoors or go indoors, unless official duties require one to stay outside.	
	ETHYLDI- CHLORARSINE	ED <i>Enemy's Delight</i>		1-2 hours in open, 2-6 hours in woods, longer in winter	Biting, stinging	Clear, oily liquid, evaporates at medium rate			Cover with earth; use bleaching powder	3. If exposed to vesicants, speed in treatment is important. (a) If outside and contami- nated, remove outer clothing. (b) Go indoors, remove under- clothing and blot up liquid gas on skin with small piece of cloth. Blot, do not rub. Put clothes in covered can.	
LUNG IRRITANTS	CHLORPICRIN	PS <i>Puking Stuff</i>		1 hour in open, 4 hours in woods, longer in winter	Flypaper, anise	Colorless, oily liquid evaporates rapidly	Lung damage; causes severe coughing, crying, nausea, vomiting		Sodium sulphite solution in alcohol	(c) If eyes are splashed with liquid vesicant and not more than five minutes have elapsed, irrigate eyes with large amounts of 2% baking soda solution (tablespoonful to a quart of water) or with water if soda is not immediately available.	
	DIPHOSGENE	DP <i>Di-Phos</i>		30 minutes	Acrid ensilage	Oily liquid evaporates rapidly	Lung damage; causes coughing, lung pains, difficult breathing; highly toxic; eyes water; effects may be delayed		None needed	(d) If materials are available apply household bleaching solu- tion (sodium hypochlorite) to areas contaminated with mus- tard gas; hydrogen peroxide to Lewisite contaminated areas. Lewisite is also effective against Lewisite.	
	PHOSGENE	CG <i>Choky Gas</i>		1-10 minutes	Musty hay, green corn	Colorless gas			None needed	(e) Bathe freely with soap and water, rinse frequently, preferably under shower.	
	CHLORINE	CL <i>Chlorine</i>		1-5 minutes	Highly pungent like household bleach	Yellow- green gas			None needed	(f) Wash nose and throat with baking soda solution.	
LAGRIMATORS	BROMBENZYL- CYANIDE	CA <i>Cry Always</i>		Several days (weeks in winter)	Sour fruit	Dark, oily liquid slowly evaporates	Eyes smart and close; copious flow of tears; skin irritation; temporary effect headaches		Cover with earth or wash with lime slurry	7. Notify air raid warden who will summon necessary medical aid.	
	CHLORACETO- PHENONE	CN <i>Cry Now</i>		While burning	Apple blossoms	Gas or smoke			None needed		
IRRITANT SMOKES	TEAR GAS SOLUTIONS	CNS or CNB		1 hour in open, 2 hours in woods, longer in winter	Apple blossoms + chloropicrin or + benzol	Liquid, which evaporates			None needed	4. If exposed to lung irri- tants, lie down. Complete rest is essential. Prevent chilling.	
	ADAMSITE	DM <i>Dirty Mixture</i>		10 minutes	Slight coal smoke or none	Yellow smoke			None needed	5. If exposed to vesicants and lung irritants, or if in doubt, regarding gas to which exposed, perform steps under 3 and 4.	
	DIPHENYL- CHLORARSINE	DA <i>Dopey Ache</i>		10 minutes	None	Fine white smoke	Causes sneezing, nausea, sick depressed feeling, temporary		None needed	6. Particles of white phos- phorus coming in contact with the skin should be kept covered with water or if available, 2%- 5% copper sulphate (blue vit- riol) solution may be applied, until medical attention is avail- able.	
INCENDIARIES	DIPHENYL- CYANARSINE	CDA		10 minutes	Garlic, bitter almonds	Fine smoke			None needed		
	MAGNESIUM	MG		While burning	None	Molten and burning metal			Control fires with water; control bombs with water		
	THERMIT	TH <i>The Heat</i>		While burning	None	Molten iron	Causes severe burns		Burns out; cannot be smothered or extin- guished by water; control fires with water		
SCREENING SMOKES	THICKENED GASOLINE	None		While burning	Gasoline	Burning particles			Control fires		
	HC MIXTURE	HC <i>Harmless Cloud</i>		While burning	Acrid	Grayish smoke	Harmless		None needed		
	TITANIUM TETRACHLORIDE	FM <i>Floating Mantel</i>		10 minutes	Acrid	Dense white smoke	Harmless		None needed		
	SULPHUR TRIOXIDE <i>in Chlorosulphonic Acid</i>	FS <i>Fuming Spray</i>		10 minutes	Acrid	Dense white smoke	Causes pricking of skin; makes eyes water; causes coughing		None needed		
WHITE PHOSPHORUS †	WP <i>White Phos</i>		While burning	Burning matches	Burns in air to a dense white smoke	Smoke is harmless, but burning par- ticles cause very severe burns		Burns out; control by immersion in water; keep wet			

Figure 1.1. Chart of chemical warfare agents issued by the United States government in 1943, demonstrating ways to identify threats and mitigate their effects.

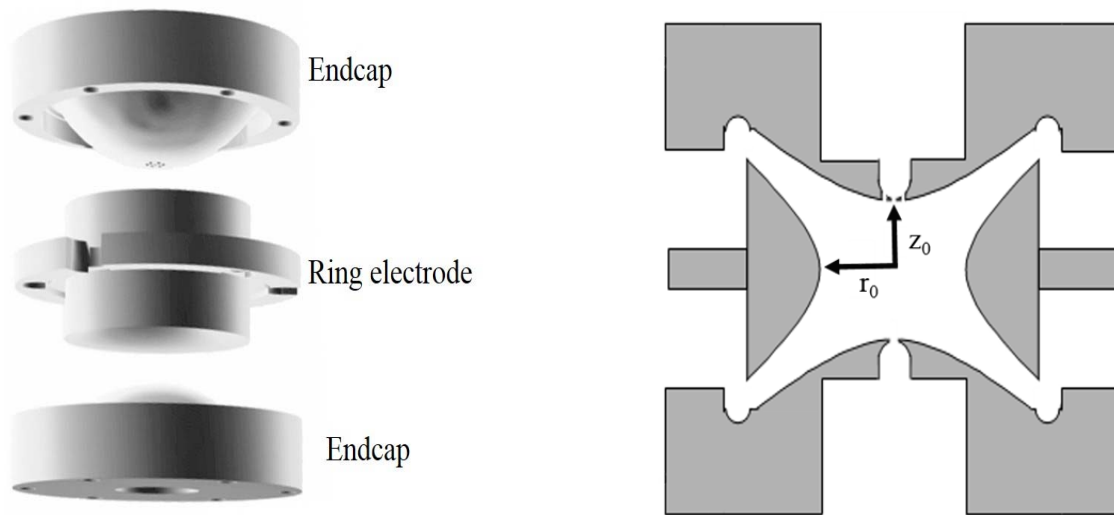


Figure 1.2. Image of steel electrodes in a hyperbolic geometry for three dimensional ion trapping, as well as a cross-sectional diagram.

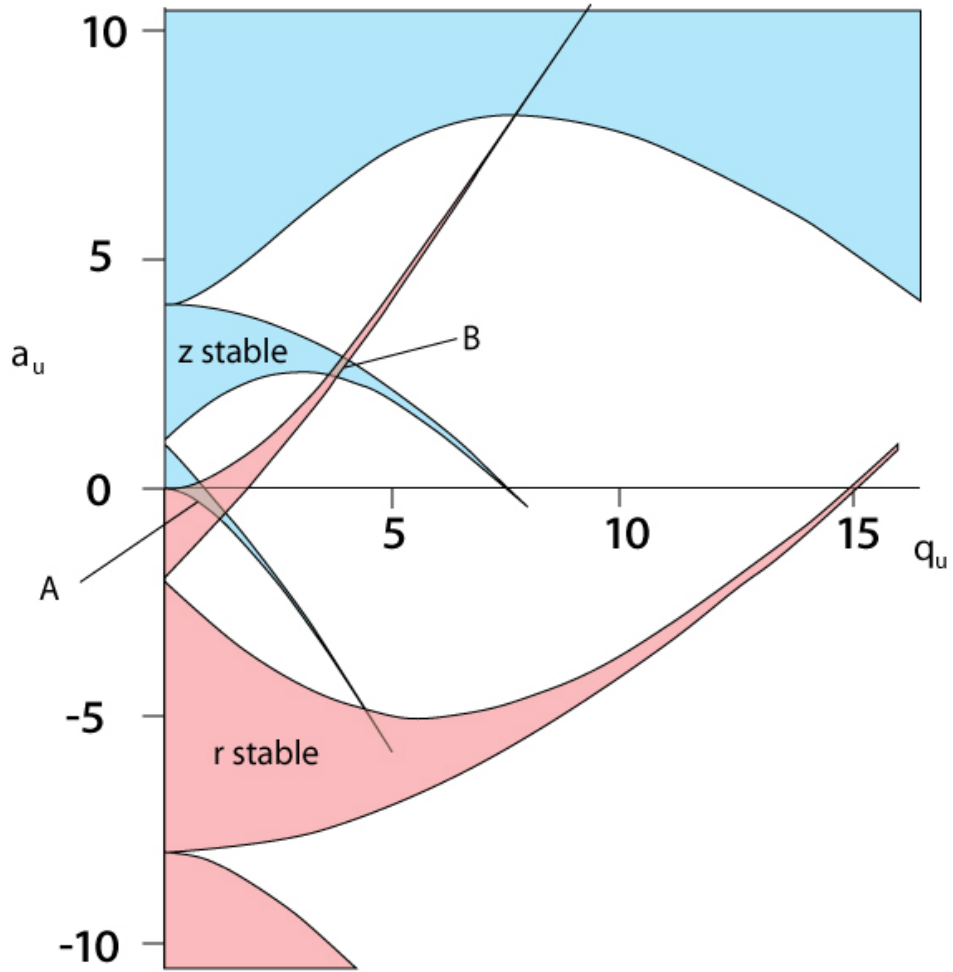


Figure 1.3. Plot in a and q space indicating when the trajectory of a charged particle is repeated and stable within an oscillating electric field.

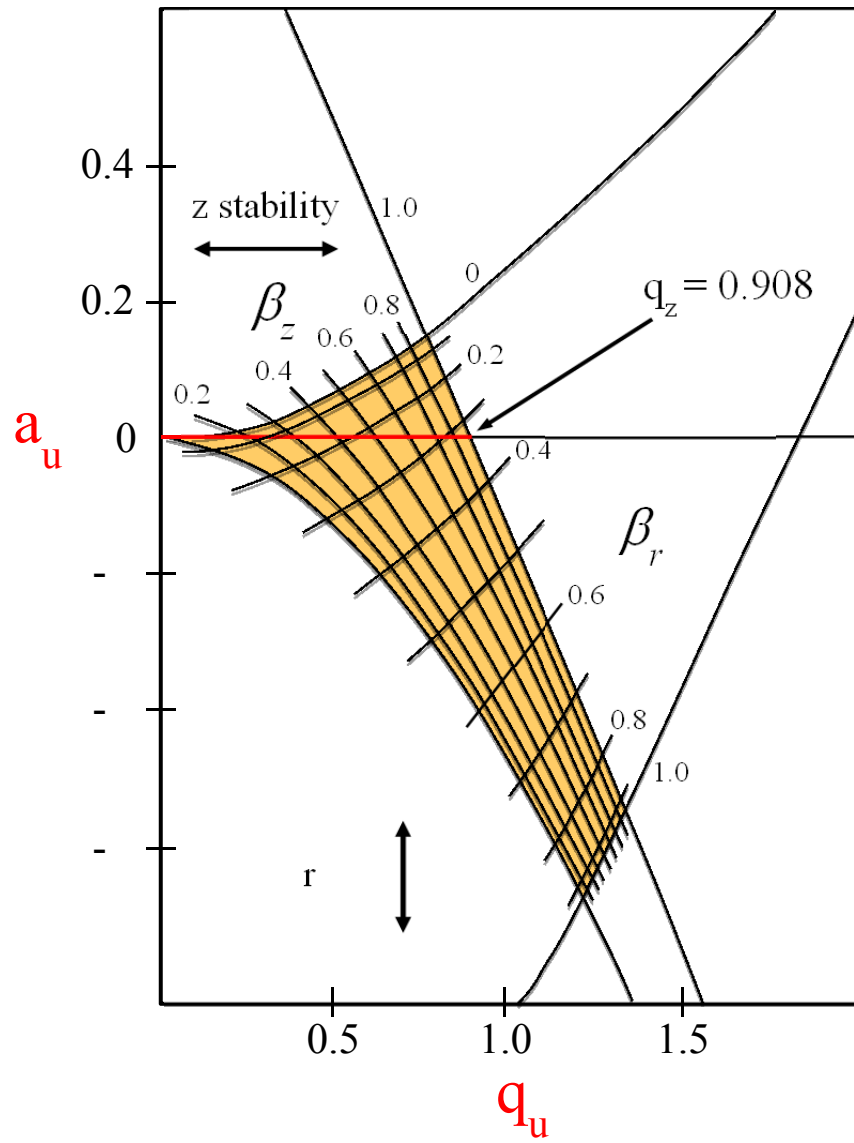


Figure 1.4. Detailed plot of the stability area typically used for ion trap mass spectrometry.

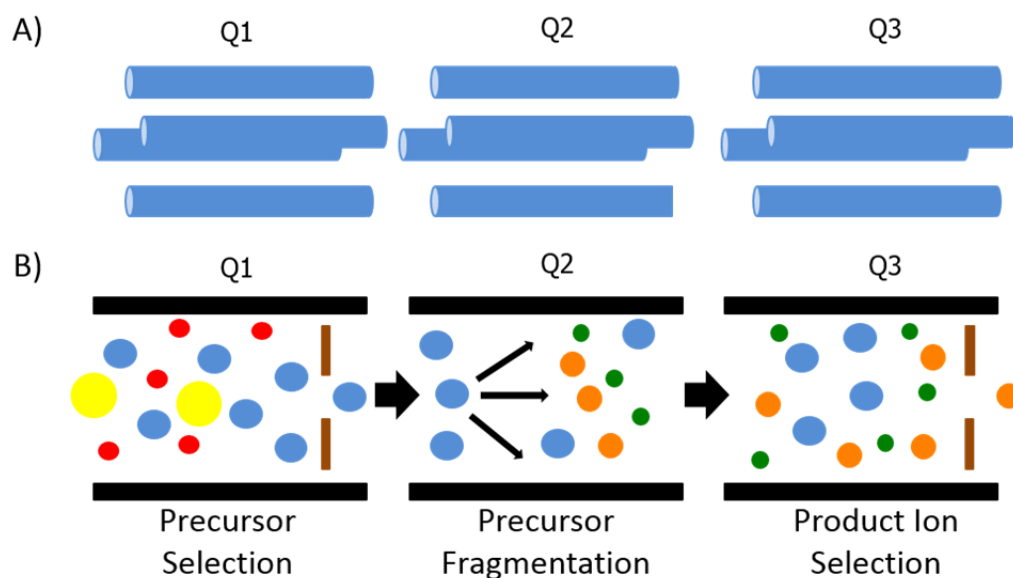
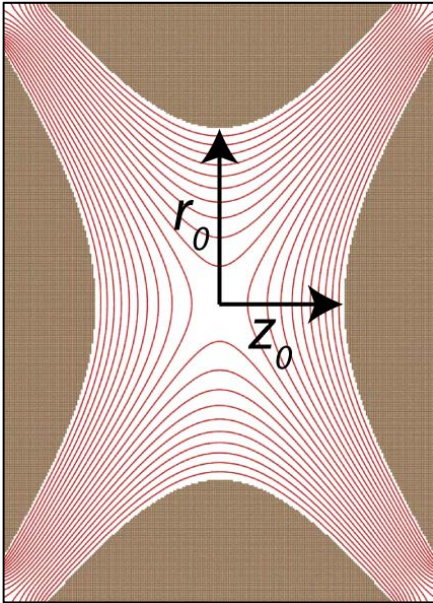


Figure 1.5. A) Example illustration of the electrode arrangement in a triple quadrupole instrument. B) Example of a tandem mass spectrometry experiment using this configuration. Ions of various mass-to-charge ratios (yellow, blue, and red) are injected from the ionization source. Q1 acts as a mass filter and passes only blue ions. In Q2, fragmentation occurs, and ions of all sizes are passed. Q3 also acts as a mass filter and allows only ions of a certain mass-to-charge to hit the detector.

A)



B)

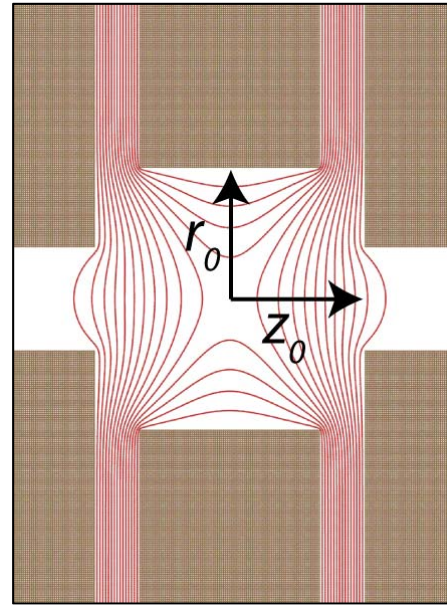


Figure 1.6. Plot of the isopotential lines resulting from (A) abbreviated hyperbolic geometry electrodes and (B) cylindrical geometry electrodes.

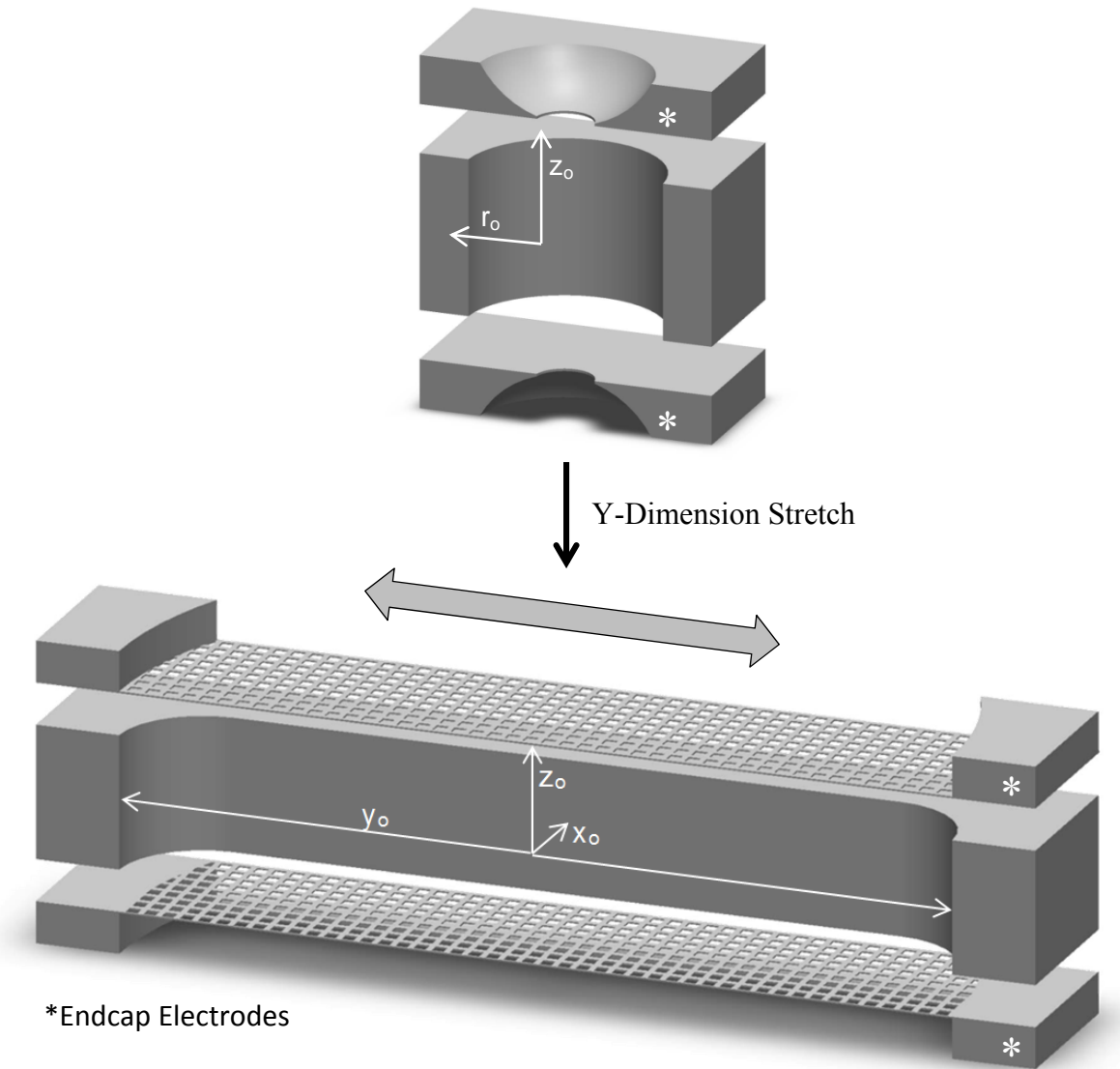


Figure 1.7. Illustration of fabricated CIT electrodes and SLIT electrodes, which are similar, but the SLIT features an elongated Y-axis.

1.6 REFERENCES

1. Lawrence, R.T., et al., *Plug-and-play analysis of the human phosphoproteome by targeted high-resolution mass spectrometry*. Nat Meth, 2016. **13**(5): p. 431-434.
2. Boix, C., et al., *High resolution mass spectrometry to investigate omeprazole and venlafaxine metabolites in wastewater*. Journal of Hazardous Materials, 2016. **302**: p. 332-340.
3. Wang, Q., C. Mesaros, and I.A. Blair, *Ultra-high sensitivity analysis of estrogens for special populations in serum and plasma by liquid chromatography–mass spectrometry: Assay considerations and suggested practices*. The Journal of Steroid Biochemistry and Molecular Biology.
4. Guo, X., et al., *Capillary Electrophoresis–Nanoelectrospray Ionization–Selected Reaction Monitoring Mass Spectrometry via a True Sheathless Metal-Coated Emitter Interface for Robust and High-Sensitivity Sample Quantification*. Analytical Chemistry, 2016. **88**(8): p. 4418-4425.
5. Lombard-Banek, C., S.A. Moody, and P. Nemes, *Single-Cell Mass Spectrometry for Discovery Proteomics: Quantifying Translational Cell Heterogeneity in the 16-Cell Frog (*Xenopus*) Embryo*. Angewandte Chemie International Edition, 2016. **55**(7): p. 2454-2458.
6. Williamson, J.C., et al., *High-performance hybrid Orbitrap mass spectrometers for quantitative proteome analysis: Observations and implications*. PROTEOMICS, 2016. **16**(6): p. 907-914.
7. Gillet, L.C., A. Leitner, and R. Aebersold, *Mass Spectrometry Applied to Bottom-Up Proteomics: Entering the High-Throughput Era for Hypothesis Testing*. Annual Review of Analytical Chemistry, 2016(0).
8. Rowland, C.E., et al., *Nanomaterial-based sensors for the detection of biological threat agents*. Materials Today.
9. Lin, S., et al., *Ultrasensitive microchip based on smart microgel for real-time online detection of trace threat analytes*. Proceedings of the National Academy of Sciences, 2016. **113**(8): p. 2023-2028.

10. Ma, Q., et al., *Rapid analysis of synthetic cannabinoids using a miniature mass spectrometer with ambient ionization capability*. *Talanta*, 2015. **142**: p. 190-196.
11. Chen, C.-H., et al., *Design of portable mass spectrometers with handheld probes: aspects of the sampling and miniature pumping systems*. *Journal of The American Society for Mass Spectrometry*, 2015. **26**(2): p. 240-247.
12. Smith, J.N., R.J. Noll, and R.G. Cooks, *Facility monitoring of chemical warfare agent simulants in air using an automated, field-deployable, miniature mass spectrometer*. *Rapid Commun. Mass Spectrom.*, 2011. **25**(10): p. 1437-1444.
13. Blakeman, K.H., et al., *High Pressure Mass Spectrometry: The Generation of Mass Spectra at Operating Pressures Exceeding 1 Torr in a Microscale Cylindrical Ion Trap*. *Analytical Chemistry*, 2016. **88**(10): p. 5378-5384.
14. Blakeman, K.H., et al., *High pressure mass spectrometry of volatile organic compounds with ambient air buffer gas*. *Rapid Communications in Mass Spectrometry*, 2017. **31**(1): p. 27-32.
15. Waridel, P., et al., *Evaluation of quadrupole time-of-flight tandem mass spectrometry and ion-trap multiple-stage mass spectrometry for the differentiation of C-glycosidic flavonoid isomers*. *Journal of Chromatography A*, 2001. **926**(1): p. 29-41.
16. Ferreres, F., R. Llorach, and A. Gil-Izquierdo, *Characterization of the interglycosidic linkage in di-, tri-, tetra- and pentaglycosylated flavonoids and differentiation of positional isomers by liquid chromatography/electrospray ionization tandem mass spectrometry*. *Journal of Mass Spectrometry*, 2004. **39**(3): p. 312-321.
17. Kushnir, M.M., et al., *Assessing analytical specificity in quantitative analysis using tandem mass spectrometry*. *Clinical Biochemistry*, 2005. **38**(4): p. 319-327.
18. Louris, J.N., et al., *New scan modes accessed with a hybrid mass spectrometer*. *Analytical Chemistry*, 1985. **57**(14): p. 2918-2924.
19. Jedrychowski, Mark P., et al., *Detection and Quantitation of Circulating Human Irisin by Tandem Mass Spectrometry*. *Cell Metabolism*, 2015. **22**(4): p. 734-740.
20. Zhang, B., L. Kall, and R.A. Zubarev, *DeMix-Q: Quantification-centered Data Processing Workflow*. *Molecular & Cellular Proteomics*, 2016.

21. Muratovic, A., et al., *Quantitative Analysis of Staphylococcal Enterotoxins A and B in Food Matrices Using Ultra High-Performance Liquid Chromatography Tandem Mass Spectrometry (UPLC-MS/MS)*. *Toxins*, 2015. **7**(9): p. 3637.
22. Anumol, T. and S.A. Snyder, *Rapid analysis of trace organic compounds in water by automated online solid-phase extraction coupled to liquid chromatography–tandem mass spectrometry*. *Talanta*, 2015. **132**: p. 77-86.
23. Sidell, F.R. and J. Borak, *Chemical warfare agents: II. nerve agents*. *Annals of Emergency Medicine*, 1992. **21**(7): p. 865-871.
24. Kim, K., et al., *Destruction and Detection of Chemical Warfare Agents*. *Chemical Reviews*, 2011. **111**(9): p. 5345-5403.
25. Chauhan, S., et al., *Chemical warfare agents*. *Environmental Toxicology and Pharmacology*, 2008. **26**(2): p. 113-122.
26. Castillo, M., et al., *Characterization of organic pollutants in industrial effluents by high-temperature gas chromatography–mass spectrometry*. *TrAC Trends in Analytical Chemistry*, 1999. **18**(1): p. 26-36.
27. Kientz, C.E., *Chromatography and mass spectrometry of chemical warfare agents, toxins and related compounds: state of the art and future prospects*. *Journal of Chromatography A*, 1998. **814**(1–2): p. 1-23.
28. Audi, J., et al., *Ricin poisoning: A comprehensive review*. *JAMA*, 2005. **294**(18): p. 2342-2351.
29. Dacre, J.C. and M. Goldman, *Toxicology and pharmacology of the chemical warfare agent sulfur mustard*. *Pharmacological Reviews*, 1996. **48**(2): p. 289-326.
30. Bartelt-Hunt, S.L., D.R.U. Knappe, and M.A. Barlaz, *A Review of Chemical Warfare Agent Simulants for the Study of Environmental Behavior*. *Critical Reviews in Environmental Science and Technology*, 2008. **38**(2): p. 112-136.
31. Noort, D., H.P. Benschop, and R.M. Black, *Biomonitoring of Exposure to Chemical Warfare Agents: A Review*. *Toxicology and Applied Pharmacology*, 2002. **184**(2): p. 116-126.

32. Eiceman, G.A. and J.A. Stone, *Peer Reviewed: Ion Mobility Spectrometers in National Defense*. Analytical Chemistry, 2004. **76**(21): p. 390 A-397 A.
33. Mäkinen, M.A., O.A. Anttalainen, and M.E.T. Sillanpää, *Ion Mobility Spectrometry and Its Applications in Detection of Chemical Warfare Agents*. Analytical Chemistry, 2010. **82**(23): p. 9594-9600.
34. Hill, H.H., W.F. Siems, and R.H. St. Louis, *Ion mobility spectrometry*. Analytical Chemistry, 1990. **62**(23): p. 1201A-1209A.
35. Hill, H.H. and G. Simpson, *Capabilities and limitations of ion mobility spectrometry for field screening applications*. Field Analytical Chemistry & Technology, 1997. **1**(3): p. 119-134.
36. Li, F., et al., *Ion mobility spectrometer for online monitoring of trace compounds*. Spectrochimica Acta Part B: Atomic Spectroscopy, 2002. **57**(10): p. 1563-1574.
37. Xu, J., W. Whitten, and J. Ramsey, *Pulsed-ionization miniature ion mobility spectrometer*. Analytical chemistry, 2003. **75**(16): p. 4206-4210.
38. Stafford, G., *Ion trap mass spectrometry: a personal perspective*. Journal of the American Society for Mass spectrometry, 2002. **13**(6): p. 589-596.
39. Paul, W. and H. Steinwedel, *A New Mass Spectrometer without a Magnetic Field*. Zeitschrift fuer Naturforschung, 1953. **a8**: p. 448-450.
40. Haywood, S., et al., *Containment device*. 1962, Google Patents.
41. Penning, F.M., *Die glimmentladung bei niedrigem druck zwischen koaxialen zylindern in einem axialen magnetfeld*. Physica, 1936. **3**(9): p. 873-894.
42. March, R.E., *Quadrupole ion traps*. Mass Spectrom. Rev., 2009. **28**(6): p. 961-989.
43. March, R.E., *An Introduction to Quadrupole Ion Trap Mass Spectrometry*. J. Mass Spectrom., 1997. **32**(4): p. 351-369.

44. Major, F.G. and H.G. Dehmelt, *Exchange-Collision Technique for Rf Spectroscopy of Stored Ions*. Phys. Rev., 1968. **170**(1): p. 91-107.
45. Mathieu, E., *Mémoire sur le mouvement vibratoire d'une membrane de forme elliptique*. J. Math. Pure Appl., 1868. **13**: p. 137-203.
46. Todd, J.F.J., G. Lawson, and R.F. Bonner, *CHAPTER VIII - QUADRUPOLE ION TRAPS A2 - DAWSON, PETER H*, in *Quadrupole Mass Spectrometry and its Applications*. 1976, Elsevier. p. 181-224.
47. Dawson, P.H. and N.R. Whetten, *Ion Storage in Three-Dimensional, Rotationally Symmetric, Quadrupole Fields. I. Theoretical Treatment*. Journal of Vacuum Science & Technology, 1968. **5**(1): p. 1-10.
48. Dawson, P.H. and N.R. Whetten, *Ion Storage in Three-Dimensional, Rotationally Symmetric, Quadrupole Fields. II. A Sensitive Mass Spectrometer*. Journal of Vacuum Science & Technology, 1968. **5**(1): p. 11-18.
49. Syka, J.E.P., *Chapter 4 - Commercialization of the Quadrupole Ion Trap*. Practical Aspects of Ion Traps Mass Spectrometry, 1995. **1**: p. 169-205.
50. Stafford Jr, G.C., et al., *Recent improvements in and analytical applications of advanced ion trap technology*. Int. J. Mass Spectrom. Ion Processes, 1984. **60**(1): p. 85-98.
51. March, R.E. and J.F. Todd, *Quadrupole Ion Trap Mass Spectrometry*. 2005: Wiley.
52. Kaiser, R.E., et al., *Extending the mass range of the quadrupole ion trap using axial modulation*. Rapid Communications in Mass Spectrometry, 1989. **3**(7): p. 225-229.
53. Goeringer, D.E., et al., *Theory of high-resolution mass spectrometry achieved via resonance ejection in the quadrupole ion trap*. Anal. Chem., 1992. **64**(13): p. 1434-1439.
54. Johnson, J.V., et al., *Tandem-in-space and tandem-in-time mass spectrometry: triple quadrupoles and quadrupole ion traps*. Analytical Chemistry, 1990. **62**(20): p. 2162-2172.
55. Louris, J.N., et al., *Instrumentation, applications, and energy deposition in quadrupole ion-trap tandem mass spectrometry*. Analytical Chemistry, 1987. **59**(13): p. 1677-1685.

56. Gao, L., R.G. Cooks, and Z. Ouyang, *Breaking the Pumping Speed Barrier in Mass Spectrometry: Discontinuous Atmospheric Pressure Interface*. *Anal. Chem.*, 2008. **80**(11): p. 4026-4032.
57. Misharin, A., et al., *Development and characterization of a field-deployable ion-trap mass spectrometer with an atmospheric pressure interface*. *Analytical chemistry*, 2012. **84**(22): p. 10105-10112.
58. Li, L., et al., *Mini 12, Miniature Mass Spectrometer for Clinical and Other Applications • Introduction and Characterization*. *Analytical chemistry*, 2014. **86**(6): p. 2909-2916.
59. Whitten, W.B., P.T. Reilly, and J.M. Ramsey, *High-pressure ion trap mass spectrometry*. *Rapid Commun. Mass Spectrom.*, 2004. **18**(15): p. 1749-52.
60. Arnold, N.S., G. Hars, and H.L.C. Meuzelaar, *Extended theoretical considerations for mass resolution in the resonance ejection mode of quadrupole ion trap mass spectrometry*. *Journal of the American Society for Mass Spectrometry*, 1994. **5**(7): p. 676-688.
61. Song, Q., et al., *Ion trap mass analysis at high pressure: an experimental characterization*. *J. Mass Spectrom.*, 2010. **45**(1): p. 26-34.
62. Xu, W., et al., *Ion trap mass analysis at high pressure: a theoretical view*. *J. Am. Soc. Mass Spectrom.*, 2009. **20**(11): p. 2144-53.
63. Paschen, F., *Ueber die zum Funkenübergang in Luft, Wasserstoff und Kohlensäure bei verschiedenen Drucken erforderliche Potentialdifferenz*. *Annalen der Physik*, 1889. **273**(5): p. 69-96.
64. Moxom, J., et al., *Sample pressure effects in a micro ion trap mass spectrometer*. *Rapid Commun. Mass Spectrom.*, 2004. **18**(6): p. 721-723.
65. Kaiser, R.E., et al., *Operation of a quadrupole ion trap mass spectrometer to achieve high mass/charge ratios*. *International Journal of Mass Spectrometry and Ion Processes*, 1991. **106**: p. 79-115.
66. Lammert, S.A., et al., *Miniature Toroidal Radio Frequency Ion Trap Mass Analyzer*. *J. Am. Soc. Mass Spectrom.*, 2006. **17**(7): p. 916-922.

67. Wells, J.M., E.R. Badman, and R.G. Cooks, *A Quadrupole Ion Trap with Cylindrical Geometry Operated in the Mass-Selective Instability Mode*. Anal. Chem., 1998. **70**(3): p. 438-444.
68. Patterson, G.E., et al., *Miniature Cylindrical Ion Trap Mass Spectrometer*. Anal. Chem., 2002. **74**(24): p. 6145-6153.
69. Riter, L.S., et al., *Analytical performance of a miniature cylindrical ion trap mass spectrometer*. Anal. Chem., 2002. **74**(24): p. 6154-6162.
70. Schultze, K., *Advanced System Components for the Development of a Handheld Ion Trap Mass Spectrometer*. Dissertation, University of North Carolina at Chapel Hill, 2014.
71. Ramsey, J.M. and K. Schultze, *Miniature charged particle trap with elongated trapping region for mass spectrometry*. 2014, Google Patents.

Chapter 2: Trapped Ion Behavior at High Pressures

2.1 Introduction:

Neutral buffer gas molecules play an important role in the operation of quadrupole ion traps.¹ Although early theoretical work was developed for the uninterrupted motion of charged particles in oscillating electric fields,² it was quickly discovered that some background pressure enhanced performance. Gains in sensitivity and resolution resulted from operation with ~1 mTorr neutral buffer gas,³ which was typically helium. Due to collisions with these neutral background molecules, trapped ions lose kinetic energy.⁴ This impediment to motion causes a relaxation of the trapped ions such that they “cool” to the center of the trap. This phenomenon means that ions that would otherwise be outside the trapping volume are successfully trapped.⁵ It also prevents the spurious excitation of undesired ions by unwanted effects, such as the non-idealities in the electric field that frequently occur near the electrodes.⁶ In essence, the role of these neutral molecules is understood to be a dampening term on the motion of the trapped ions.

While collisional cooling effects can be beneficial to mass spectrometry, some deleterious impacts also arise from the disruptive nature of the collisions.^{7,8} The secular frequency of trapped ions is an important characteristic, but its fidelity can be adversely affected by collisions with neutrals.⁹ The secular frequency is defined by repeated motion within the trap,⁴ and random collisions alter that trajectory by affecting both the direction and magnitude of the ion’s velocity. As the number of collisions rises per repeated cycle of the motion, the

behavior of the ion becomes less well defined. Ion cooling from elevated pressures may also confine the ions to a tighter cloud, increasing the role of space-charge effects in distorting the secular frequency.¹⁰ There have also been suggestions that the stability region is significantly affected by pressure.^{9, 11} For these reasons, pressure above the traditional 1 mTorr has been viewed as a hindrance to attaining quality mass spectra.¹²

High pressure mass spectrometry (HPMS), however, brings ion trap operation to a pressure regime with significantly increased numbers of collisions between ions and neutral buffer gas molecules. With around 1 Torr of background gas in HPMS, collisions should play a dominating role in ion trap behavior. Discussed in this chapter are experiments focused on characterizing the effects of collisions on trapped ions under HPMS conditions. First, effective trapping conditions are displayed via stability plots for cylindrical ion traps (CITs) and stretched length ion traps (SLITs). These diagrams are then compared at low (10 mTorr) and high pressures (1 Torr). Furthermore, the characteristics of resonant ejection are studied as a function of pressure. Resonant ejection mass spectra are shown across a broad range of resonant conditions and pressures.

2.2 Stability Diagram Analysis

As discussed in Chapter 1 and reshowed in Figure 2.1, stability diagrams are two-dimensional plots representing the parameter space in which a given ion can be successfully trapped by an oscillating electric field. Experimentally generated stability diagrams can provide important information about an ion trap in a variety of ways.¹³⁻¹⁵ The plots are traditionally constructed with axes of a and q ; these serve to bring several important variables into a well-defined, unit-free space.^{4, 16} Included in these variables are the ion mass-to-charge ratio, trap

geometry, RF drive frequency, RF drive voltage and DC voltage applied to the ring electrode. For our purposes, the ion mass-to-charge ratio, trap geometry and RF drive frequency are held constant as they are not easily changed within the time scale of a single mass spectrum. To adjust the a parameter, one can manipulate the DC voltage applied to the ring electrode relative to the endcaps while the q parameter can be similarly controlled by the RF voltage applied to the ring electrode. Consequently, it is straightforward to test whether or not a specific mass-to-charge ion is stable at given definitions of a and q , then plot those results to create experimental stability diagrams.

Noted above, ion trapping efficiencies or ion population decay after trapping may reveal information about the pseudopotential well depth in the trap. Insights from this data are mostly qualitative in nature as the only information gained is relative to other points within the stability region. Historically, stability diagram experiments have also been used to reveal resonance conditions related to the geometry of the trap. At certain β values, ions have been noticed to eject from the trap due to the resonant interactions between secular frequency and nonlinear resonances stemming from non-quadrupolar field lines in the trap.¹⁷ Note that any trap geometry other than purely hyperbolic electrodes will have trapping fields with contributions from higher order terms. These effects will be of possible interest when analyzing the data.

The boundaries of the stability diagram also provide important information about a trap. Since a traditional mass selective instability scan is performed by traversing the ions through a - q parameter space across one of the boundary lines, the sharpness of that boundary condition is an important factor in defining mass spectral resolution. If the boundary condition is more gradient in nature than a well-defined limit, ion ejection may behave as a slow leak of ions, causing widening of peaks. Fine sampling around these regions may show if any parameters, such as

pressure, play prominent roles in the definition of these stability boundaries. The actual shape of the stability region may also reveal important characteristics about the ion trap. Beyond simply elucidating a range of acceptable RF and DC values for trapping, the symmetry (or asymmetry) of the stability region reflects the nature of the ion trap. Conventional 3-dimensional traps such as the CIT have stability regions like those discussed in the Chapter 1 and shown in Figure 2.1. Linear ion traps, an alternative trapping geometry, have stability regions that are symmetric around the $a = 0$ axis.¹⁸⁻²⁰ The stretched length ion trap (SLIT) has been hypothesized to function in the manner of a linear ion trap,²¹ so experimentally mapping its stability region is an opportunity to probe their behavior.

To experimentally map a stability region, there are a few important choices to consider with regards to accumulating and then detecting the ions. First, the initial ion population may be acquired in one of two ways. The ions may be accumulated either at the (a, q) coordinate being tested²² or under a standardized set of conditions before then being moved to the (a, q) point of interest.²³ Representative timing diagrams for these strategies are depicted in Figure 2.4. Second, the stable ion population may be measured in multiple ways. The entire ion population can be ejected towards the detector either via a quick DC pulse on an endcap or via a traditional mass spectral scan. Detecting the ions with a sharp DC pulse rapidly quantifies the entire trapped ion population, which may be beneficial in isolating the factors leading to ion loss. Generating an entire mass spectrum, however, collects information about mass bias or fragmentation. Furthermore, a targeted analysis is possible by integrating only a peak of interest from the mass spectra, while also collecting mass information. Therefore, generating the entire mass spectrum was the method chosen for ion ejection.

For ion accumulation strategies, there are a few important implications that result from the specific strategy chosen. If the trap is set to the a and q values of interest before ion acquisition, these starting conditions will govern the number of ions successfully trapped. When set to values outside the boundary conditions of the stability region, no ions will ever be trapped. Furthermore, the ion trapping efficiency, when inside the stability region, will be dependent on the pseudopotential well depth. Experiments conducted in this mode, therefore, may provide data that elucidates how the well depth varies over the stability region. Furthermore, by acquiring ions at the a, q coordinate of interest, it is assured that trapped ions are truly affected by that particular set of RF and DC conditions, rather than by the intermediate conditions between the starting values and the point being tested. For example, if ions are acquired at $a_z = 0, q_z = 0.4$, but the test point is $a_z = 0.1, q_z = 0.5$, the ion population will either move through intermediate values of a and q , or be immediately moved via a sudden change in the system. If the intermediate values include a resonance, there is a possibility for ion excitation and loss. Furthermore, there is the possibility that the intermediate values lie outside the stability region despite both initial and final coordinates being stable trapping conditions.

There are also advantages, however, to the method of acquiring ions at the same a, q coordinate for each experiment. Primarily, a controlled number of ions are included in each experiment. This effect means that space-charge effects are consistent across all experiments. It also means that trapping efficiency, which may be a function of more variables than just pseudopotential well depth, is not a factor. Also, in order to create a mass spectrum, ions are scanned across the $q_z = 0.908$ boundary, meaning the ions already will experience a selection of a - q space beyond the single coordinate of interest. Preliminary data suggested, however, that simply moving the ions across the parameter space at a moderate pace does not cause ion

ejection. This tolerance means that it is reasonable to acquire all ions at a standardized ion accumulation a, q coordinate, adjust the RF and DC potentials to the a, q point of interest with a brief period of time at these coordinates for unstable ions to leave the trap. This is then followed by a return to the initial a, q coordinates and a mass selective instability scan.

2.2.1 Instrumental Design

High pressure mass spectrometry requires custom instrumentation that has been designed in this laboratory to maximize its flexibility over a broad range of variables.^{24, 25} Nearly all mass spectrometers use electron multipliers as detectors due to their high gain and large bandwidth. A major constraint to electron multipliers, however, is that they are not pressure tolerant. For this reason, a differential chamber technique was used such that ionization and mass analysis was performed in a high pressure region while detection was accomplished in a low pressure region with an electron multiplier. The electrodes of the ion trap itself serve as the conductance limit between the high and low pressure sides. An example of this instrumentation is shown in Figure 2.2 with an exploded view of stacked trap electrodes, a glow discharge ionization source, and an electron multiplier detector. Two versions of instrumentation were used for experiments in this work: a benchtop differential chamber system and a mini differential chamber system.

The benchtop differential chamber was a custom designed vacuum system (approximately 12 cm x 15 cm x 25 cm) with appropriate electrical feedthroughs for the operational strategy shown in Figure 2.3. The detection chamber was pumped with an Agilent TPS compact turbopump, backed by an Agilent SH-110 roughing pump (not shown). A second set of the same model of pumps was also attached to the mass analysis chamber. A conductance

limiting valve was used to control the pumping speed on the mass analysis chamber. A mass flow controller (FMA5408, Omega) was used to introduce either helium or nitrogen background gas. When air was used as the buffer gas, a simple series of needle valves leading to the ambient atmosphere was used as an inlet. By controlling the flow rate of the gas being introduced and the conductance on the pumping exit, it was possible to adjust the pressure within the mass analysis chamber. Pressure measurements were made with a capacitance manometer (627D, MKS, Andover, MA).

For helium or nitrogen buffer gas experiments, a precision leak valve (ULV-150, MDC Vacuum Products, Hayward, CA) was used to introduce analyte at an uncorrected pressure of around 10^{-5} Torr, measured by a full range vacuum gauge (FRG-700, Agilent). With the atmospheric inlet for air buffer gas experiments, the volatile compound was leaked into the chamber through a third needle valve, parallel to the outer valve controlling the air inlet. For low vapor pressure samples, a heating tape (40-60 °C) was wrapped around the test vial to improve signal intensity.

For experiments in helium and nitrogen, ionization was achieved via electron impact with a tungsten filament as the electron source. The accelerating voltage was scaled from -70 to -225 V as pressure increased in order to ensure the electrons reached the trapping volume with sufficient kinetic energy to induce ionization. The filament required between 1.7 and 2.2 A of current to generate sufficient electron flux. A gating lens between the filament and the trap was used to control timing. The tungsten filament, however, is extremely intolerant of oxygen. For experiments in air, therefore, a glow discharge electron source was developed. The source consisted of two circular ~1-inch steel electrode plates separated by a 1-cm Teflon spacer. To control the timing, the voltage on the electrode furthest from the trap was pulsed, stopping and

starting the glow discharge. The electrode nearest the ion trap served also to generate the electric field for accelerating electrons which had escaped the plasma towards the trap through a hole in that electrode. Glow discharge is much more tolerant of oxygen and high pressures, but the source is tuned for a particular pressure and is only able to form the necessary plasma within a certain range (~400-1500 mTorr).

Mini differential chamber systems consist of significantly smaller vacuum chambers (approximately 2.5 cm x 2.5 cm x 9 cm), with an internal volume of under 5 cm³. They were designed for high pressure operation in air, so glow discharge was used as the ionization source. While primarily used as an electron source for electron impact, it can also be used as a primary ion source by placing a positive bias on the electrode nearest the ion trap. In mini systems, the sample introduction was as described above for an air inlet.

For mass analysis, a cylindrical ion trap was constructed by stacking three metal electrodes separated by Kapton or Teflon insulators. Ring electrodes were 0.790 mm thick copper with a trap radius of 0.500 mm while endcap electrodes were beryllium copper with 0.200 mm radius apertures. The insulating spacers were 0.250 mm thick.

With all systems, timing and voltages were controlled from a custom LabVIEW program interfacing with National Instruments hardware (NI PXI-6733, NI PXI-6122). RF for the ion trap was enhanced with a tuned tank circuit using the trap as the capacitive load. The RF signal started from a signal generator (SMB100A, Rohde and Schwarz), underwent an initial amplification by an RF preamplifier (TVA-R5-13, Mini-Circuits), was further amplified by an AR305 power amplifier, and resonated with the trap via a custom built inductor. The inductance value can be adjusted to tune the resonant frequency of the circuit. Gain is high enough to achieve up to 1000 V_{0-P} in many cases. In this chapter, RF was tuned to near 7 MHz for each

experiment. Supplemental AC is applied directly from an arbitrary function generator (AFG3022, Tektronix). Voltage for the electron multiplier detector (2300, DeTech) is generated from a custom high voltage pulser, and the signal is transduced through a current-to-voltage preamplifier (SR570, Stanford Research Systems) with a gain between 50 and 200 nA/V.

To generate the experimental data discussed in this section, custom software was created. A control script was made to sequentially adjust the RF voltage and DC potentials during the relevant sections of the scan function. The script was given a low value, a high value, and a step size for each of the RF and DC domains. DC was scanned from -10 to 40 V in 2 V increments while RF was scanned from ~100-750 V_{p-p} in ~50 V increments. The program iterated through these values sequentially, inserting a few control experiments for monitoring any drift from the ionization source or sample introduction. Custom software also was made to integrate the mass peak of interest for each spectrum, resulting in an array of numbers representing the ion intensity at a specific a, q coordinate. The chosen analyte was N,N-dimethylaniline, and the molecular ion (m/z 121) was used as the indicator. Corrections to the intensities could be made based on the drift of the ionization source as determined from the interjected control experiments. This corrected array was turned into a false color plot for visual interpretation.

2.2.2 Pressure Effects on Stability Regions

The first set of experiments was conducted with the strategy of accumulating ions at different (a, q) locations around the stability region followed by ion ejection. A false color contour representation of an experimentally generated stability region at 1 Torr of air buffer gas is shown in Figure 2.5. The axes have been left in experimental variables (y-axis: DC voltage, x-axis: RF voltage) for ease of interpretation, but these correspond directly to the a and q terms

used to plot the theoretical stability diagrams, as in Figure 2.1. Blue areas correspond to no trapped ions, while white to red regions represent the integrated intensity (low to high) of ions trapped at those conditions. As can be seen from the figure, the region differs from the theoretical version in qualitative shape. Specifically, the RF voltage corresponding to the outer edge of stability (~ 570 V) is nearly constant over the range of DC values explored. In the theoretical diagrams (Figure 2.1), q_z (or in our case the RF voltage) increases significantly as a decreases. That is, the rightmost edge of the stability area is nearly vertical rather than sloping more gradually as in the theoretical plot. Furthermore, the stability region does not extend to the origin of the plot, which is the same point in a, q space as it is in DC, RF space. Of course, it is expected for there to be some variation between the experimental and the theoretical stability regions originating from both pressure and geometric effects. The geometries of cylindrical ion traps are quite different from the purely hyperbolic geometry used in generating the theoretical diagram. These differences lead to significant variation in electric fields, mostly due to contributions from higher order terms in the cylindrical geometry. These higher order fields manifest near the edges of the trapping volume and can significantly impact the motion of trapped ions, leading to the differences in the stability diagrams.

During normal MS operation, DC potentials are not used which means that ions only experience conditions along the $a = 0$ (or DC = 0) axis.²⁶ This means that the most important point of the right hand boundary is where it intersects this axis, as this defines the boundary ejection point. Other characteristics of the boundary, such as verticality, are useful for analyzing the trapping fields. There is, however, a significant impact on traditional operation that can be noted from the leftmost boundary of the stability region along the $a = 0$ axis. As noted above and predicted by simulations,¹¹ the boundary does not extend to the origin. Thus, ions with low q_z

values, i.e. high mass-to-charge ratio, are not stably trapped whereas in theoretical ion traps, there is no high mass limit for trapping ions. From the experimental data, however, ions are not detected at all with q values below ~ 0.3 , as calculated from RF values below $\sim 200 V_{P-P}$. Theory does predict a shallow pseudopotential well depth for an ion when the q value is very low, which is likely to explain the practical inability to trap these ions. The impact of this limit is that there is a finite mass window over which ions can be simultaneously trapped. Both operational frequency and pressure are likely to play important roles in determining this mass window. The impact of increased frequency on the stability diagram is to increase the pseudopotential well depth of an ion at the same q value, since a higher V is required to maintain that q value. This trend is likely to extend the stability region towards the origin and enlarge the mass window. Another important factor is pressure, which is investigated in the following experiments.

Ion accumulation efficiency is expected to be a result of multiple factors, including pseudopotential well depth. As seen in Figure 2.5, the regions of high intensity or higher accumulation efficiency of ions, shown in red, are near the left side of the stability region. Calculations, however, predict the deepest pseudopotential well should be achieved at a $q_z \approx 0.8$, near the right hand boundary of the stability region. Based on the voltages applied here, the maximum ionization efficiency is near $RF \approx 270 V_{P-P}$, $DC \approx 0 V$, which corresponds to $q_z \approx 0.45$, $a_z \approx 0$. Furthermore, during a mass spectral scan, the ions ejected near $\sim 600 V_{P-P}$ RF, which should correspond to the $q_z = 0.908$ point. The apparent boundary from this stability diagram is somewhat lower than this, near $\sim 570 V_{P-P}$. This discrepancy may be due to the higher RF voltages disrupting the trajectories of electrons during the ionization period. By preventing the electrons from entering the trap, the larger RF fields are inhibiting ion formation within the trap

despite the larger pseudopotential well depth meaning that any formed ions are more likely to be successfully trapped.

The effect of pressure on the stability region was further investigated at 500 and 1500 mTorr, and the results shown in Figure 2.6. The diagram in panel B (1500 mTorr) shows horizontal streaks, which are the result of inconsistent ionization capabilities at this pressure. These intensity artifacts makes it difficult to judge the trapping efficiency in the stability region. The overall shape of the plot, however, is still consistent with those generated at 500 and 1000 mTorr. By comparing the plots in Figures 2.5 and 2.6, for example, it is possible to see that over a range of 500-1500 mTorr, the shape of the stability region changes very little. The left-hand and right-hand boundaries appear too similar to draw any distinct conclusions. Literature suggestions, based on simulations, show competing trends of enlarging and shrinking stability regions based on pressure.^{9, 11} Neither effect is strongly supported by the data shown here, studied over a smaller pressure range.

The possible effects from higher order fields, which would result in areas of instability within the boundaries, are not seen in the data. While calculations from the trap geometry show a large contribution from non-quadrupolar fields, their impact on the stability region may be prevented for a variety of reasons. First, the resonance points may represent relatively narrow sets of conditions, while the experiment had large enough step sizes to miss some of these points. Based on some simulations and the sheer number of data points in the experiments, this under-sampling seems unlikely to be a complete explanation. A second, more convincing reason is that the high pressure of buffer gas in the trapping volume acted as a damper to prevent resonance excitation. Since higher order fields have their most significant impact near the edges of the trapping volume, the increased collisional cooling may have more closely confined the ions to

the center of the trap. Furthermore, the collisional dispersing of ion motion may have prevented the resonant overlap from being strong enough to cause ejection of otherwise stable ions.

The stability diagram was then generated with ion accumulation, as discussed previously, performed at a standardized set of a and q condition. To generate Figure 2.7, the ions were trapped at $a = 0.0$, $q = 0.4$, moved to the desired a and q values to be tested, held for 2 milliseconds for loss of unstable ions, then transferred back to the standardized a , q condition, followed by ejection past the boundary. This resulted in the stability region being enlarged in multiple dimensions. The left-hand boundary remains similar to that in Figure 2.5, but there is a much greater tolerance for DC voltage (at least 40 V vs. 20 V), and the right-hand boundary is pushed slightly towards higher voltages. The new right-hand boundary also lines up much better with the observed ejection voltages for ions, ~ 600 V_{P-P}, and the shape approaches that of the theoretical stability diagram. The power supplies used for the DC voltage were insufficient to investigate the bottom-most border of the stability region such that 40 V was the upper limit tested, but that mode is also quite far from normal modes of operation. Of note, the boundaries appear quite sharp and there is an almost binary feature of ions being preserved as long as they were moved within the stability region but being entirely lost outside the stability region.

To extend the range of pressures tested, a tungsten filament was used as the electron source at low pressures with helium as the buffer gas at 10 mTorr. The resulting stability region is shown in Figure 2.8. Again, the horizontal streaks in the plot are due to fluctuations in electron intensity coming from the filament over the several hours of experimentation. Importantly, despite the geometry of this ion trap being identical as those in prior experiments, the left-hand boundary is pushed to lower voltages. This effect also suggests that pressure does play an important role in the determining stable trapping conditions. It is likely that buffer gas

characteristics (e.g. mass) are the cause of this shift, although the role of buffer gas identity was not directly isolated in these experiments. The diagram in Figure 2.8 also does not reach to the origin of the plot, suggesting pressure is not the only variable limiting the mass window. It is also interesting that the boundaries, particularly the right-hand boundary, do not appear as distinct at these low pressures compared to high pressures, which would be expected to correspond to a loss of mass resolution. Most likely, these regions along the border simply have lower pseudopotential well depths, so ions are easily lost at low pressure, but sufficiently damped at high pressure.

2.2.3 Characterizing the Stability Region of SLITs

Experiments up to this point have focused on stability regions generated from cylindrical ion traps. The stretched length ion trap (SLIT) geometry with its larger trap volume, however, has been shown to improve sensitivity for high pressure mass spectrometry.²⁷ It is therefore of interest to explore the properties of this device, especially the range of stable trapping conditions. Figures 2.9 and 2.10 show results from analogous experiments to Figures 2.7 and 2.8, respectively. Comparing the 1 Torr and 10 mTorr results in Figure 2.9 and 2.10, the same differences are present as were seen for CITs at these pressures: the ionization stability is not as consistent, and the stability region is shifted to lower RF voltages on both boundaries.

Comparing the 1 Torr SLIT and CIT data in Figures 2.9 and 2.7, however, reveals some important variations. First, the right-hand boundary is pushed slightly towards higher RF voltages with a slight convex curve rather than a slant – the maximum stable RF value is with 0 V DC rather than with a strong positive DC. There also appears to be less tolerance for DC voltage with the SLIT trap. These are interesting characteristics, but it takes some analysis to

understand their full implications. It was discussed earlier that SLITs were believed to be two-dimensional traps in nature and that this style of trap has a stability diagram that is symmetric around the $a = 0$ axis. The stability regions shown in these figures are clearly asymmetric, so it seemed likely that there are strong three-dimensional characteristics to the trapping behavior of SLITs.

For comparison, a simulation of the stability region of a SLIT at 1 Torr is shown in Figure 2.11.²⁸ There is a strong agreement between the experimental and simulated data. The outline shapes are much the same, and significantly the simulation is also asymmetrical. One of the strengths of simulation compared to experiments, however, is the ability to investigate other factors involved with ion trapping. It is challenging to determine experimentally how unstable ions leave the trapping volume. With simulations, tracking ion positions is possible, and it was noted that not all instability conditions resulted in identical ion behavior. In Figure 2.12, for example, is a SIMION plot of ion trajectories when there is a strong negative DC component on the ring electrode. The ions remain stable in the x-z plane, but are unstable along the y-axis where they extend the length of the SLIT. Another way of stating this effect is that ions are trapped in two-dimensions and pulled out towards the ends of the SLIT by the attractive forces of the negative potential. In most other conditions of instability, the ions are in fact becoming unstable in either the x (width) or z (endcap to endcap) dimension. With this new information in mind, SLITs are truly behaving as two dimensional traps with the constraint that the endcaps are not held at ground as they would be in a conventional linear ion trap. This constraint abbreviated the upper region of the stability diagram by drawing the ions into the electrodes along the y-axis when they would otherwise be stable. Synthesizing all of this information has led to a much

deeper understanding of the SLIT and its behaviors. Future work in Chapter 3 will seek to further take advantage of these characteristics and potentially overcome some of the weaknesses.

2.3 Resonant Ejection Behavior Analysis

Resonant ejection, as discussed in Chapter 1, is a powerful tool in mass spectrometry. Briefly, by applying a supplemental AC potential to the endcaps of a trap, any ions that have secular motion at that same frequency will be resonantly excited. If the excited ions reach the edge of the trap, they will be ejected and likely detected. This technique can extend mass range,²⁹ improve resolution,³⁰ and be used for non-sequential ejections.³¹ In order to reach the point of ejection, however, resonant excitation must cause the ion to excuse to the edge of the trap. The increased collisions in HPMS systems are likely to inhibit that behavior by impeding the ions' velocity and by disrupting the fidelity of the secular motion. The experiments in this section explore the implications of increased pressure on resonant ejection.

One particular phenomenon observed with resonant ejection in miniature cylindrical ion traps, such as those in HPMS, is double resonance ejection.³² The first resonance in this case is between the secular frequency of the ion and the supplemental AC. The second resonance occurs with the nonlinear fields arising from the non-hyperbolic geometries within the trap. These nonlinear resonances are very intense in a cylindrical trap, which has many higher order field contributions by design, and in a miniaturized trap, where the higher order fields at the fringe of the geometry are closer to the ions. The double resonance conditions mean that there is a noticeable increase in signal intensity and resolution when resonant ejection is enacted at a

frequency corresponding to a nonlinear resonance within the trap. We explore the impact of pressure on this phenomenon in cylindrical ion traps in the following experiments.

The results from these experiments are represented in complex three-dimensional plots. The plots show stacked mass spectra, with each blue trace showing a mass spectrum captured at specific supplemental AC frequencies applied to the end cap with all other variables held constant. Between panes, a different supplemental AC voltage is applied and between figures (Figures 2.12-14), a different buffer gas pressure. All spectra are of pure xenon in helium, and since xenon is an atomic species, all peaks would be the result of an isotope rather than any possible fragmentation. This simplicity aids interpretation of results significantly. For comparison, boundary ejection spectra are seen in the A panel of each figure and show that there is some variation of signal intensity due to fluctuations in the electron flux from the tungsten filament.

Figure 2.13 shows data at 1 mTorr of helium buffer gas, which has been the historical condition for ion trap mass spectrometry. In panel A, there is very low (10 mV_{0-P}) supplemental AC, so every spectrum is just a boundary ejection spectrum of xenon. The peaks appear near the upper-left edge of the plot though there are also small ridges of signal at slightly lower ejection voltages, likely resulting from higher order fields in the trap. The subsequent panels show resonant ejection spectra of xenon with varied frequencies of supplemental AC. For the lower-right axis, supplemental AC frequency, as a fraction of drive RF ($\Omega = 7$ MHz), increases from right to left. Based solely on a direct resonance between this frequency and the secular frequency ω , one would expect the RF ejection voltage to increase as the AC frequency increases up to $\Omega/2$ (3.5 MHz). That feature is observed in panels B, C, and D. The maximum frequency of the secular motion, however, is $\Omega/2$. Once the supplemental AC frequency is above $\Omega/2$, the secular

frequency cannot be in direct resonance. On first pass, this effect would mean that there should only be boundary ejection when the supplemental AC frequency is above this threshold. Simulation data, however, has shown a strong (although weaker than the secular frequency) sideband motion at a frequency of $(\Omega - \omega)$. Data shows that this behavior is also observed experimentally, resulting in resonant ejection. This ejection tendency extends the horseshoe shape of the ejection profile above $AC / \Omega = 0.5$. Note that at supplemental AC frequencies near the drive RF frequency, there is no resonant ejection and the signal reverts to boundary ejection at the edge of the spectrum. This effect is due to the relative weakness of that sideband motion.

The spectra in Figure 2.13 vary drastically in intensity. There are multiple spectra where the signal is substantially enhanced as a result of double-resonance conditions. Overlapping these nonlinear resonances with the supplemental AC and the secular frequency of the ions leads to these substantial increases in signal. The exact location of these enhancements changes based on the intensity of the supplemental AC, as can be seen by comparing panel B ($0.50 V_{0-P}$), panel C ($1.0 V_{0-P}$), and panel D ($2.0 V_{0-P}$). Notice also that intensity scale bars change between plots due to the strong ion pulse at the rightmost corner, a result of the pulsed AC ejecting many ions right as it is turned on. In the short range of voltages used in this experiment, the larger AC voltage led to larger signal.

Figure 2.14 is an analogous experiment at 300 mTorr of helium buffer gas. Note there is a shift to higher RF voltages (350-750 V from 200 to 650 V) used due to a change in the functional mass window at this pressure. Panel A is again simply the boundary ejection spectra. Panel B is shown with $1.0 V_{0-P}$ supplemental AC as compared to $0.50 V_{0-P}$. At this higher pressure, increased AC voltages were required to produce similar results as those at lower pressures. Furthermore, there does not appear to be nearly the same variation along the horseshoe feature.

Although the ejection voltage changes with AC frequency, the signal and resolution were not affected significantly. Panel D does show one small area of no signal. This is likely an artifact from a temporary failure of either the ionization or the detector. Trends in the experiment, however, make it unlikely that there is significant information hidden in this region. Figure 2.15 is a further extension of the experiment, performed at 1 Torr of helium buffer gas. The data look very similar to that taken at 300 mTorr of helium in Figure 2.14, but in general required higher AC voltages to produce the same effect. Again, there is no significant variation in signal intensity, revealing a lack of double resonance points. At this high pressure, it is clear that it takes high voltages to effect ejection at these high frequencies of supplemental AC.

The trend emerging from these experiments is that pressure acts as a significant damper on resonant behavior in the ion traps. The supplemental AC voltage necessary to induce resonant ejection increases with pressure. Increased collisions between the ion and neutral buffer gas at higher pressures impede the acceleration of the ion and disrupt the characteristic secular frequency, resulting in a two-pronged damping effect. Furthermore, double resonant characteristics are almost non-existent at high pressures. Since the higher order fields are unchanging, how the ions are experiencing the trapping fields must be a function of pressure. The higher pressures appear to be cooling the ions to the center of the trap, limiting their exposure to the higher order fields near the edges. Even once the ions have begun excitation, the pressure is likely preventing the ions from experiencing some of the fringing fields at the edge of the trap. The result is that a microscale ion trap with non-ideal geometries actually behaves more similarly to a purely hyperbolic trap as pressure increases. While double-resonant behavior has been an effective tactic for improving resolution and sensitivity in microscale traps, it is shown

to be incompatible with high pressures. Resonant ejection, however, is shown to behave very similar to theoretical predictions provided a high enough amplitude.

2.4 Conclusions

This chapter investigated the behavior of trapped ions and how those behaviors are affected by pressure. Stability regions at high pressures were experimentally mapped and compared to their low pressure counterparts, showing a reduction of mass window, but a preservation of sharp boundaries, high efficiency ion preservation, and adherence to theoretical predictions. The stability region for SLIT geometries was also explored. Experimental data and simulations revealed the two-dimensional trapping characteristics of the SLIT. Future experimentation could pursue more geometries of traps as well as additional types of ions. It would be possible to add small dimensional changes to a CIT or SLIT and investigate the effects on the stability region. Furthermore, other novel geometries could serve as interesting subjects. All stability region experiments were performed on a m/z 121 ion, but pseudopotential well depth varies with mass-to-charge ratio. Using different ion masses, therefore, may affect the perceived mass window and ion accumulation efficiencies. Using doubly charged species may also affect this behavior. No comprehensive studies have been completed exploring comparisons of helium and air buffer gas at the same conditions.

Resonant behavior, especially double resonance, was shown to be greatly damped with pressure. It was demonstrated that increasing the supplemental AC voltage at higher pressures can still effect resonant ejection, which is a valuable strategy for HPMS to extend mass range and achieve good resolution. It also has shown promise for interacting with trapped ions via axial

AC towards other purposes, such as tandem mass spectrometry. The double resonance points of SLITS have not yet been investigated at low pressures.

The results described in this section have been important steps towards building an understanding of HPMS. While no new functionality was demonstrated, these experiments served to elucidate the role of pressure on the behaviors of trapped ions, informing future strategies.

2.5 Figures

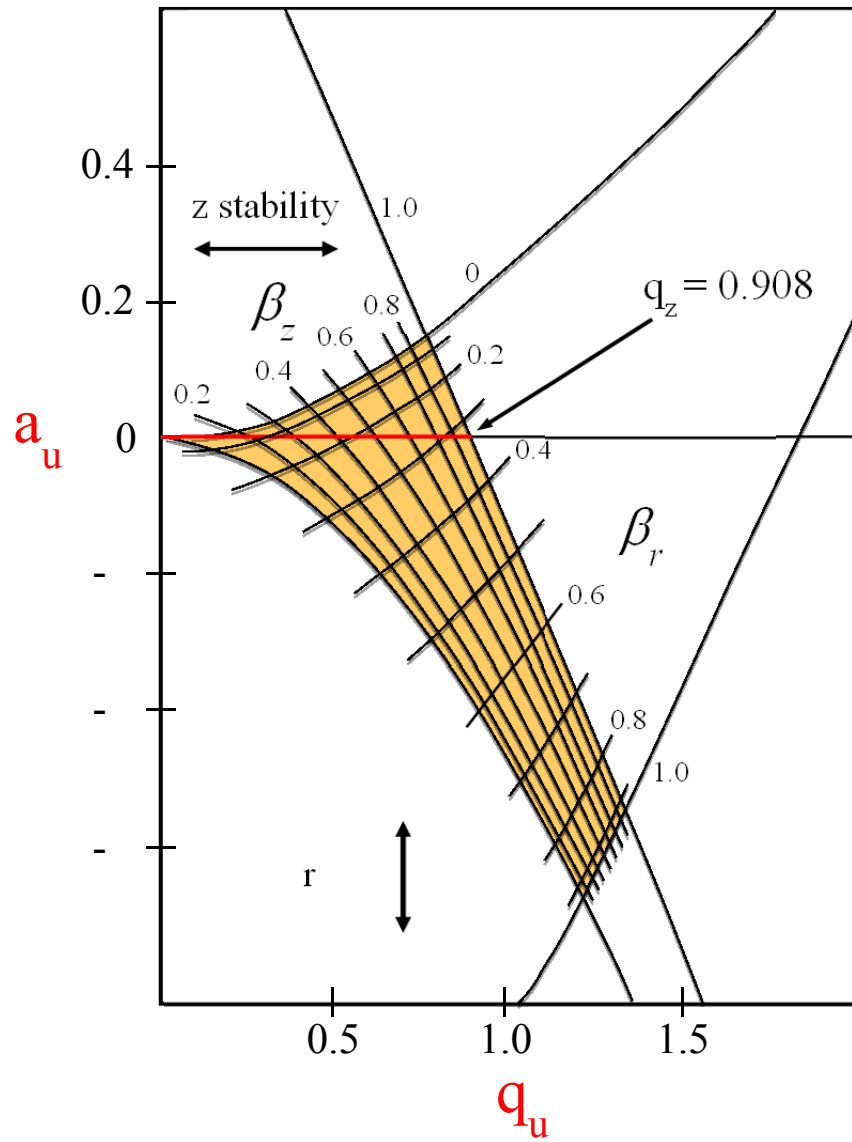


Figure 2.1: Detailed plot of the stability area typically used for ion trap mass spectrometry.

The yellow portion represents the set of conditions for which an ion is stably trapped.

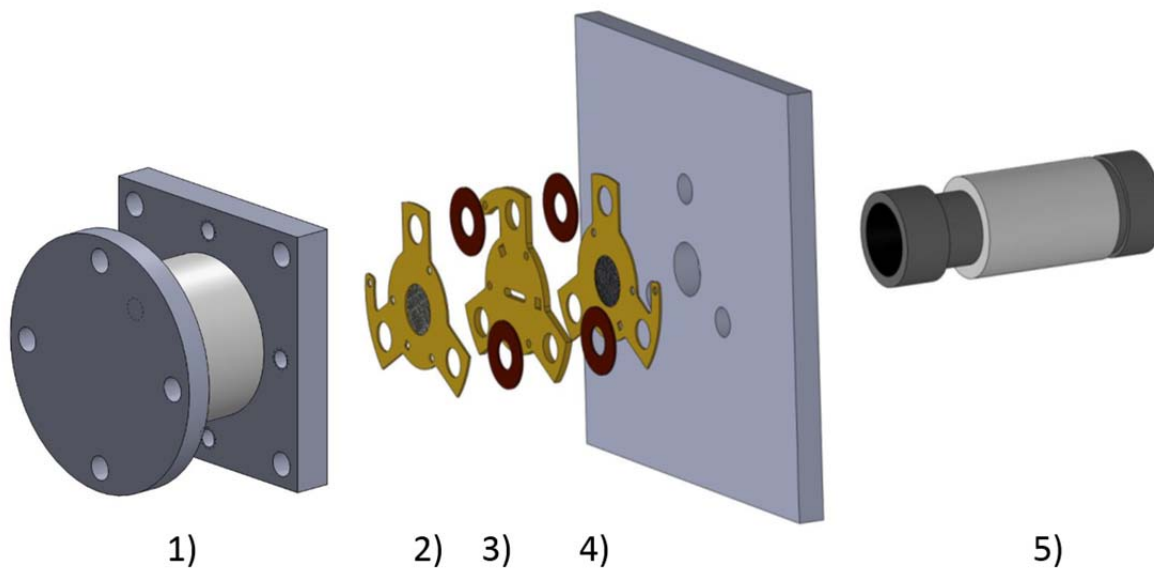


Figure 2.2: Exploded cartoon view of the components in a differential pressure mass spectrometer. 1) Glow discharge ionization source. 2) Ion trap end cap. 3) Ion trap ring electrode. 4) Ion trap endcap. 5) Electron multiplier for detection, held at low pressure.

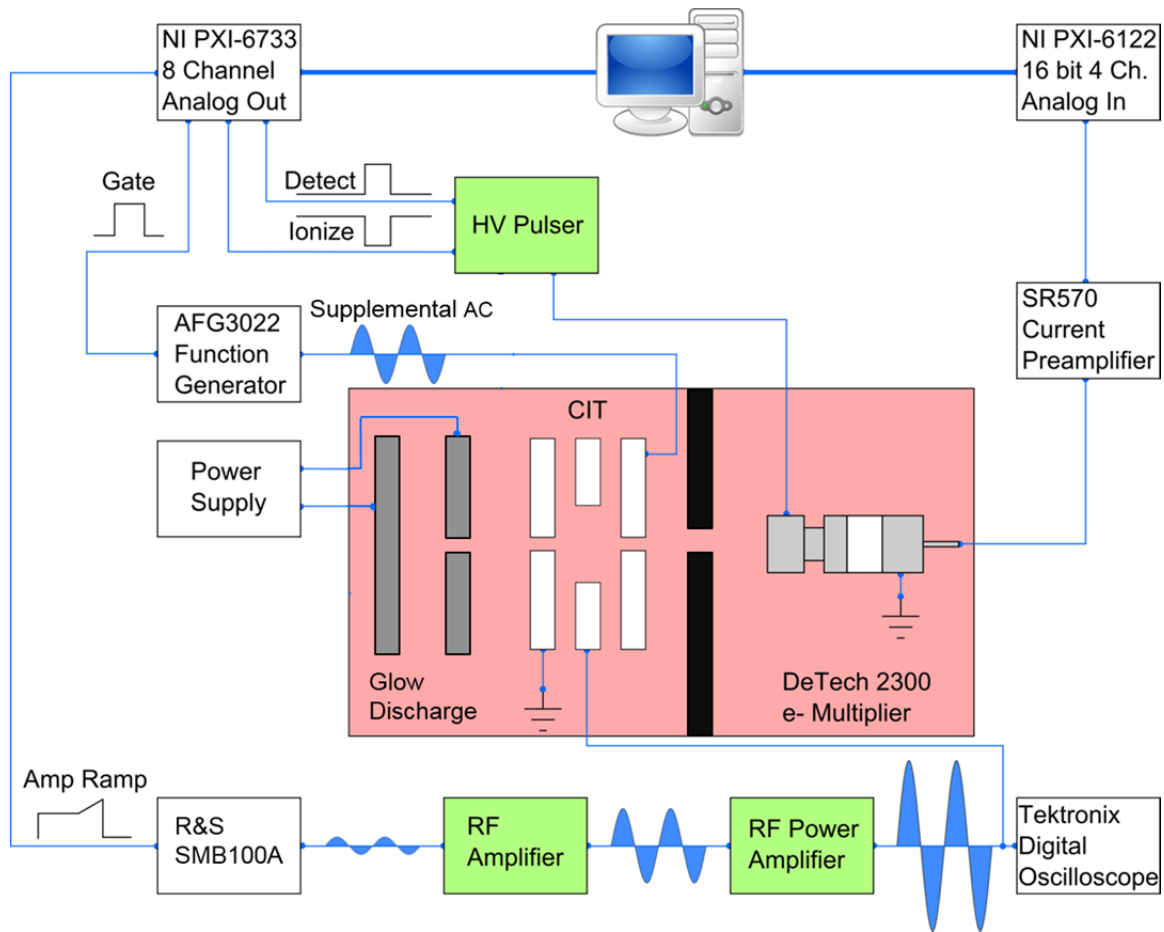


Figure 2.3: Control diagram representing the necessary components of the entire mass spectrometer. The pink box designates the components inside the vacuum chamber.³³

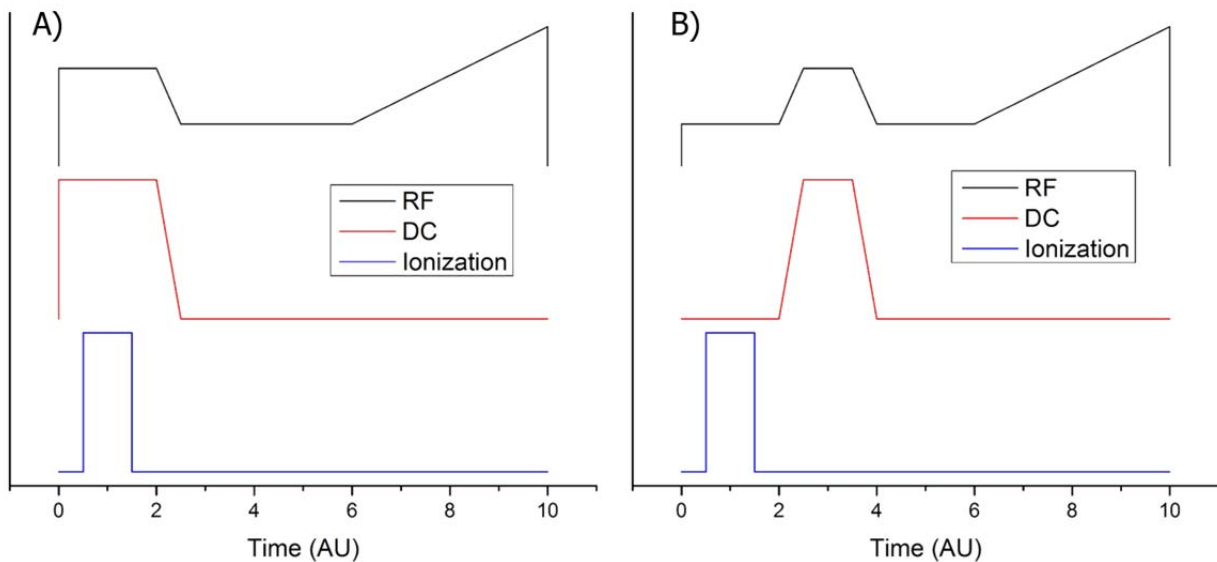


Figure 2.4: Timing diagram for the experimental methods of mapping stability regions. In Panel A, ions are accumulated at varied values of a and q between time = 0.5 and 1.5 and then ejected by ramping the RF voltage. In Panel B, ions are accumulated at a standardized value of a and q (Time = 0.5 to 1.5) before being moved to the experimental conditions (between time = 2.5-3.5) followed by ejection (Time > 6).

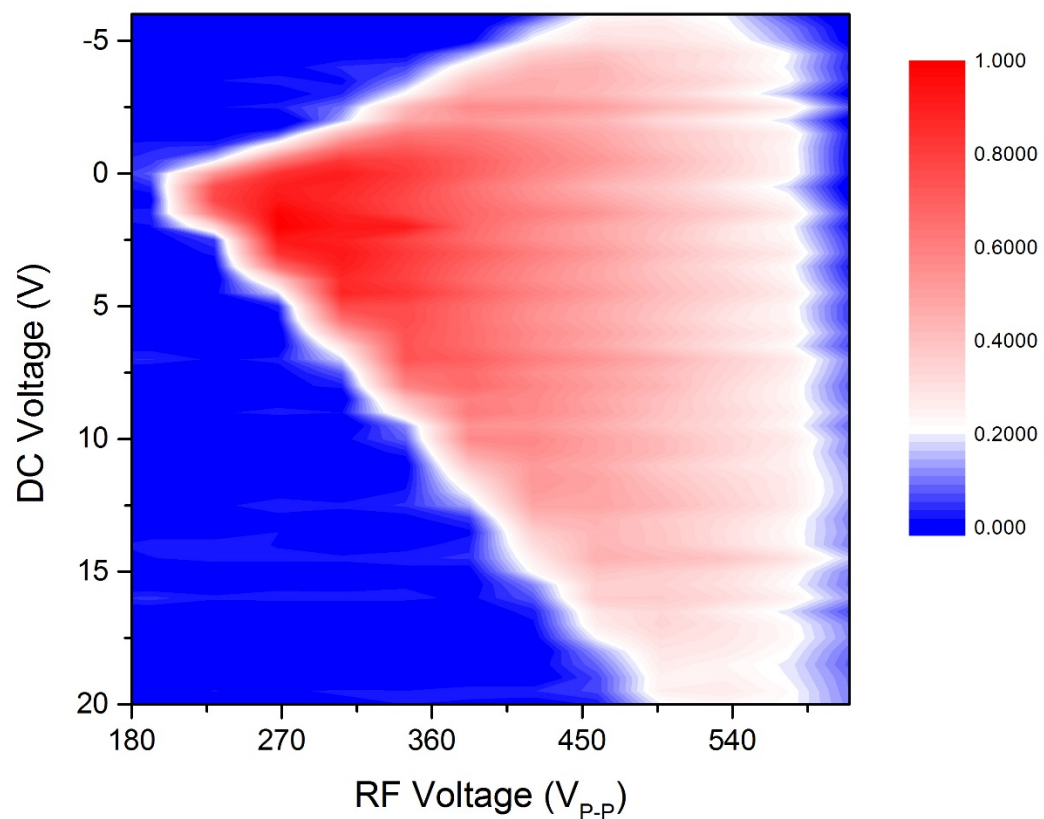


Figure 2.5: Stability diagram for a CIT with $r_0 = 500 \mu\text{m}$ with 1 Torr air buffer gas, generated from molecular ion of N,N-dimethylaniline (m/z 121). This experiment used the timing diagram shown in Figure 2.4.A.

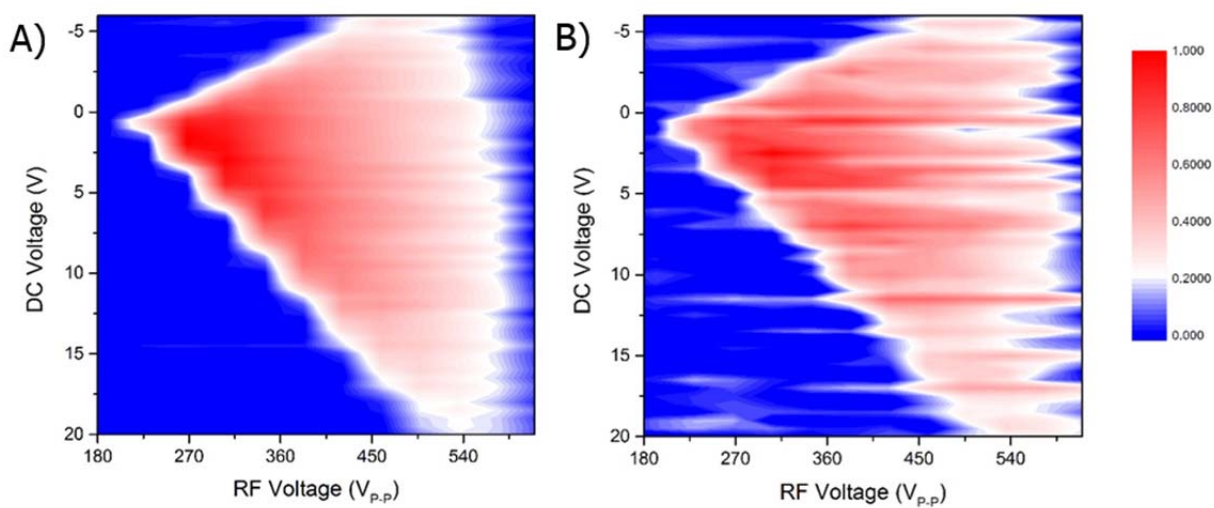


Figure 2.6: Stability diagrams for a CIT with $r_0 = 500 \mu\text{m}$, at A) 500 and B) 1500 mTorr air buffer gas, generated from molecular ion of N,N-dimethylaniline (m/z 121). This experiment used the timing diagram shown in Figure 2.4.A.

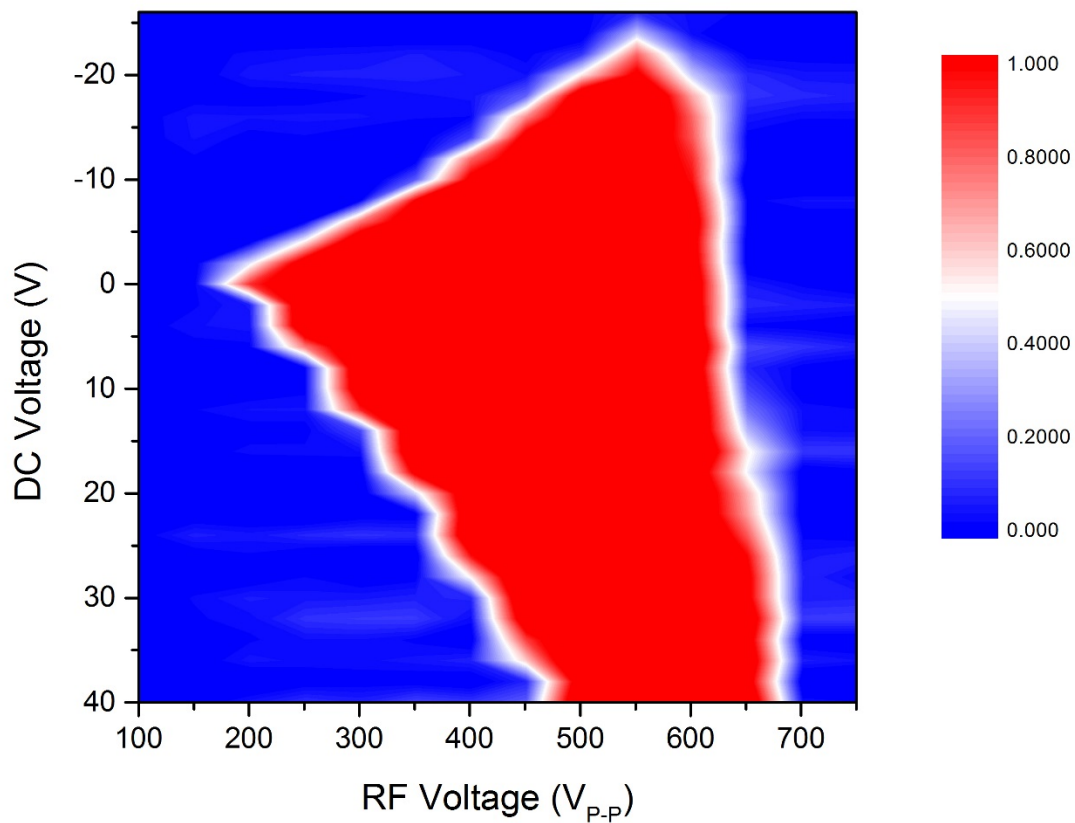


Figure 2.7: Stability diagram for a CIT with $r_0 = 500 \mu\text{m}$, at 1 Torr air buffer gas, generated from molecular ion of N,N-dimethylaniline (m/z 121). This experiment used the timing diagram shown in Figure 2.4.B.

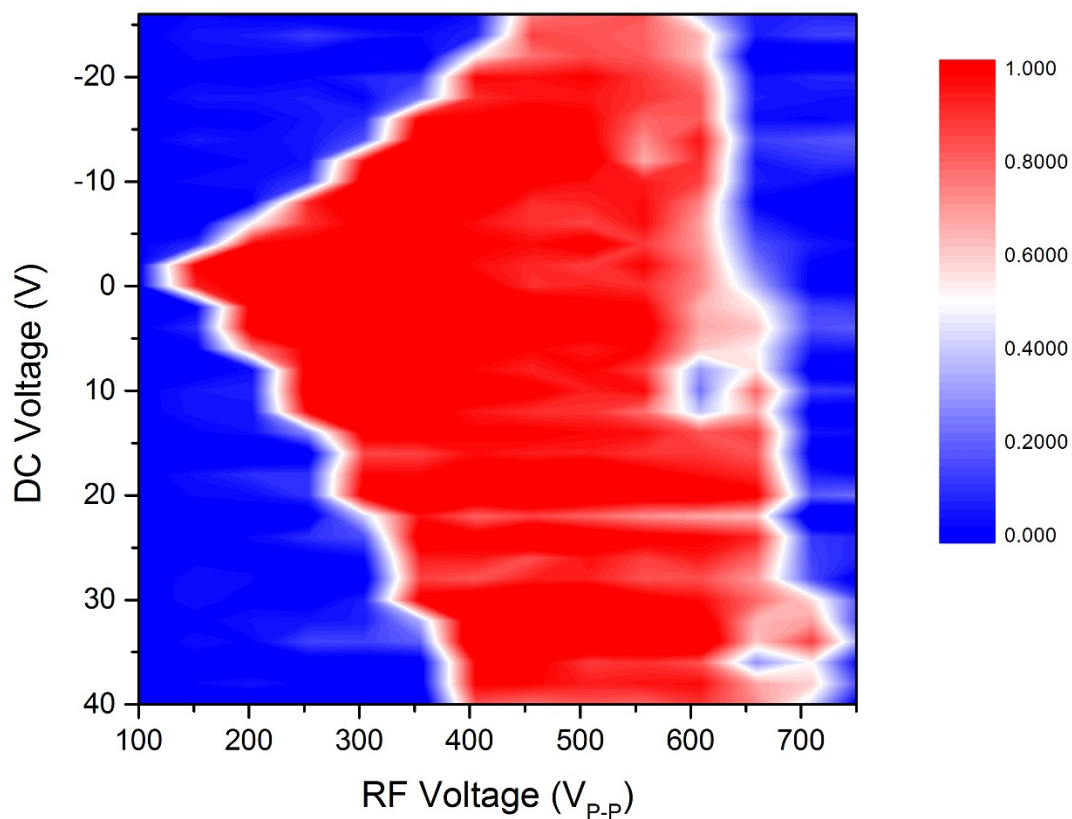


Figure 2.8: Stability diagrams for a CIT with $r_0 = 500 \mu\text{m}$, at 10 mTorr helium buffer gas, generated from molecular ion of N,N-dimethylaniline (m/z 121). This experiment used the timing diagram shown in Figure 2.4.B.

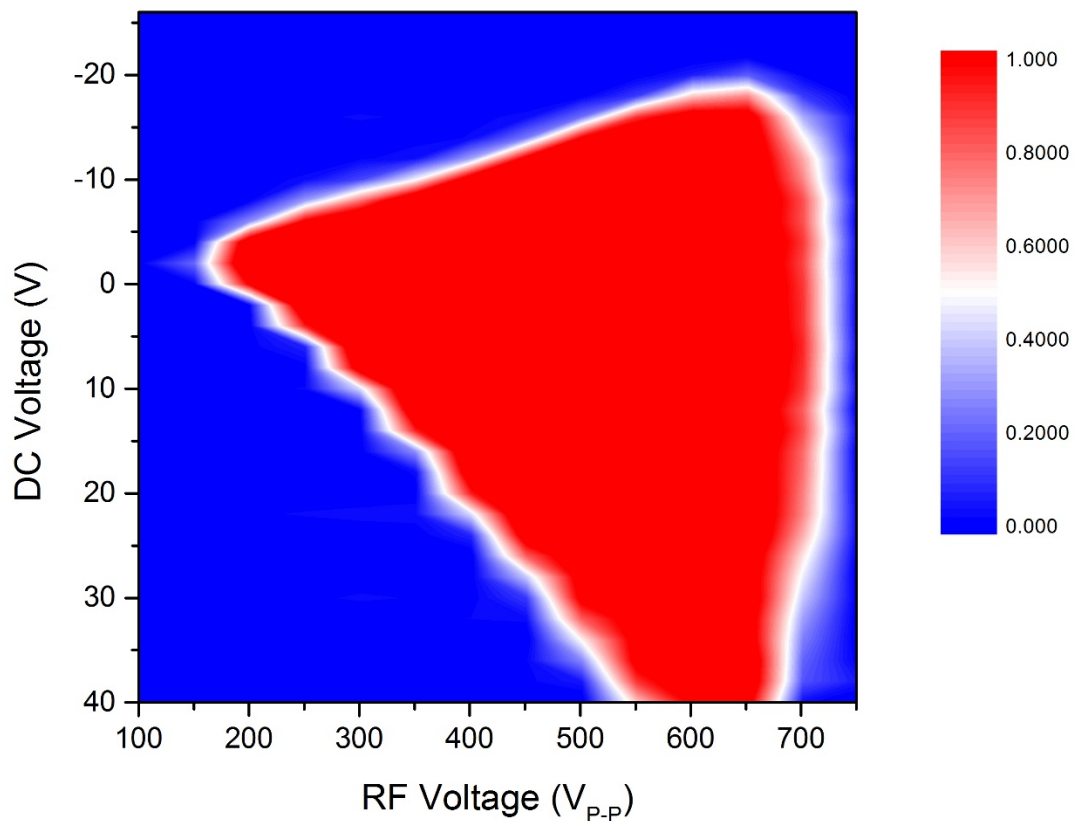


Figure 2.9: Stability diagrams for a SLIT with $x_0 = 500 \mu\text{m}$, at 1 Torr air buffer gas, generated from molecular ion of N,N-dimethylaniline (m/z 121). This experiment used the timing diagram shown in Figure 2.4.B.

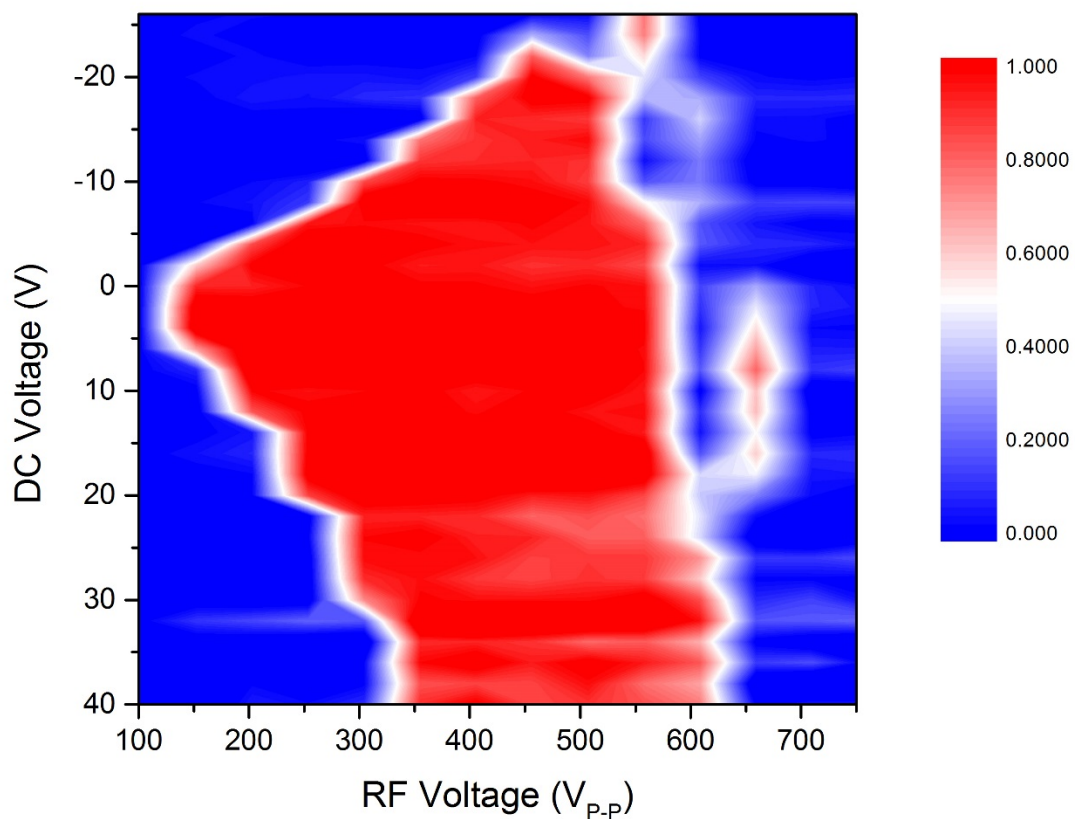


Figure 2.10: Stability diagrams for a SLIT with $x_0 = 500 \mu\text{m}$, at 10 mTorr helium buffer gas, generated from molecular ion of N,N-dimethylaniline (m/z 121). This experiment used the timing diagram shown in Figure 2.4.B.

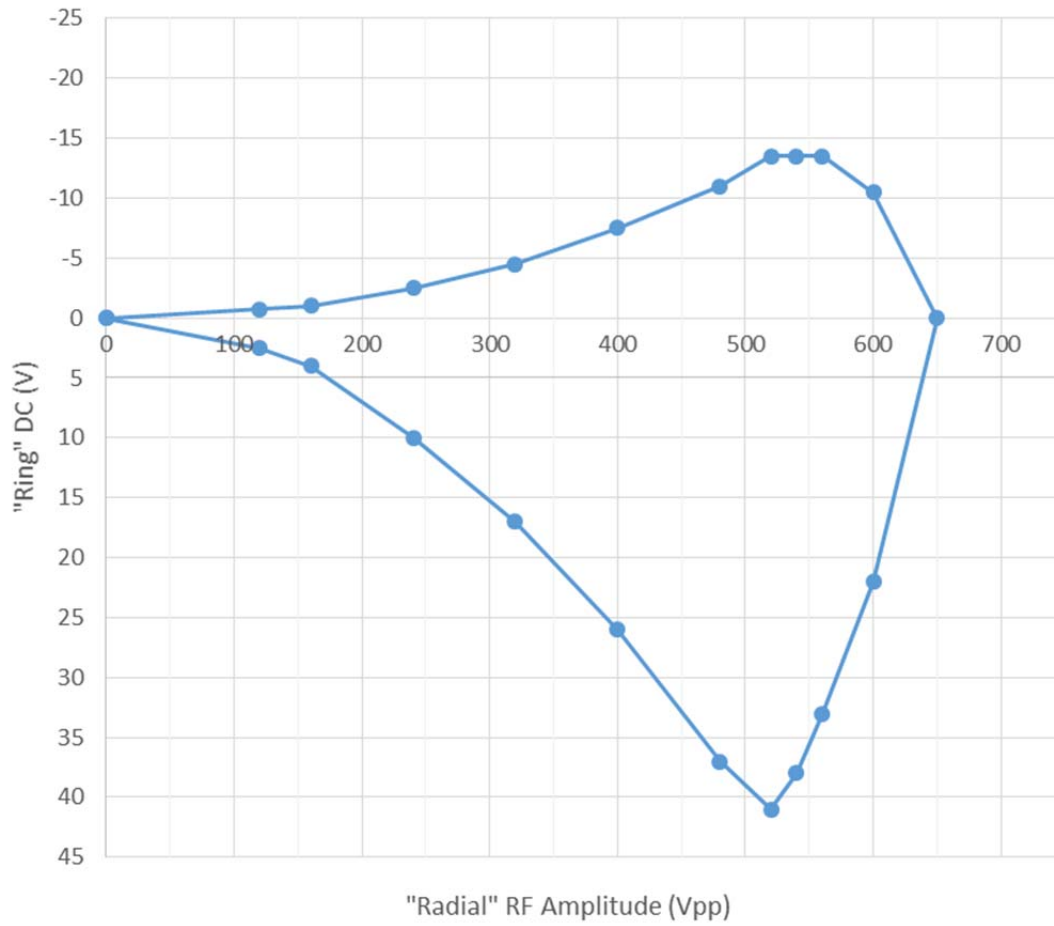


Figure 2.11: A stability diagram for a SLIT, generated via simulation in SIMION. The boundaries show clear asymmetry, but also do not have the expected shape for a three-dimensional trap along the right-hand border.

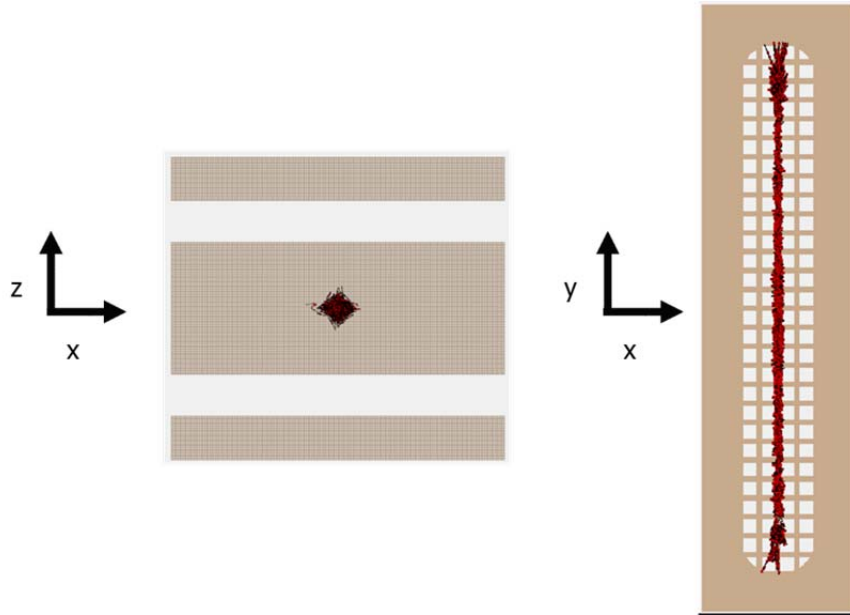


Figure 2.12: Trajectories of ions from SIMION simulation²⁸ along the z-x and y-x planes of a SLIT with -8 V DC, 400 V_{p-p} RF. Although ions are stable along the z-axis, they are unstable along the y-axis due to the negative potential from the DC bias.

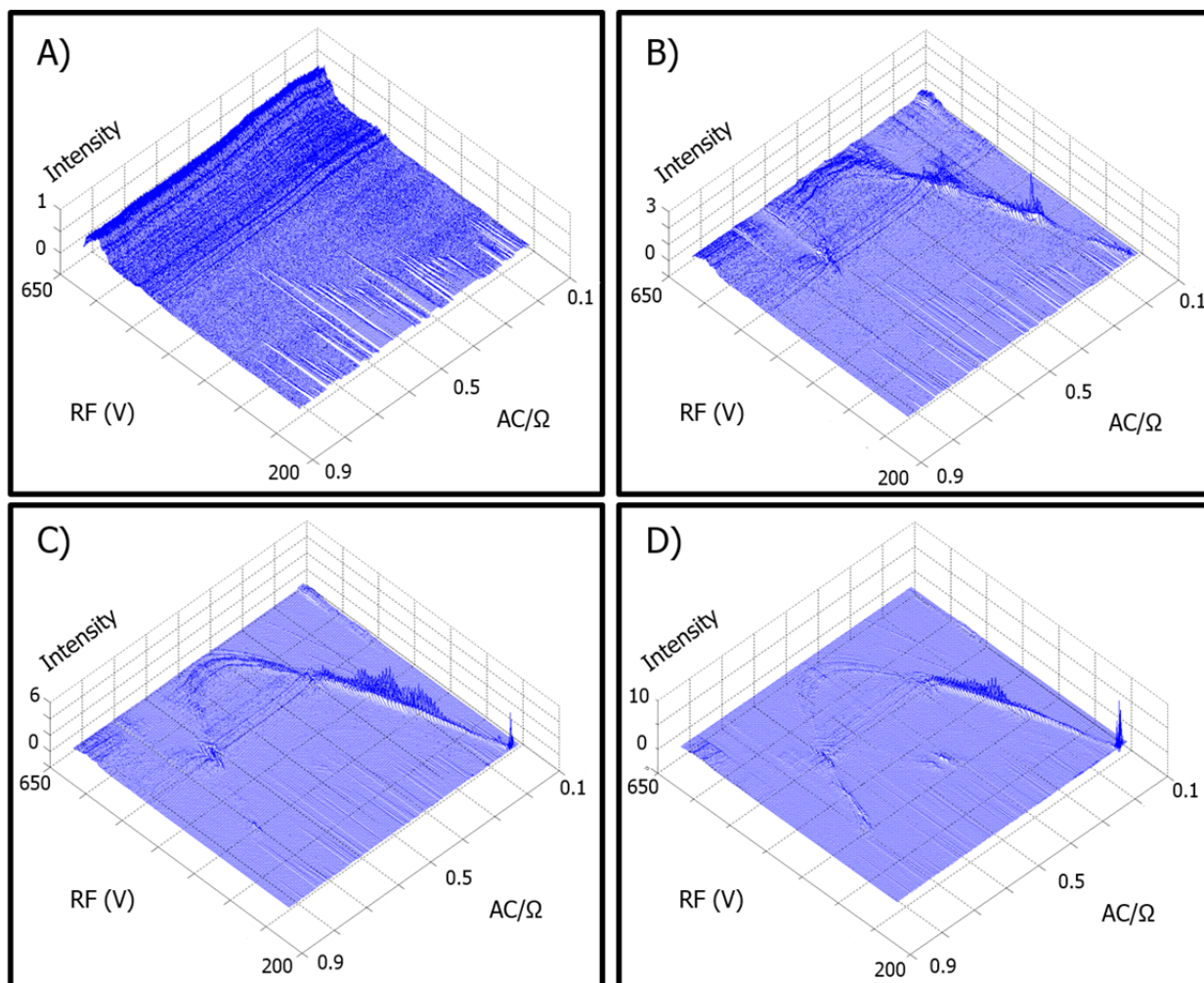


Figure 2.13: Stacked spectra showing the interaction of supplemental AC with trapped atomic ions of xenon at 1 mTorr helium buffer gas. Each blue line (running lower right to upper left) is a mass spectrum. Moving right to left along the lower right axis (AC/Ω), supplemental AC frequency increases as a fraction of drive RF frequency. Drive RF voltage (RF (V)) is ramped as in a traditional mass scan and plotted from right to left as the lower left axis. The voltage of supplement AC is set for each panel: A) $0.010 V_{0-P}$ B) $0.50 V_{0-P}$ C) $1.0 V_{0-P}$ D) $2.0 V_{0-P}$.

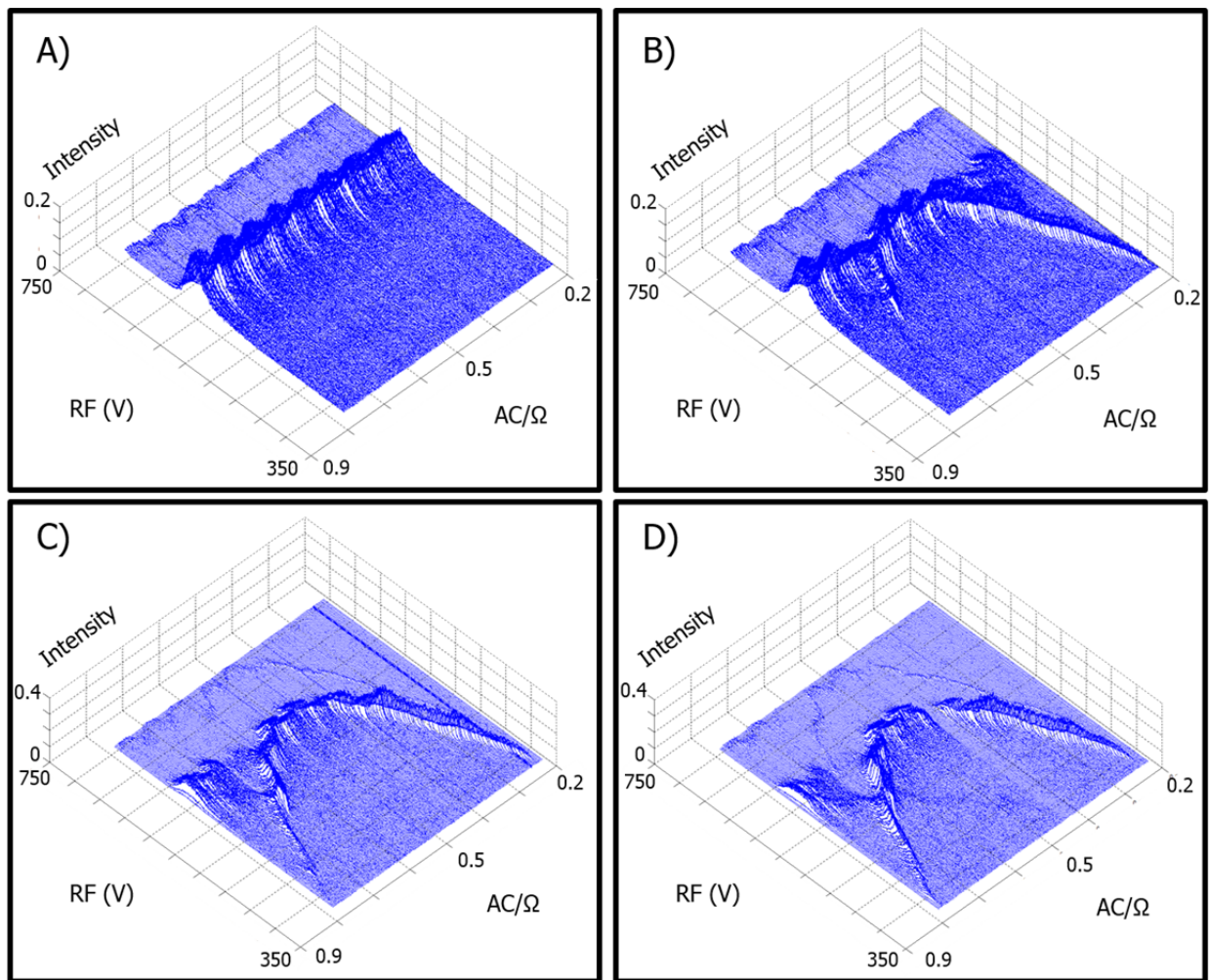


Figure 2.14: Stacked spectra showing the interaction of supplemental AC with trapped atomic ions of Xenon at 300 mTorr helium buffer gas. AC voltage was held at A) 0.010 V_{0-P} B) 1.0 V_{0-P} C) 2.0 V_{0-P} D) 3.0 V_{0-P} .

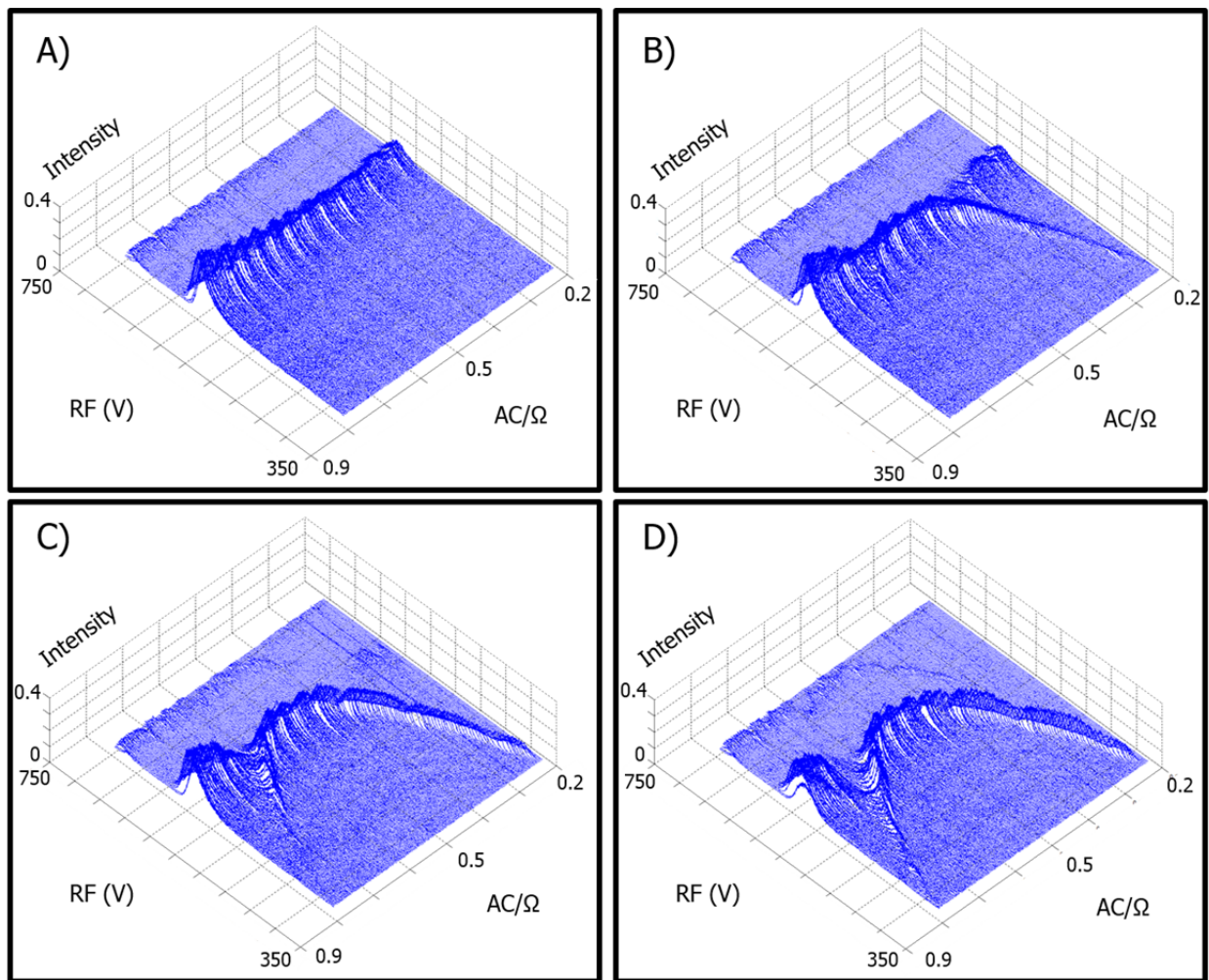


Figure 2.15: Stacked spectra showing the interaction of supplemental AC with trapped atomic ions of Xenon at 1.0 Torr helium buffer gas. AC voltage was held at A) 0.010 V_{0-P} B) 1.0 V_{0-P} C) 2.0 V_{0-P} D) 4.0 V_{0-P}.

2.6 REFERENCES

1. March, R.E., *Quadrupole ion traps*. Mass Spectrom. Rev., 2009. **28**(6): p. 961-989.
2. Murty, S.V.S.N., *Advances in metallic materials and manufacturing processes for strategic sectors : selected, peer reviewed papers from the International Conference on Advances in Metallic Materials and Manufacturing Processes for Strategic Sectors (ICAMPS 2012), January 19-21, 2012, Trivandrum, India*. Materials science forum., 2012, Durnten-Zurich, Switzerland: Trans Tech Publications. xxi, 808 p.
3. Stafford, G., *Ion trap mass spectrometry: a personal perspective*. Journal of the American Society for Mass spectrometry, 2002. **13**(6): p. 589-596.
4. March, R.E., *An Introduction to Quadrupole Ion Trap Mass Spectrometry*. J. Mass Spectrom., 1997. **32**(4): p. 351-369.
5. Leuthner, H. and G. Werth, *Buffer-gas-cooled ion clouds in a classical Paul trap: superimposed stability diagrams and trapping capacity investigations*. Applied Physics B, 2014. **114**(1-2): p. 89-98.
6. March, R.E. and J.F.J. Todd, *Practical Aspects of Trapped Ion Mass Spectrometry, Volume IV: Theory and Instrumentation*. 2010: CRC Press.
7. Xu, W., et al., *Ion trap mass analysis at high pressure: a theoretical view*. J. Am. Soc. Mass Spectrom., 2009. **20**(11): p. 2144-53.
8. Song, Q., et al., *Ion trap mass analysis at high pressure: an experimental characterization*. J. Mass Spectrom., 2010. **45**(1): p. 26-34.
9. Whitten, W.B., P.T. Reilly, and J.M. Ramsey, *High-pressure ion trap mass spectrometry*. Rapid Commun. Mass Spectrom., 2004. **18**(15): p. 1749-52.
10. Hager, J.W., *A new linear ion trap mass spectrometer*. Rapid Communications in Mass Spectrometry, 2002. **16**(6): p. 512-526.
11. Albrieux, F., et al., *Ion trajectory simulations in a high-pressure cylindrical ion trap*. European Journal of Mass Spectrometry, 2010. **16**(5): p. 557.
12. Badman, E.R. and R. Graham Cooks, *Miniature mass analyzers*. Journal of Mass Spectrometry, 2000. **35**(6): p. 659-671.

13. Taylor, N. and D.E. Austin, *A simplified toroidal ion trap mass analyzer*. Int. J. Mass Spectrom., 2012. **321**: p. 25-32.
14. Bandelow, S., G. Marx, and L. Schweikhard, *The stability diagram of the digital ion trap*. International Journal of Mass Spectrometry, 2013. **336**: p. 47-52.
15. Possa, G.C. and L.F. Roncaratti, *Stability Diagrams for Paul Ion Traps Driven by Two-Frequencies*. The Journal of Physical Chemistry A.
16. Louris, J.N., et al., *Instrumentation, applications, and energy deposition in quadrupole ion-trap tandem mass spectrometry*. Analytical Chemistry, 1987. **59**(13): p. 1677-1685.
17. Dawson, P.H. and N.R. Whetten, *Non-linear resonances in quadrupole mass spectrometers due to imperfect fields I. The quadrupole ion trap*. International Journal of Mass Spectrometry and Ion Physics, 1969. **2**(1): p. 45-59.
18. Drakoudis, A., M. Söllner, and G. Werth, *Instabilities of ion motion in a linear Paul trap*. International Journal of Mass Spectrometry, 2006. **252**(1): p. 61-68.
19. Gulyuz, K. and N.C. Polfer, *Ion Traps*, in *Laser Photodissociation and Spectroscopy of Mass-separated Biomolecular Ions*, N.C. Polfer and P. Dugourd, Editors. 2013, Springer International Publishing: Cham. p. 49-70.
20. Bier, M.E. and J.E.P. Syka, *Ion trap mass spectrometer system and method*. 1995, Google Patents.
21. Ramsey, J.M. and K. Schultze, *Miniature charged particle trap with elongated trapping region for mass spectrometry*. 2014, Google Patents.
22. Johnson, J.V., et al., *The stretched quadrupole ion trap: Implications for the Mathieu au and qu parameters and experimental mapping of the stability diagram*. Rapid Communications in Mass Spectrometry, 1992. **6**(12): p. 760-764.
23. Ouyang, Z., et al., *Rectilinear Ion Trap: Concepts, Calculations, and Analytical Performance of a New Mass Analyzer*. Analytical Chemistry, 2004. **76**(16): p. 4595-4605.
24. Blakeman, K.H., et al., *High pressure mass spectrometry of volatile organic compounds with ambient air buffer gas*. Rapid Communications in Mass Spectrometry, 2017. **31**(1): p. 27-32.
25. Blakeman, K.H., et al., *High Pressure Mass Spectrometry: The Generation of Mass Spectra at Operating Pressures Exceeding 1 Torr in a Microscale Cylindrical Ion Trap*. Analytical Chemistry, 2016. **88**(10): p. 5378-5384.

26. March, R.E. and J.F. Todd, *Quadrupole Ion Trap Mass Spectrometry*. 2005: Wiley.
27. Schultze, K., *Advanced System Components for the Development of a Handheld Ion Trap Mass Spectrometer*. Dissertation, University of North Carolina at Chapel Hill, 2014.
28. Goodwin, M., *Stability Diagrams of SLITs*. Unpublished Results, 2015.
29. Kaiser, R.E., et al., *Operation of a quadrupole ion trap mass spectrometer to achieve high mass/charge ratios*. International Journal of Mass Spectrometry and Ion Processes, 1991. **106**: p. 79-115.
30. Tabert, A.M., M.P. Goodwin, and R.G. Cooks, *Co-occurrence of Boundary and Resonance Ejection in a Multiplexed Rectilinear Ion Trap Mass Spectrometer*. Journal of the American Society for Mass Spectrometry, 2006. **17**(1): p. 56-59.
31. Snyder, D.T., C.J. Pulliam, and R.G. Cooks, *Linear mass scans in quadrupole ion traps using the inverse Mathieu q scan*. Rapid Communications in Mass Spectrometry, 2016. **30**(22): p. 2369-2378.
32. Moxom, J., et al., *Double resonance ejection in a micro ion trap mass spectrometer*. Rapid Commun. Mass Spectrom., 2002. **16**(8): p. 755-760.
33. Wolfe, D., *High-Pressure Cylindrical Ion Trap Mass Spectrometry*. UNC at Chapel Hill, North Carolina, 2012.

Chapter 3: Ion Manipulation in High Pressure Ion Traps

3.1 Introduction

High pressure mass spectrometry (HPMS) has recently been shown as a viable strategy to push the frontiers of miniaturized mass spectrometry.¹ A drawback to the technique, however, is a degradation of mass spectral resolution, and thus selectivity, due to collisional broadening. Because of this tradeoff, more species are likely to appear isobaric, meaning they are observed to have the same mass-to-charge ratio. One strategy to combat this trend is to increase the drive frequency of the trap. This tactic, however, requires reduction of trap size, thus decreasing sensitivity, in order to avoid large increases in power consumption. To overcome the loss in sensitivity, the stretched length ion trap (SLIT), with a higher ion capacity, was developed.^{2,3} It is also possible to further improve both sensitivity and selectivity by exploiting the advantages from ion trapping. Tandem mass spectrometry, for example, is an important technique due in large part to its capability to differentiate isobars and improve selectivity.^{4,5}

Ion traps have significant capabilities beyond other mass analyzers due to their ability to store ions for prolonged periods of time.^{6,7} Once the ions are trapped, it is possible to manipulate them by controlling the electric field within the trap. Frequently these interactions facilitate means of probing ion characteristics other than mass-to-charge ratio. For example, ion traps are popular tools in ion spectroscopy,^{8,9} and were used for such experiments even before the invention of the quadrupole ion trap mass spectrometer.^{10,11} For our purposes, we take advantage of three major forms of trapped ion manipulation: spatial control of ions in the y-axis of SLITs;

mass-selective ion isolation where unwanted ions are ejected, leaving the ion of interest in the trap; and resonant excitation for collision-induced dissociation (CID), where the fragmentation pattern can be used to improve chemical identification.

SLITs, like all linear ion traps (LITs), spatially confine ions into a linear ion cloud, along the length of which ions can move freely. Figure 3.1 shows a depiction of the ring electrodes for these trapping geometries, where trapped ions are free to move along the z-axis of a LIT or y-axis of a SLIT. Because of their larger volumes compared to cylindrical or hyperbolic ion traps respectively, there are significant improvements in sensitivity from these trapping strategies.^{12, 13} To fully take advantage of this increase in sensitivity, ensuring that ion ejection occurs from a single point would prevent inconsistent conditions at detection, thereby improving resolution. Current HPMS design has the detector in line of sight of the ionization source. It would be preferable to inject and eject ions from distinctly different portions of the SLIT to avoid overloading the Faraday cup detector with excess charge during ion accumulation. To control the location of ion ejection, slight modifications to the geometries of SLITs affecting the potentials within the trap were investigated.

To effectively implement tandem mass spectrometry in an ion trap, there are two fundamental steps needed: mass-selective ion isolation and resonant excitation for CID. In the first step, a targeted precursor ion population is isolated from other accumulated ions, ensuring that peaks in the subsequent mass spectrum are directly related to the precursor, rather than a potential interferent. Second, the selected ions must be activated, causing fragmentation. In ion traps, this activation is almost always collision-induced dissociation (CID) via resonant excitation. These new fragments can be mass analyzed, revealing important chemical information about the initial ion population, differentiating the analyte from other species with

the same mass-to-charge ratio. Note it is possible to go beyond the two stages of tandem MS with the limiting factor on stages simply being the efficiency of each stage of isolation and fragmentation.¹⁴

Experiments in this chapter focused on improving chemical identification through manipulations of trapped ions at high pressures to enhance sensitivity and selectivity. Spatial ion control in a tapered SLIT and a SLIT with supplementary electrodes are investigated. The steps necessary to perform tandem mass spectrometry are also investigated. Precursor ion isolation is demonstrated at high pressures via apex isolation, SWIFT-like multi-frequency excitation, and abbreviated instability scans. Collision-induced dissociation (CID) via resonant excitation is demonstrated in high pressure ion traps with 1 Torr air buffer gas.

3.2: Spatial Control of Ion Ejection from SLITs

The spatial profile of ions upon ejection from SLITs has been previously investigated.² It was found that ions rapidly sampled the entire length of the trap, though they would become axially unstable and eject at local “hot spots” created by geometrical variations. The location of these “hot spots” was difficult to predict from simple observation of the electrodes. As pressures increased to HPMS conditions, however, the effects of these “hot spots” were minimized, likely due to collisions inhibiting the resonant amplification of ions due to the higher order fields hypothesized to be present at these points. Because of this smoothing effect, under the conditions desired for a portable device at 1 Torr of air buffer gas, the ejection profile was generally uniform along the length of the SLIT.

Other researchers have also investigated strategies to effectively control the location of ion ejection from two-dimensional traps. Extensive research has been conducted into mass selective methods for axial ejection from linear ion traps.^{12, 15} Axial ejection has offered advantages in resolution over conventional radial ejection and is extremely useful for hybrid instruments, where the ions can easily be ejected as a tight beam into a subsequent mass analyzer. The predominant strategy employed in commercial traps is to excite ions radially and use fringing fields near the endcaps to couple that motion into the axial dimension. Another strategy is to add a potential gradient along the length of the trap by adding slanted wire electrodes between the electrode rods.^{16, 17} Because the electrodes are different distances from the center of the trap, there is a roughly linear electric field imposed along the length of the ion trap, keeping the ions moving towards the exit end cap.¹⁸

If internal ion manipulation is successful, there is a possible added advantage of injecting ions in one location of the trap and ejecting the ions at a different location of the trap. The desire to implement this capability stems from an overabundance of charge during ion accumulation. Much of this charge will escape the trap and, depending on the trap to detection geometry, impact the detector. This is especially detrimental for a Faraday cup detector, where the response time and sensitivity are a function of the amplification circuitry. Designing the circuitry to maximize bandwidth and sensitivity, however, requires tradeoffs with the robustness to handle this abundance of charge. The most likely impact is that the detector generates a maximum output unrelated to the mass spectrum and will require some time, on the order of a few milliseconds, to return to a baseline response. This requires added time to the scan function and may affect sensitivity and the ability to perform enough scans to average. Having spatial control of ions along the length of a SLIT would allow the detector to be offset from the ionization

region, preventing the excess charge during ionization from impacting the detector. This would simplify the design of the appropriate detection circuit.

3.2.1: Tapered SLIT Geometry

Research has previously explored the impact of introducing a taper along the lengthwise y-axis of a SLIT.² It was found that at low pressures, ions did preferentially eject from the smaller end of the trap, where their experienced q_z value would be increased due to the smaller dimensions. Thus, ions that were rapidly sampling the full length of the trap would first become unstable in the smaller portion of the trap and eject. These experiments, however, used traditional operating conditions with no DC potential on the ring electrode. Applying a DC potential to a tapered ring electrode creates an electric potential gradient (Figure 3.2) along the length of the SLIT. Rather than relying on ions to randomly sample the full length of the trap, this field drives ions to a specific location. A positive potential on the ring should drive the trapped ions (typically positive in charge) to the wider end of the trap, where they can be furthest away from the walls of the ring electrode. A negative potential, in contrast, should pull the ions towards the narrow end. Stability diagrams indicate, however, that there is a limit to the negative potential (on the order of several volts) that can be applied as it will likely pull the ions into neutralizing on the electrodes.

There is a potential drawback to the tapered geometry, though. The tapered geometry is, in many ways, equivalent to non-parallel rods used in a linear ion trap.¹³ The skewing of the trap, rather than simply leading to selective ejection from one space, can lead to ejection at different voltages at different locations along the length of the trap. When scanning voltages, this causes

multiple masses being ejected at the same time, which corresponds to a loss in mass spectral resolution.

To determine the effect of various DC potentials applied to the ring electrode on the SLIT ejection location, three experiments (Figure 3.3) were run where the ion intensity was measured from the entire SLIT, from the right-hand side or “broad” side of the SLIT, and from the left-hand or “narrow” portion of the SLIT. This was accomplished by placing conductive copper tape, in electrical contact with the endcap, over the respective areas where signal was undesired such that all signal would be from the opposite half of the trap. In this case, the SLIT had a 10% taper of the x-dimension along the y-axis. The combination of geometry and applied voltage creates a potential gradient as seen in Figure 3.2. With a positive potential applied, a valley is created on the broad side of the trap (the deepest region of which is shaded), causing ions to pool there. A negative potential creates an opposite field, causing ion migration toward the narrow side. For these experiments, the DC values were held constant throughout the scan function.

For comparison purposes, each trace was normalized to the signal with 0 volts applied, where no electric field controlled ion location. The black trace shows the signal from the whole tapered SLIT. As the whole trap is being sampled, signals higher than 1 would indicate improved trapping while signals below 1 indicate the opposite. The maximum signal is seen with 2 V DC on the ring electrode. This is consistent with the experimental stability diagrams for straight-edged SLITs generated in Chapter 2. Also as expected, overall signal decreases with increasing negative voltages.

The blue trace corresponds to the mass spectral intensity from the broad side of the SLIT when a blocking electrode was placed between the detector and the narrow half of the SLIT. If no effect on ejection location is present, the relative signal would be expected to mimic the

signal acquired from the entire trap (black trace). As predicted, the relative signal intensity increases with the maximum at approximately 2 V DC potential. Part of this increase is due to the increase in total number of ions trapped as a whole but the relative gain is significantly stronger than that observed from the entire SLIT. This indicates that the trapped ions have shifted their ejection location more towards the broad side of the trap rather than the narrow side. The red trace was generated with a blocking electrode between the wide half of the SLIT and the detector, thus representing the intensity of ions ejecting from the narrow side. The expected signal intensity increase with a positive potential is again seen due to improved trapping, though it occurs at 1 V compared to 2 V DC as in the entire trap and broad side signals. Based on the broad side ejection results, this is expected since the majority of ions should be on the broad side when positive DC potentials are applied. Compared to the entire trap signal, the relative gains in intensity are weaker over the range of positive voltages, indicating a lower proportion of the ions ejecting from the narrow side. While the signal decreases slightly with a few negative volts DC, the relative signal is higher than the broad side signal, indicating a higher proportion of ions on the narrow side. These trends show agreement with the expected outcomes for ions moving towards the narrow end of a tapered SLIT with negative DC and towards the broader end with positive DC.

Figure 3.4 shows the signal from the broad and narrow sides plotted as the ratio of the intensity of ions ejected from the broad side to the intensity of ions ejected from the narrow side of the SLIT. Even at 0 V, the broader side of the trap has a factor of $\sim 2.2x$ more ions. That side is larger in volume, storing significantly more ions even with no applied DC voltage. This ratio, however, clearly grows with small positive DC and shrinks with small negative DC. Beyond

about 3 V in either direction, however, the ratios tend to fall off the expected trend, but this is likely due to a drop in the overall signal affecting the results.

The expected loss in resolution from non-parallelism within the trap was present with the tapered SLIT, but the high pressures tended to cause a more significant limitation for the optimum resolution. The degradation of resolution was frequently observed as an alteration of mass spectral peak shape, normally fronting. This fronting behavior was likely the result of a small population of ions ejecting from the narrow portion of the SLIT first while the majority of ions ejected later in the scan from the broad portion of the SLIT. Furthermore, the signal was noticed to be reduced in these experiments compared to the expected signal from a straight-edged SLIT, despite the overall volume of the trap being increased by the introduction of the taper.

From the data presented, it is clear that preferential control over the ions' ejection location is possible. The largest ratio from Figure 3.4 shows that there can be a ~4.5x factor of ions or around 80% of the ions on the broader side of the trap compared to the narrow at 2 V. For negative applied voltages, the ratio of trapped ion is ~0.9 at -3 V meaning that the slight majority of trapped ions are being ejected from the narrow side, despite the smaller volume. As trap miniaturization to reduce voltage requirements while using high frequencies is the direction this project is heading, transporting ions to the smallest portion of the ion trap for mass analysis would be the largest benefit. The results of these experiments, however, show that influencing ions in the direction of smaller dimensions is significantly more difficult than into the larger dimensions. Although not as beneficial as transporting ions to the narrow side of the trap, this is still a useful capability.

3.2.2: Supplementary Electrode SLIT Geometry

Another strategy for controlling ion location is to introduce an electric field gradient along the y-axis of a SLIT. Printed circuit boards (PCBs), as shown in Figure 3.5, were designed to match the footprint of the ring and endcap electrodes of the trap. A slot feature through the middle was slightly (~5 millimeters) larger than the ion trap (SLIT) feature in the paired ring electrode. On these PCBs, copper leads extend from the circular solder point and are exposed at the exact edge of the slot and act as supplementary electrodes. The circular solder point is used to establish electrical connection to these supplementary electrodes, which are exposed to the trapping volume of the ion trap. As part of the PCB construction, the copper leads for the exposed electrodes are covered with a solder mask that acts as an insulator. These PCBs are inserted between the ring and each endcap electrode (with the solder mask facing the endcaps) and act as spacers. Applying a potential to the supplementary electrodes will affect the electric fields the trapped ions experience inside the trap and can be used to control ion location. By electrically connecting the upper and lower supplementary electrodes together, symmetry in the x-z plane is preserved while a gradient is created in the y-axis. A negative potential would be expected to pull positive ions towards that portion of the trap, while a positive potential should repel the positive ions. Experimental conditions where portions of the trap were blocked from the detector, as in the tapered SLIT experiments, were repeated here. For these experiments, however, a benchtop miniature mass spectrometer from 908 Devices, Inc. with Faraday cup detection was used. Operational pressure was ~1 Torr of ambient air buffer gas, and the drive RF frequency was ~ 6 MHz. The DC potential applied to the supplementary electrodes was generated by a standalone power supply and was held constant throughout the scan function.

Figure 3.6 shows the results of the control experiment where the signal intensity is derived from the entire length of the SLIT trap. Each trace shows the mass spectrum of N,N-dimethylaniline with 0 V DC (black trace), -30 V DC (red trace), or 30 V DC (blue trace) applied to the supplementary electrodes. It can be seen that there is a very slight variation in intensity based on voltage applied, with the signal intensity increasing as the voltage decreased. To generate Figure 3.7, a blocking electrode was placed between the detector and the half of the SLIT without any supplementary electrodes, and the same scan conditions repeated. Thus, the only ions hitting the detector should be ejecting from the side of the SLIT with the supplementary electrodes. The color assigned to each trace is the same as in the previous figure, but the signal intensity variation between the traces is significant. With -30 V applied on the supplemental electrodes, the signal is approximately double the intensity with 0 V applied. This result is consistent with ions being evenly dispersed along the y-axis with 0 V applied and only half reaching the detector due to the blocking electrode. With -30 V applied, the vast majority of ions are trapped near the supplementary electrodes so a large signal should be detected. With 30 V applied, the ions should accumulate on the half of the trap blocked from the detector, resulting in very little signal.

As mentioned above, one of the primary goals for the spatial control of ions is to be able to inject and eject ions from completely different regions of the ion trap. To test this capability, a blocking electrode was placed between the detector and the portion of the SLIT with no supplemental electrodes. A second blocking electrode was placed between the ionization source and the portion of the SLIT with supplemental electrodes. Thus, there was no direct line of sight between the ionization source and the detector, meaning any generated ions must be transported to the side of the trap with supplementary electrodes to be successfully detected. Figure 3.8

demonstrates the signal intensities with 0 and -30 V applied to the supplementary electrodes. Note that even with no voltage applied to the supplemental electrodes (black trace), a small peak is seen, so ions must be dispersed along the full width of the SLIT, despite being collected in a region with no direct path to the detector. With -30 V applied to the supplemental electrodes (red trace), there is a significant gain in sensitivity due to the ions pooling at and ejecting from the region of the SLIT away from the detector-side blocking electrode.

This strategy of supplemental electrodes was shown to be immensely successful at spatially manipulating ions along a SLIT. While these mass spectra could not be converted onto a mass axis due to there only being one peak, the full width at half maximum (FWHM) was measured to be near 0.4 ms in each experiment in Figures 3.6-3.8. This configuration shows minimal cost in terms of resolution as well as experimental complexity, while significant enhancements were shown in terms of ability to control the ejection profile. These results also suggest the possibility of implementing multiple planes of electrodes along the y-axis, used to manipulate ions along this dimension during the course of a single scan function. This capability would greatly enhance the flexibility of the experiment, and it could be used to govern the mixing of different species for controlled ion-ion reactions.

3.3: Targeted Ion Isolation

Tandem mass spectrometry is a way to improve chemical identification, typically involving at least two steps. The first step is isolating a specific population of target analyte ions. After the isolation step, any peaks in the subsequent mass spectra are directly related to the analyte, rather than a potential interferent. Since the primary goal of tandem mass spectrometry is to reveal chemical information about the targeted analyte ion, it is important to confidently

assign a correlation between the peaks, mandating effective ion isolation. Ion isolation effectiveness is measured both by the extent to which unwanted ions are removed and by the efficiency with which the desired ions are preserved.

In ion traps, there are two principal ways that isolation has historically been achieved: apex isolation¹⁹ and stored waveform inverse Fourier transform (SWIFT).²⁰ The former method involves tuning the RF and DC potentials on the ring electrode to trap only a narrow range of m/z . This small mass window is usually reached at the apex of the stability region, as discussed in Chapter 2. For this method to be effective, the stability region must be well characterized such that the appropriate RF and DC potentials can be applied to move a specific mass-to-charge ion into a stable region, while other nearby mass-to-charge ions are rendered unstable and leave the trap. A sharp transition between stable and unstable conditions for ions defines the efficiency of this tactic.

SWIFT, on the other hand, is a means of resonantly exciting ions of all mass-to-charge ratios except a specific m/z window. This specific window of interest is converted to an expected secular frequency and then notched out of a phase-controlled white noise spectrum that is then converted to a time domain signal via inverse Fourier transform. This new signal is applied to the endcaps, causing all ions outside the isolation band to be resonantly ejected. The resonant characteristic of trapped ions is the most important factor in the effectiveness of this strategy. Ions with similar secular frequencies are likely to be excited by the same supplemental AC frequencies, making an isolation difficult.

A third technique is also useful in cases where the target analyte ion population is the highest m/z species in the trap. Ramping the voltage of RF on the ring electrode to just below the ejection voltage of the highest m/z species will eject all ions with lower mass-to-charge ratios.

This technique is far simpler to implement than either apex isolation or SWIFT, but is only applicable when the target analyte is the highest m/z species. The effectiveness of this strategy, within its useful conditions, is governed by the mass resolution of the instability scan. Two ion populations that cannot be resolved by a mass scan will not be isolated by this method.

3.3.1: Apex Isolation

As noted above, apex isolation is a common tactic for ion isolation in an ion trap, relying on strategic use of the stability diagram. Any m/z ratio can be put into the apex of the stability diagram such that larger m/z ions are unstable outside the left boundary of the stability region and smaller m/z ions are unstable outside the right boundary. Figure 3.9 shows apex isolation of aniline ions from N,N-dimethylaniline ions at 1 Torr of air. As can be seen in the figure, the undesired N,N-dimethylaniline (m/z 121) is removed from the spectrum along with a moderate fraction of the targeted aniline (m/z 93). Only 3% by integrated peak intensity of the unwanted m/z 121 peak survives, but just 36% of the desired m/z 93 peak is retained. Just as with a quadrupole mass filter, there is a tradeoff between signal intensity and resolution when using apex isolation. Allowing a more broadband mass window is likely to increase the survival efficiency of the targeted ion, but will also increase the survival efficiencies of unwanted ions. While the ion population was successfully isolated, the results highlighted the poor resolution and low efficiency of this strategy. The ion populations used in this experiment were almost 30 mass-to-charge units apart, but there was still a significant loss in the population of desired ions in order to completely remove the undesired ions. Clearly, an isolation of this quality is insufficient for many situations.

3.3.2: Multifrequency Isolation

Figure 3.10 shows the isolation of aniline from N,N dimethylaniline and fragments, using an alternative approach to apex isolation: multi-frequency isolation, which is a simplified version of SWIFT. Like SWIFT, the underlying principle is to resonantly eject all of the unwanted ions from the trap, while preserving the targeted species. SWIFT is the most common method of isolation in commercial instruments due to its speed, flexibility, and ease of implementation. During initial efforts to isolate ions using a SWIFT function, it was found that a 10-volt (peak to peak) function generator, while outputting a broadband signal, was unable to provide enough power for any given frequency to cause ejection at high pressure. As noted in Chapter 2, ions at higher pressures required higher voltages to be resonantly ejected. The frequency bandwidth of the stored waveform spanned a few megahertz in order to access a mass window of 100 mass-to-charge units. This broad bandwidth caused a significant power dilution across the frequency spectrum such that no particular ion experienced enough resonant excitation to cause ejection.

Because of the high pressure of buffer gas (1 Torr air), the interaction bandwidth of stored ions is larger than in conventional conditions. While this mandates a wider isolation window, this effect also has advantages that can be exploited. For one, it is not necessary to apply a true SWIFT waveform, since a more comb-like function will still eject all unwanted ions. An arbitrary waveform built from the addition of sine waves of several frequencies can be used to eject the undesired ions. This method avoids the moderate computational time required to calculate a SWIFT function that will preserve a certain mass window. The real advantage, however, is that more power can be put into each frequency mode in the arbitrary waveform. A comb function, as others have used at lower pressures,^{21, 22} successfully ejected the undesired ions (m/z 77, 91, 121). The function was calculated by adding sine waves at or near the secular

frequencies of the unwanted ion populations. For the experiment in Figure 3.10, only three sine waves were necessary to achieve isolation. Undesired ions, specifically those at m/z 77, 91, and 121, were ejected, and the targeted ions at m/z 105 isolated with near perfect efficiency. This technique showed a much narrower mass window while maintaining a much higher preservation efficiency as compared to the apex isolation strategy described above.

3.3.3: Partial Instability Scan Isolation

A third isolation method used is where the highest mass-to-charge ion species is isolated by simply performing boundary ejection of all the lower mass-to-charge ions. The isolated species can then be relaxed back to an appropriate q_z value by reducing the RF voltage. In Figure 3.11, the molecular ion of bromobenzene at m/z 156 was isolated from a fragment ion at m/z 77. The isolation efficiency was measured at 100%, as the intensity of the molecular ion is unchanged. As long as two peaks are resolvable in a traditional mass spectrum, it is possible to isolate the higher mass peak with this strategy which is simple to implement. This technique is severely limited by the inability to remove high mass-to-charge contaminants. It is, however, useful in cases of isolating the molecular ion in mass spectra of pure compounds. Going forward with the CID experiments, this was the chosen method as the targeted analyte populations were always the largest mass-to-charge species in the trap.

3.4: Collision-Induced Dissociation in HPMS

The second step of tandem mass spectrometry is to fragment the targeted analyte ions from the isolation step, preparing them for later analysis. Collision-induced dissociation (CID)

was chosen as the fragmentation method as CID is by far the most common activation technique in ion traps.²³ Briefly, trapped ions are resonantly excited, but not ejected, by a supplemental AC potential on the endcaps. Collisions between the buffer gas and analyte ions convert the ions' kinetic energy into internal energy, causing the breaking of chemical bonds. High pressure CID was implemented much the same way as in a low pressure device. In general, a few volts of supplemental AC for a few hundreds of microseconds was used to convert precursor ions into fragment ions. An example of successful CID at 1 Torr of air can be seen in Figure 3.12, with the molecular ion of bromobenzene (m/z 156) from a full mass spectrum (black trace) being isolated from the phenyl ion fragment at m/z 77 (blue trace) and then dissociated into smaller fragments (red traces). For the molecular ion of bromobenzene, a loss of bromine results during the CID process and a single phenyl cation fragment peak (m/z 77) appears.

A further example of successful fragmentation at high pressure is shown in Figure 3.13. In this experiment, N,N-dimethylaniline is used as the analyte. The full mass spectrum (black trace) shows only a single peak so there was no need for an isolation step. CID fragmentation is shown in the red trace where consecutive losses of the methyl groups and the nitrogen atom from the molecular ion resulted in peaks at m/z 77, 91, and 106. An important result of this experiment is that new fragments, not seen in the initial mass spectrum, were formed by CID. These new peaks yield valuable chemical information about the analyte that can be used to differentiate the target analyte from interferences that have the same mass-to-charge ratio.

So far, the focus has been on analyzing volatile organic compounds that are easily introduced into the HPMS system. Recently, however, HPMS systems have been shown to couple effectively with electrospray ionization,²⁴ which is a known strategy for introducing large chemicals into the gas phase.^{25,26} The coupling of these technologies can be used to analyze

nonvolatile compounds, including peptides and proteins. Monitoring nonvolatile compounds is important for water quality studies, bioreactor feedback loops, clinical diagnostics, and screens for drugs of abuse. When studying large biological analytes, such as in the field of proteomics, tandem mass spectrometry is an extremely important tool that provides additional chemical information about the targeted species.^{27, 28} In Figure 3.14, the black trace shows a full mass spectrum resulting from the electrospray ionization of a tryptophan solution infused from a microchip device.^{29, 30} The highest mass-to-charge species in the full scan (m/z 405, black trace) appears to be a proton-bound dimer of the amino acid. This ion was subsequently isolated (blue trace) and activated, generating the protonated molecule (m/z 200) (red trace). Because the activation broke only a non-covalent bond, the required intensity of supplemental AC was low ($4 V_{P-P}$) and the total signal between fragment and parent ion was very close ($\sim 99\%$) to the total signal in the isolation scan.

Peptides can be significantly more difficult chemicals to fragment due to their relatively high number of chemical bonds. The internal energy necessary for breaking these chemical bonds can be dissipated throughout these degrees of freedom, requiring a larger amount of energy before any bonds are broken. In Figure 3.15, a common peptide in cell signaling experiments (Arg-Gly-Glu-Ser) is infused into the HPMS and successfully fragmented. The full mass spectrum (black trace) is dominated by the protonated molecule (m/z 450). This peak is successfully isolated (blue trace) and fragmented (red trace). By comparing the fragmentation spectrum and a zoom of the full scan (dashed black trace), it can be seen that many of the fragmented peaks are simply regenerated fragments from the full scan, such as those at m/z ~ 185 , ~ 233 , and ~ 266 . Additional fragmented peaks, however, are present at m/z ~ 340 , ~ 380 and ~ 412 and represent new chemical information about the sample. The peak at m/z 380, for example,

likely corresponds to loss of the serine residue from the peptide, indicating its position as a terminal amino acid.

Controlling the fragmentation pathway of an excited ion is another method of generating additional chemical information about the targeted analyte. Figure 3.16 shows this capability at high pressure by adjusting the amplitude of the AC excitation voltage. A heated sample (65 °C) of 1,3-dichlorobenzene was used as the model analyte and produced peaks at m/z 75, 110, 145, and 180. The highest mass-to-charge ion at m/z 180, taken to be trichlorobenzene and thought to be a reaction product from the heated sample, was then successfully isolated (blue trace) by boundary ejection. After peak isolation, the amplitude of the AC supplemental voltage was changed between scans to explore the fragmentation patterns while all other experimental conditions were held constant. As the voltage was increased from 5.3 (red trace) to 6.5 (orange trace) to 9.5 (purple trace) V_{p-p} , significantly lower m/z fragments were generated. The fragment ion populations appear to be directly related as consecutive dissociations of chlorine atoms from the isolated molecular ion. Reaching consecutive dissociation pathways suggests one of two possibilities. First, there may be a fast addition of energy relative to the dissociation times. The traditional CID of trapped ions is often regarded as a “slow-heating” technique,³¹ meaning the lowest energy bonds are likely to be broken first, and the excitation is stopped as the ions fall out of resonance. In this experiment, it is possible that the energy deposition occurs in relatively large increments due to the mechanics of the collisions, as discussed in the following section. The kinetics of this particular dissociation pathway are also unknown. Second, there may be a continued addition of energy even after primary fragmentation. This result would be unexpected based on the large difference in secular frequencies between the precursor and fragment ions. Nonetheless, controlling the predominant fragment ion under HPMS conditions is possible.

A similar experiment investigating the effect of the AC supplemental voltage on N,N-dimethylaniline is shown in a false color plot in Figure 3.17. Here, the color dimension represents intensity (low to high intensity is shown from blue to white to red) and the horizontal axis is the mass axis, such that each horizontal slice of the plot is a mass spectrum. The vertical axis is the intensity of supplemental AC applied to the endcap. The signal centered around m/z 121 is the capped intensity of the molecular ion of N,N-dimethylaniline and thus shows no variation over the different voltages. The remainder of the plot shows which fragments (m/z 77, 91, 106) are most abundant for a given excitation amplitude (4-10 V_{P-P}). It can be seen that with 4 V_{P-P} AC, there is very little fragmentation, but with 5 V_{P-P} AC, there is a strong signal from a fragment at m/z 106. With 6-7 V_{P-P} , however, the most intense fragment peak is shifted downwards to m/z 91. If more than 8 V_{P-P} is applied, there is essentially no fragmentation occurring before ions are completely ejected from the trap.

As described previously, SLITs provide an increase in sensitivity over CITs and are therefore useful in HPMS. The improved sensitivity may also aid tandem mass spectrometry due to a larger initial population of isolated ions, leading to an increase in the retained number of low efficiency fragment ions and therefore improved detection. Figure 3.18 displays the results of an analogous experiment to that shown in Figure 3.17, but in a SLIT instead of a CIT. The color scale is normalized to the same blue to white to red gradient, but notice that the absolute intensity has increased (from ~10 mV to ~20 mV) due to the enhanced sensitivity of the SLIT. There is a slight variation in the fragmentation pattern in that fragmentation is not induced until around 5 V_{P-P} is applied. Again, as voltages increase, the predominant fragment peak shifts from m/z 106 to m/z 91. When more than 8 V_{P-P} AC is applied, all of the ions are ejected from the trap without fragmenting. The physical reason for requiring increased voltage to induce fragmentation is

unclear. It is possible that the resonant excitation is not as strong due to subtle changes in the geometry. An alternate explanation is that since ions are unconstrained in the y-axis of a SLIT, collisions may divert ions along that axis, inhibiting the deposition of internal energy. Still, the differences are moderately small and CID is shown to be effective in both CIT and SLIT geometries under HPMS conditions.

These experiments have demonstrated the capability to induce fragmentation in HPMS conditions. By elucidating the chemical structure of the targeted analytes, it is possible to differentiate between analytes that would otherwise appear isobaric. Given the poorer resolution in HPMS systems, this ability greatly enhances the selectivity which should in turn limit the false positive rate.

3.5 Conclusions

In this chapter, several important forms of ion manipulation have been shown with 1 Torr of air buffer gas. First, several methods were developed for spatial control of ions along the typically unconstrained axis of a stretched length ion trap. The combination of a tapered geometry with a DC field was shown to be moderately effective, but the addition of supplemental electrodes between the ring electrode and endcaps was significantly more effective. Furthermore, this technique largely preserved resolution and improved sensitivity.

Ion isolation was also shown through: apex isolation, multi-frequency excitation isolation, and partial instability scan isolation. The ability to perform a selective, efficient isolation is critical to implementing tandem mass spectrometry within an ion trap. It is also critically important in fields such as ion spectroscopy, where it is imperative to have a pure

species as the trapped ion population. Multi-frequency excitation isolation is a strategy that exploits the broad interaction bandwidths of ions in HPMS systems and represents a low-power, simple strategy for fast isolation in a portable device.

Perhaps the most important form of ion manipulation demonstrated was the ability to induce fragmentation. The capability to perform CID is crucial to incorporating tandem mass spectrometry into a portable system. It was shown that CID is, in fact, quite possible and practical at 1 Torr of air buffer gas across a variety of analytes, even in systems with shallower pseudopotential well depths than conventional ion trap mass spectrometers. This capability was demonstrated in both CIT and SLIT geometries. The resulting chemical information from fragmentation scans can greatly improve the selectivity of an instrument in identifying an unknown compound, which can be important in situations where false positives have high costs, monetary or otherwise.

Further improvements in CID efficiency could greatly aid in instrumental capabilities. Low abundances of precursor ions currently are difficult to analyze due to even lower intensity fragment ions. Investigations into the relevant parameters of fragmentation efficiency, such as pressure, buffer gas identity, and pseudopotential well depth as defined by drive frequency and trap size will be discussed in Chapter 4 of this work.

Despite a factor of 1000 more collisions than in a conventional ion trap with a buffer gas 7x more massive than the traditional helium, it has been shown that it is possible to control and manipulate trapped ions in HPMS conditions. Various methods of interaction have been used to unlock important functionalities to improve the sensitivity and selectivity of a high pressure portable device.

3.6 Figures

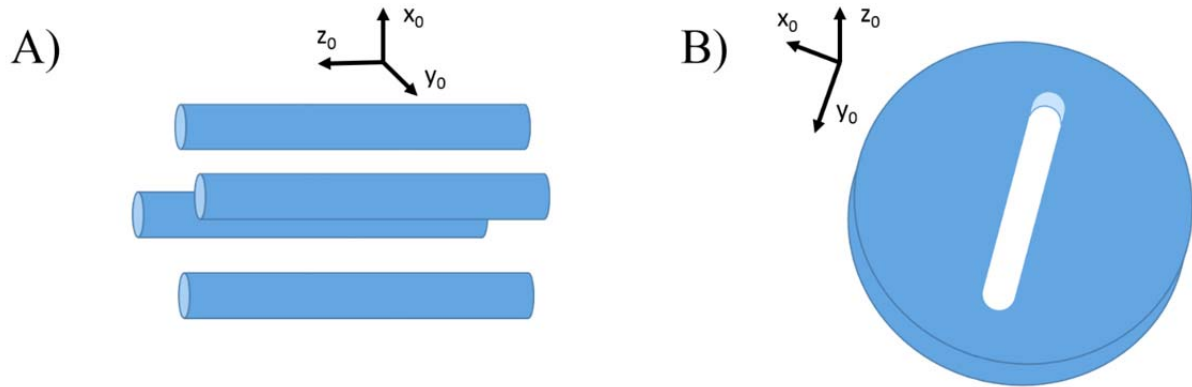


Figure 3.1. Ring electrode geometries and axis nomenclature for A) Linear Ion Traps and B) Stretched Length Ion Traps. Endcaps must be added in the z -dimension for both geometries to create effective trapping fields.

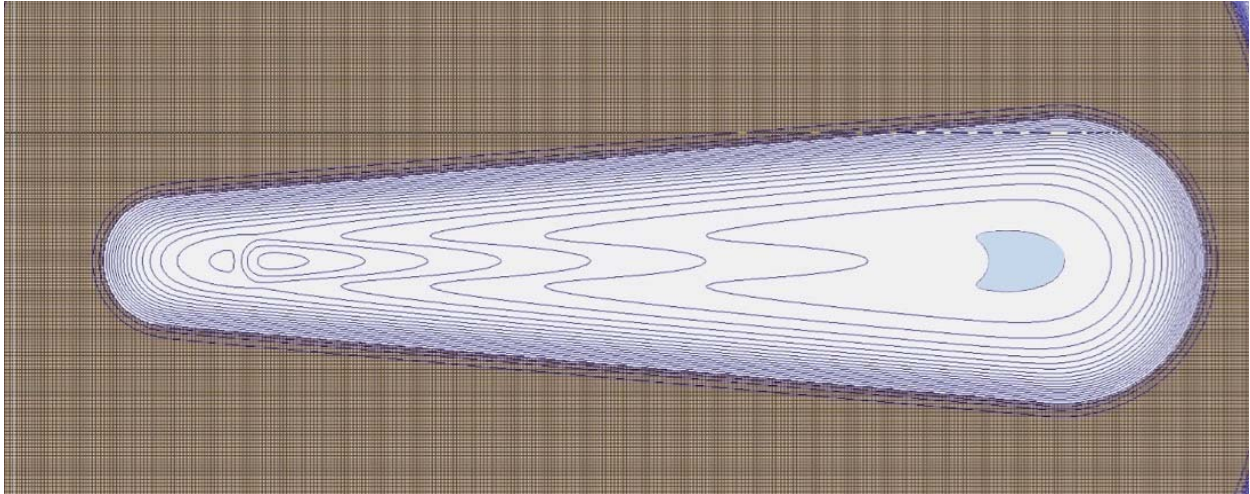


Figure 3.2. Isopotential lines (in blue) in a tapered SLIT geometry resulting from voltage applied to the electrode. The shaded area denotes the valley of potentials within the trap when a positive potential is applied and where ions should locate. When a negative potential is applied, this point is the least negative.

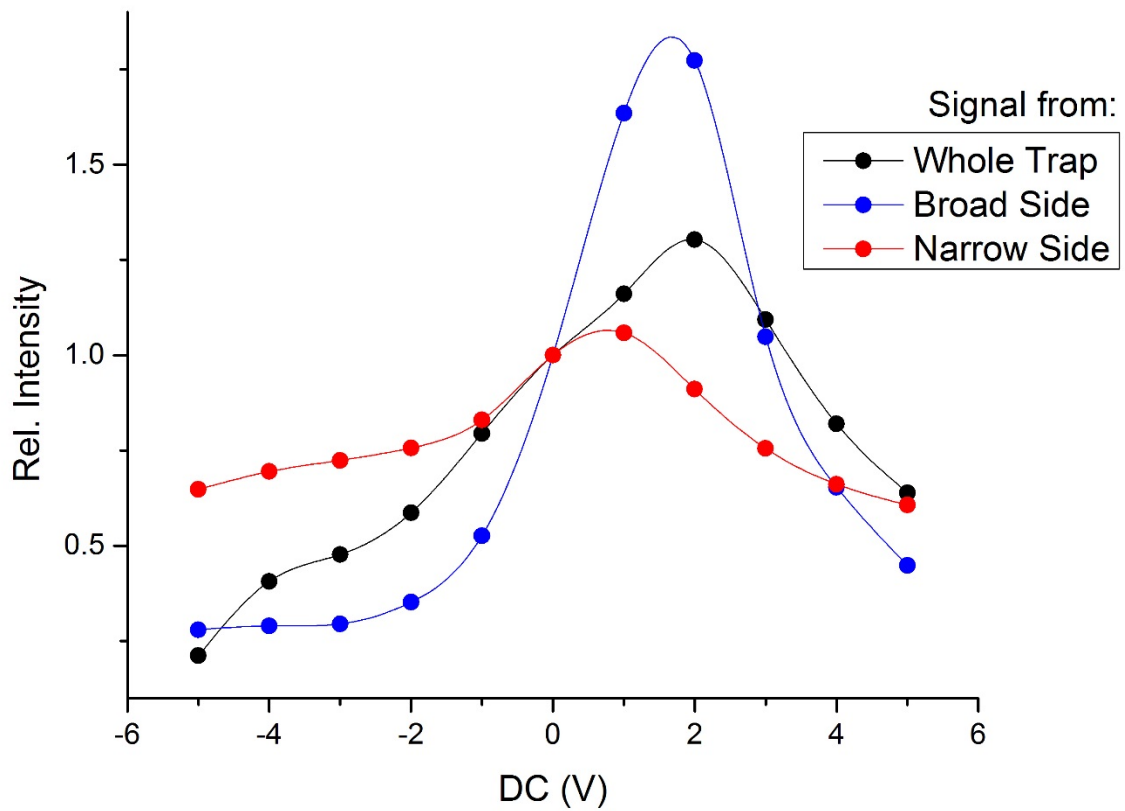


Figure 3.3. Plot of the relative intensity of signal from a tapered SLIT with varied DC voltage on the ring electrode. By using blocking electrodes, signal was measured from: the whole trap (black trace), the broad side of the trap (blue trace), and the narrow side of the trap (red trace).

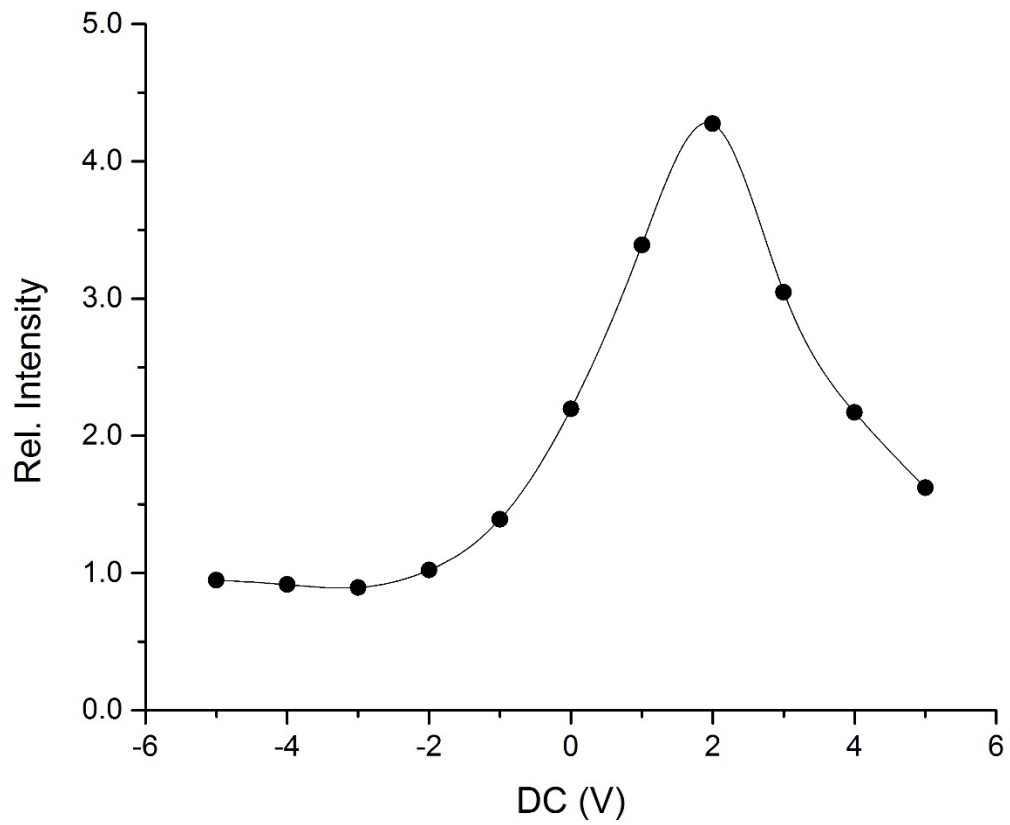


Figure 3.4. Plot showing the ratio of the intensity of signal measured from the broad side of the trap to the intensity of signal measured from the narrow side of the trap. A blocking electrode was used to isolate the signal from each half.

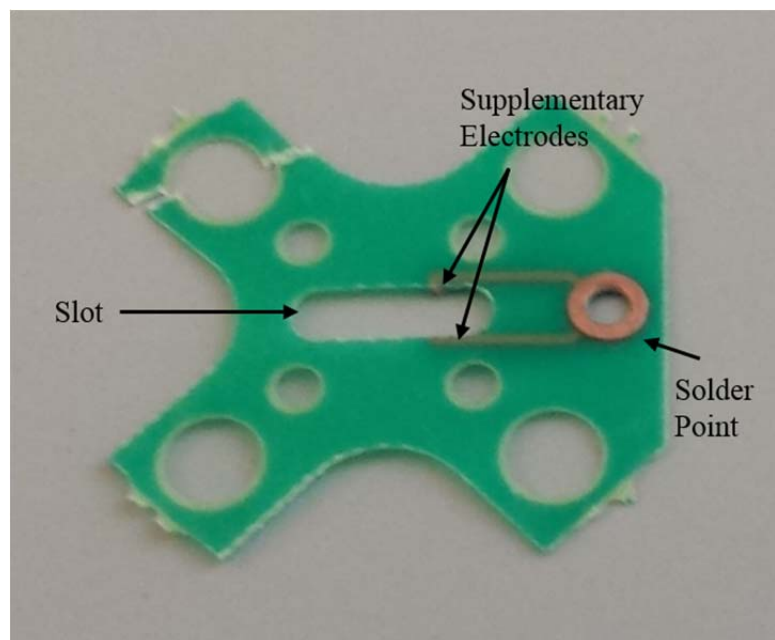


Figure 3.5. Picture of printed circuit board with supplemental electrodes used for spatial manipulation of ions in the SLIT.

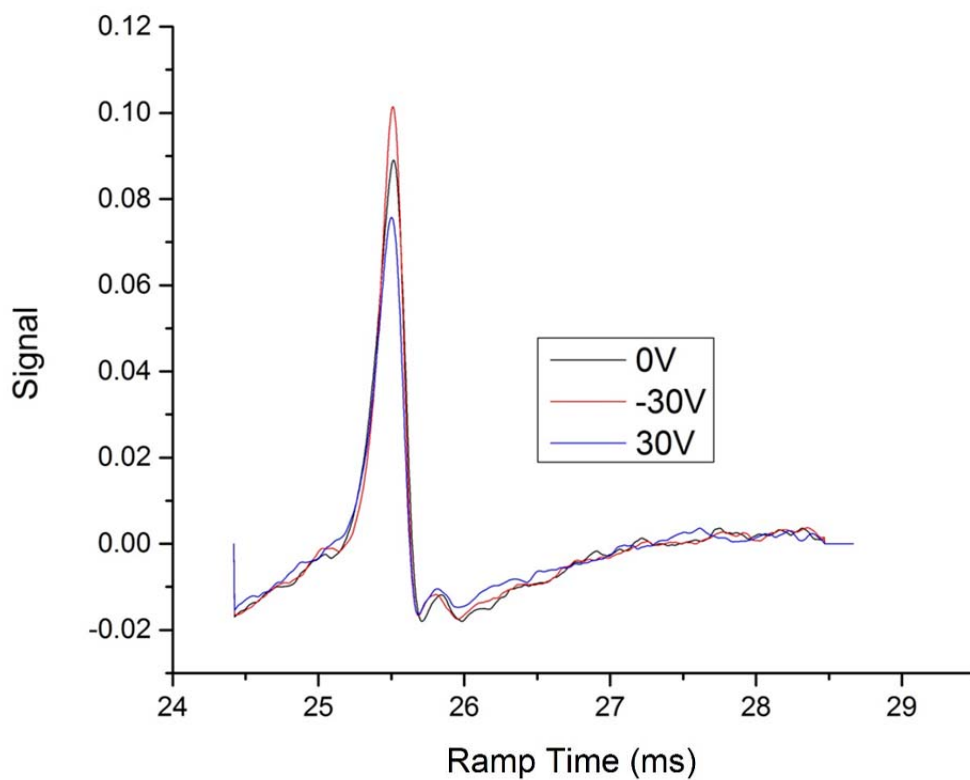


Figure 3.6. Mass spectra of N,N-dimethylaniline in SLIT with supplementary electrodes. The plot shows intensity of spectra with: 0 V (black trace), -30 V (red trace), and 30 V (blue trace) DC potential applied to the supplementary electrodes.

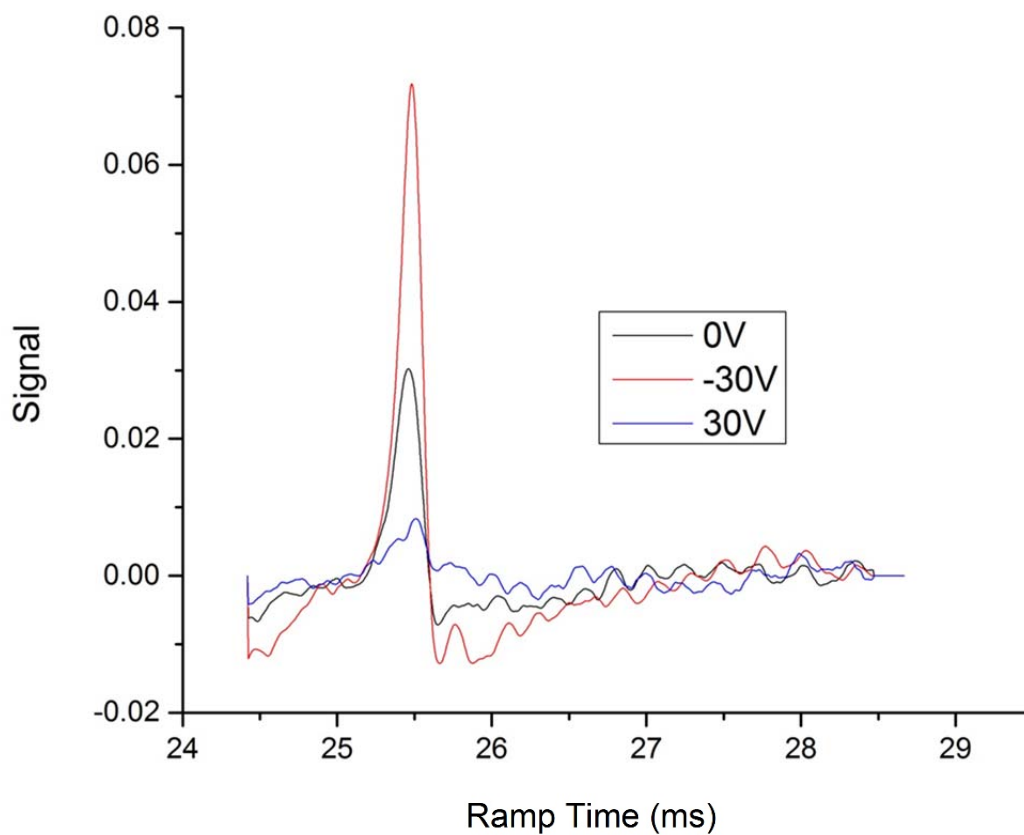


Figure 3.7. Mass spectra of N,N-dimethylaniline from the side of the SLIT with supplementary electrodes. A blocking electrode was placed between the SLIT and detector, blocking ions on opposite side of the SLIT-supplementary side from reaching detector. The plot shows intensity of spectra with: 0 V (black trace), -30 V (red trace), and 30 V (blue trace) DC potential applied to supplementary electrodes.

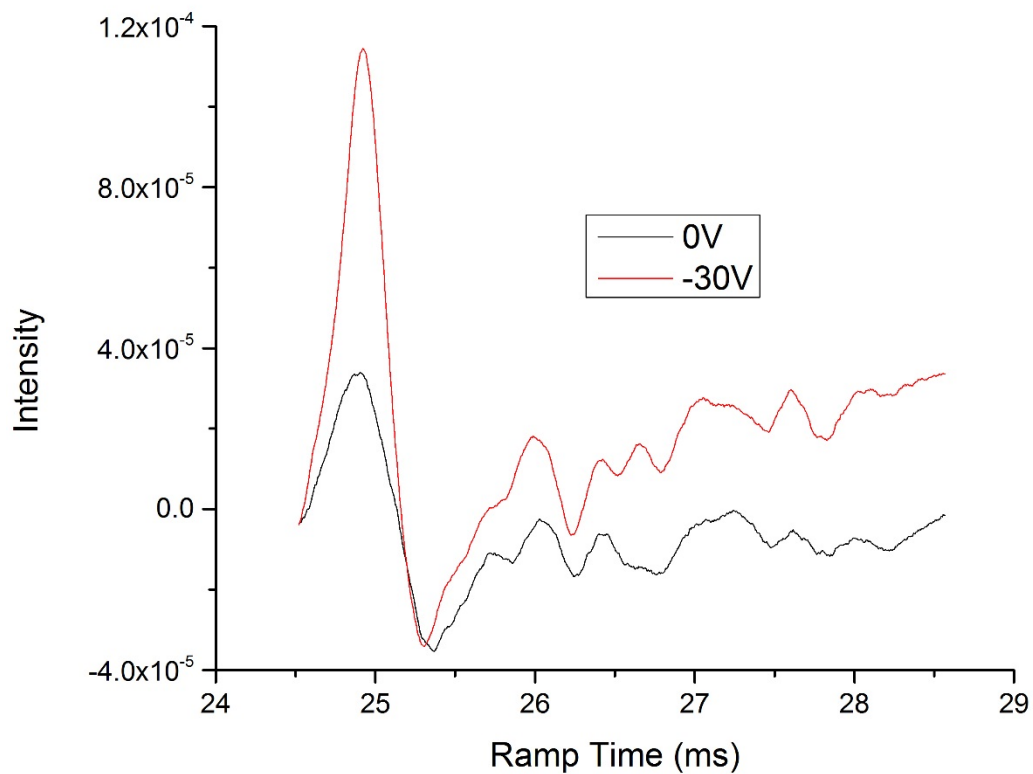


Figure 3.8. Mass spectra of N,N-dimethylaniline from the side of the SLIT with supplementary electrodes, with blocking electrodes preventing detection from the other side of the trap and ionization on the side of the supplementary electrodes. There is no line of sight between ionization source and detector. The plot shows intensity of spectra with: 0 V (black trace), -30 V (red trace) DC potential applied to supplementary electrodes.

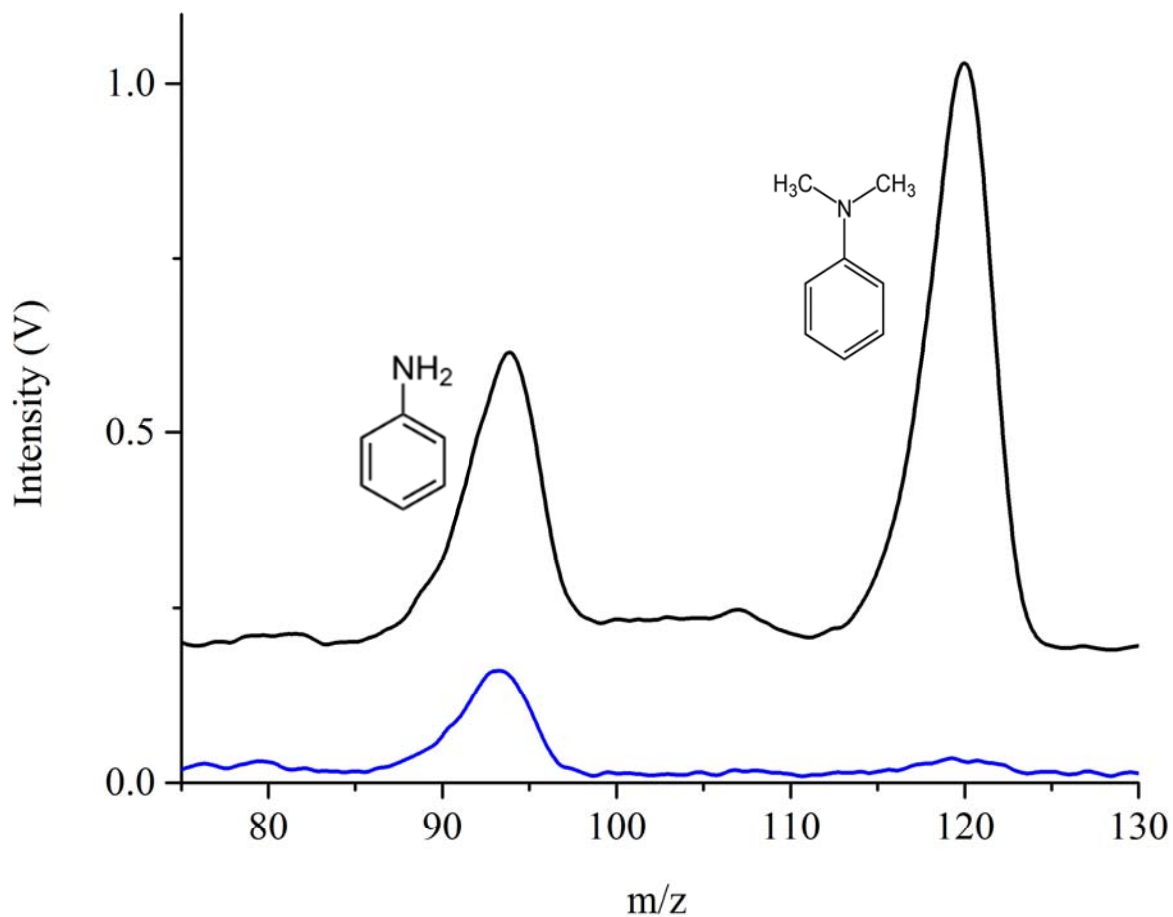


Figure 3.9. Plot demonstrating apex isolation of aniline molecular ion (m/z 93) from N,N-dimethylaniline molecular ion (m/z 121). The black trace is a full scan and blue trace is a scan after apex isolation of the target ion population.

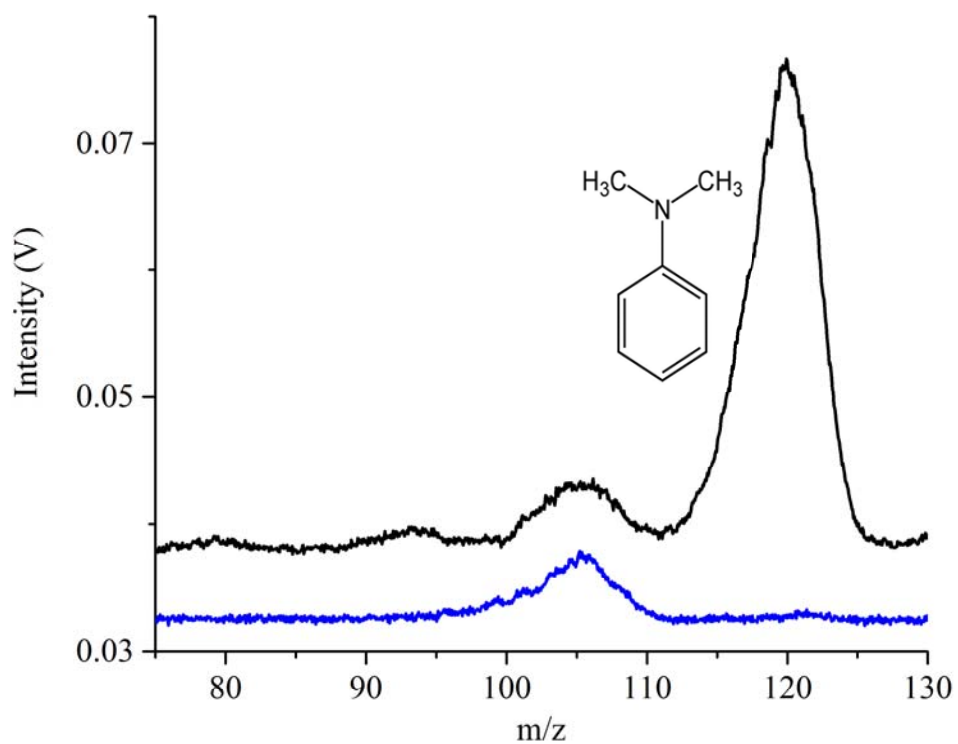


Figure 3.10. Plot demonstrating multi-frequency isolation of a fragment ion (m/z 105) from N,N-dimethylaniline molecular ion (m/z 121). The black trace is the full scan and blue trace is a scan after isolating the target ion population.

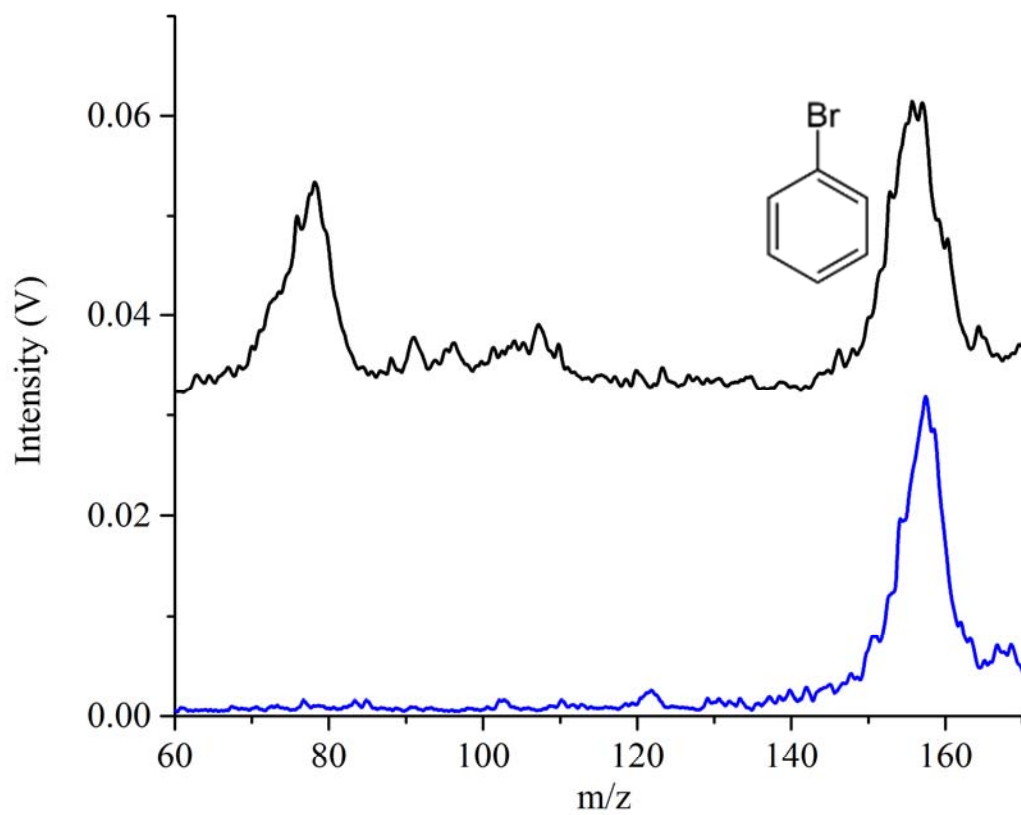


Figure 3.11. Plot demonstrating partial instability scan isolation of phenyl fragment ion (m/z 77) from bromobenzene molecular ion (m/z 156). The black trace is a full scan and blue trace is a scan after isolating the target ion population.

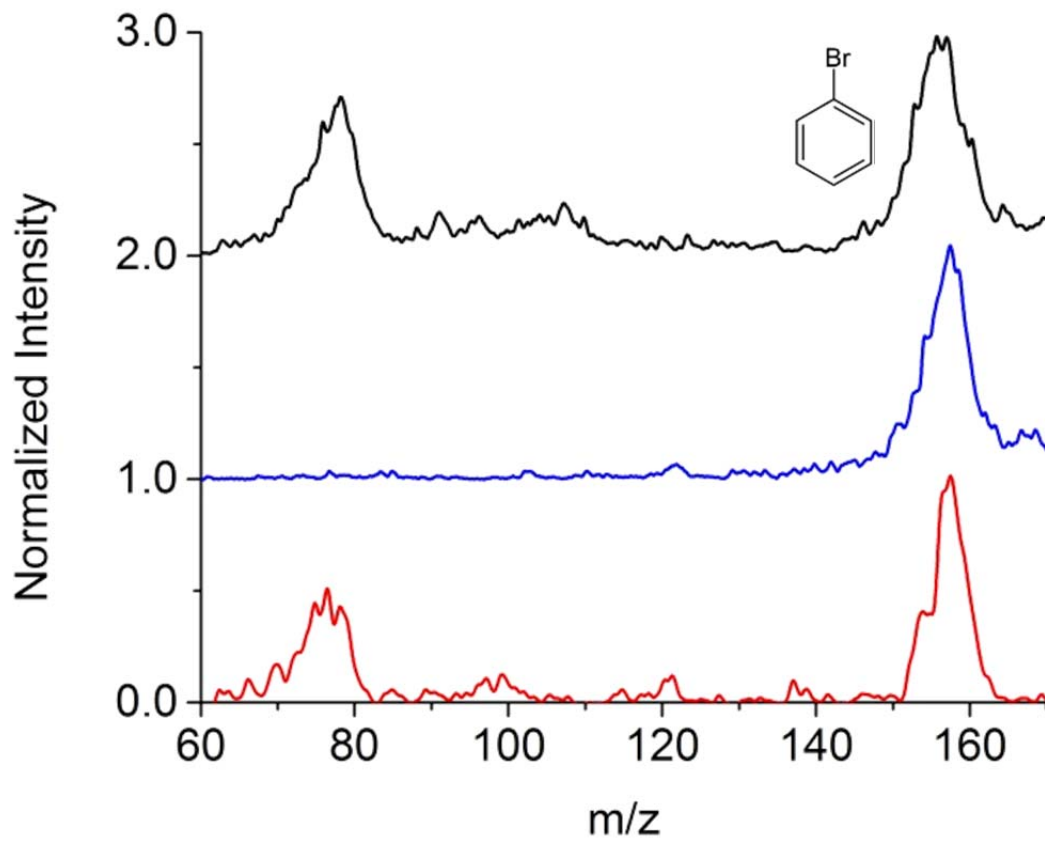


Figure 3.12. Tandem mass spectra of bromobenzene (molecular ion m/z 156). The black trace is a full scan, the blue trace is a post-isolation spectrum, and the red trace is taken after collision induced dissociation.

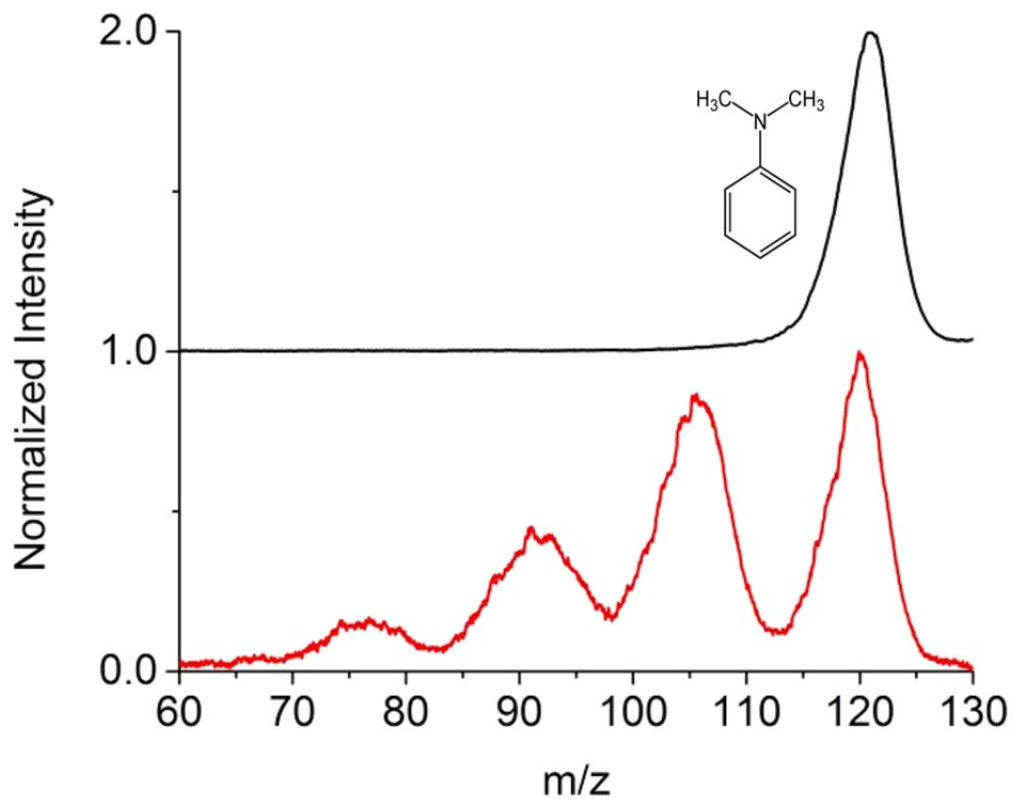


Figure 3.13. Tandem mass spectra of N,N-dimethylaniline (molecular ion m/z 121). The black trace is a full scan, and the red trace is taken after collision induced dissociation.

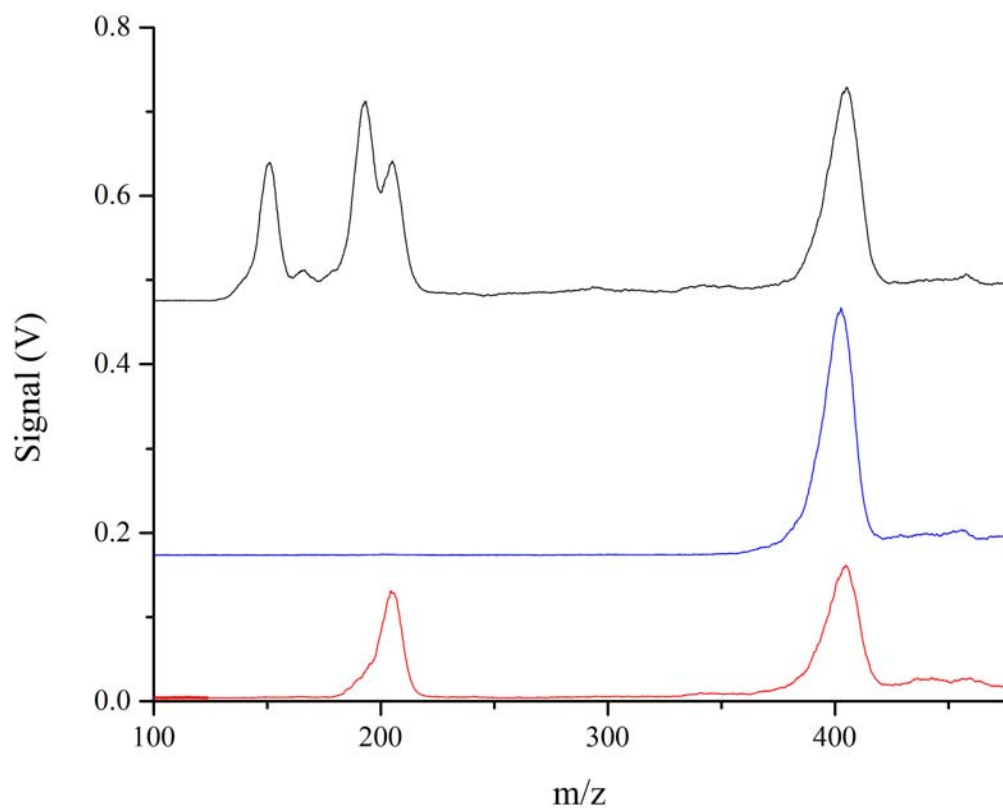


Figure 3.14. Tandem mass spectra of tryptophan (proton bound dimer m/z 405). The black trace is a full scan, the blue trace is a post-isolation spectrum, and the red trace is taken after collision induced dissociation.

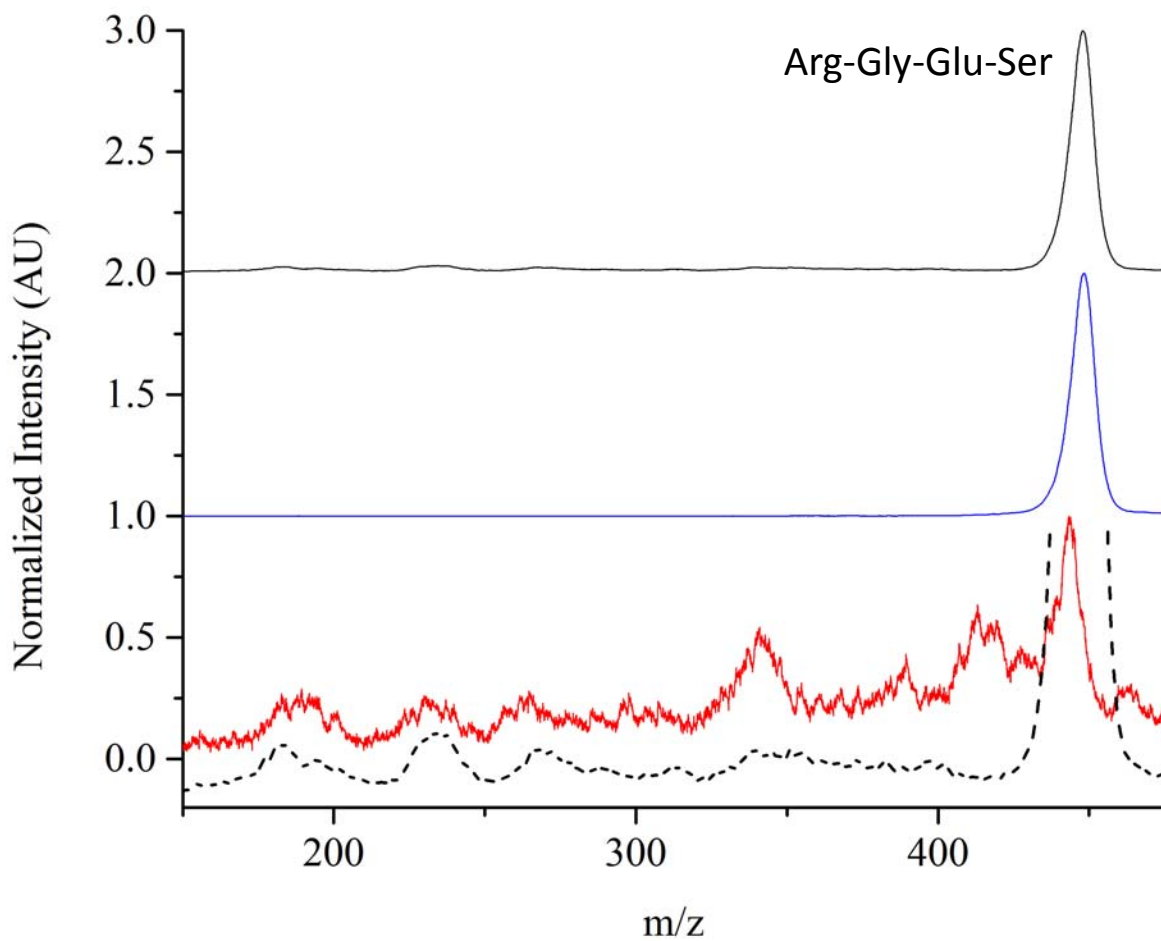


Figure 3.15. Tandem mass spectra of RGES (Arginine-Glycine-Glutamic Acid-Serine) peptide (protonate molecule m/z 447). The black trace is a full scan, the blue trace is a post-isolation spectrum, and red trace is taken after collision induced dissociation. The dashed black trace is a zoom of the full scan for comparison purposes.

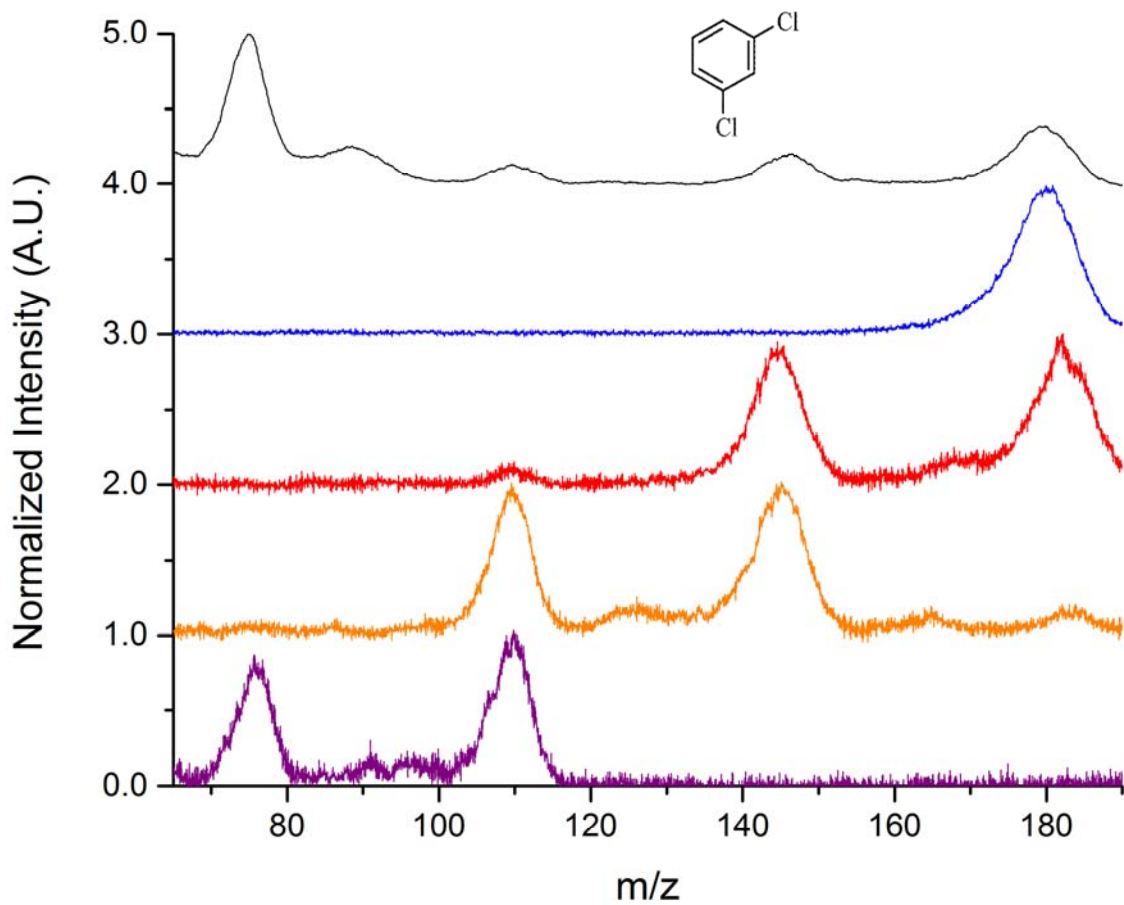


Figure 3.16. Series of mass spectra from a 1,3-dichlorobenzene sample showing effect of various AC excitation voltages. The black trace is the initial molecular full scan, and the blue trace is the isolated parent ion. The remaining traces show fragmentation patterns with 5.3 V_{p-p} (red trace), 6.5 V_{p-p} (orange trace) and 9.5 V_{p-p} (purple trace) AC excitation voltages applied.

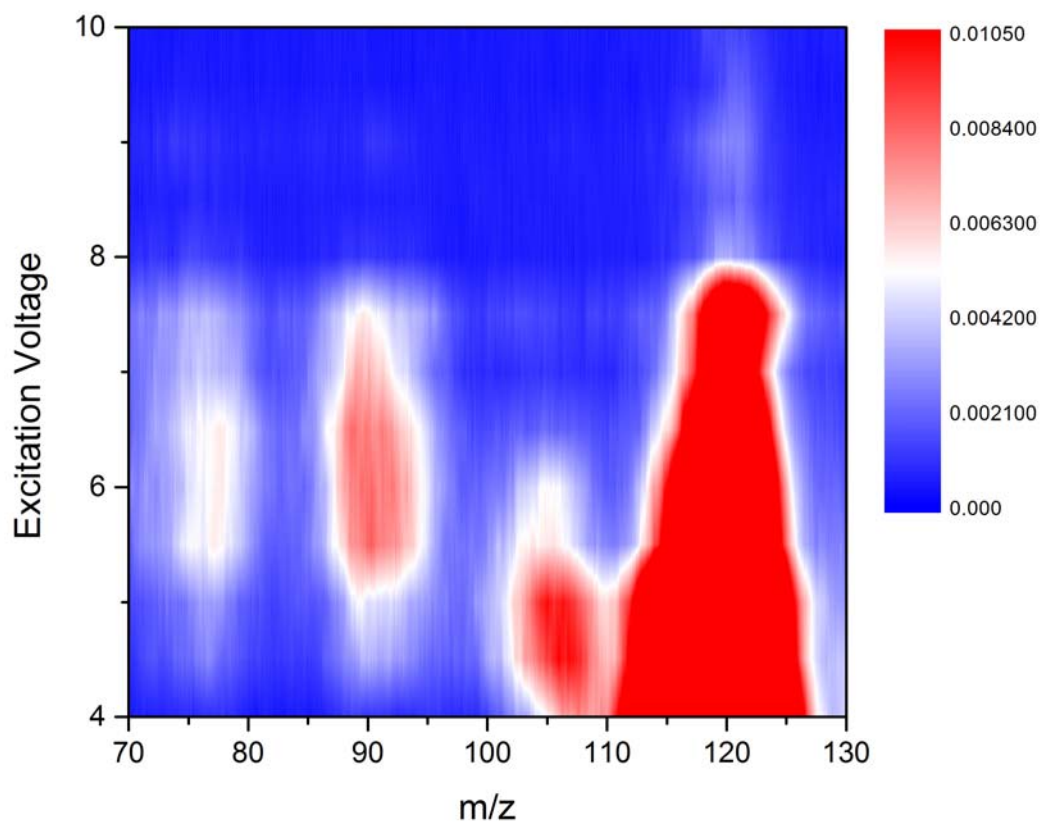


Figure 3.17. Signal intensity heat map from spectra of N,N-dimethylaniline in a cylindrical ion trap with varied excitation voltages applied. Molecular ion (m/z 121) fragmentation is apparent at m/z 77, 91, 105.

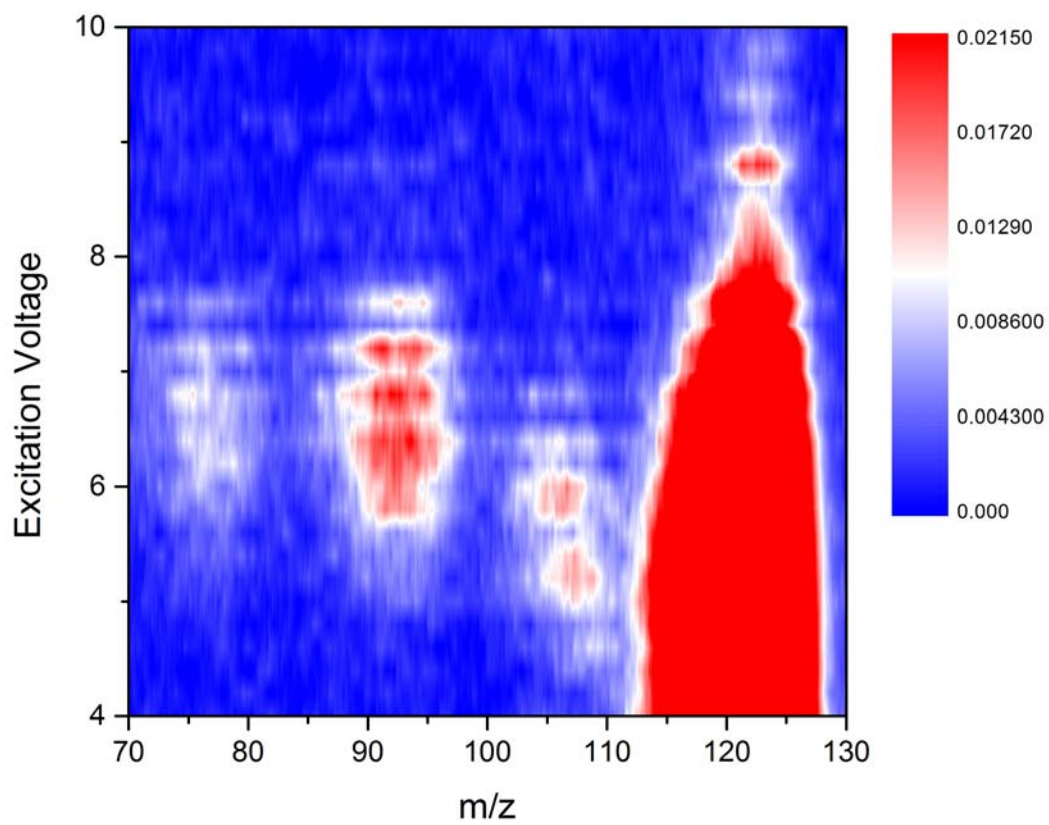


Figure 3.18. Signal intensity heat map from spectra of N,N-dimethylaniline in a stretched length ion trap with varied excitation voltages applied. Molecular ion (m/z 121) fragmentation is apparent at m/z 77, 91, 105.

3.7 REFERENCES

1. Blakeman, K.H., et al., *High Pressure Mass Spectrometry: The Generation of Mass Spectra at Operating Pressures Exceeding 1 Torr in a Microscale Cylindrical Ion Trap*. Analytical Chemistry, 2016. **88**(10): p. 5378-5384.
2. Schultze, K., *Advanced System Components for the Development of a Handheld Ion Trap Mass Spectrometer*. Dissertation, University of North Carolina at Chapel Hill, 2014.
3. Ramsey, J.M. and K. Schultze, *Miniature charged particle trap with elongated trapping region for mass spectrometry*. 2014, Google Patents.
4. Kassel, D.B. and K. Biemann, *Differentiation of hydroxyproline isomers and isobars in peptides by tandem mass spectrometry*. Analytical Chemistry, 1990. **62**(15): p. 1691-1695.
5. Zhang, J. and J.S. Brodbelt, *Structural characterization and isomer differentiation of chalcones by electrospray ionization tandem mass spectrometry*. Journal of Mass Spectrometry, 2003. **38**(5): p. 555-572.
6. March, R.E., *Quadrupole ion traps*. Mass Spectrom. Rev., 2009. **28**(6): p. 961-989.
7. March, R.E., *An Introduction to Quadrupole Ion Trap Mass Spectrometry*. J. Mass Spectrom., 1997. **32**(4): p. 351-369.
8. Stockett, M.H., et al., *A cylindrical quadrupole ion trap in combination with an electrospray ion source for gas-phase luminescence and absorption spectroscopy*. Review of Scientific Instruments, 2016. **87**(5): p. 053103.
9. Seaiby, C., et al., *IR-induced conformational isomerization of a helical peptide in a cold ion trap*. The Journal of Chemical Physics, 2016. **144**(1): p. 014304.
10. Blatt, R., U. Schmeling, and G. Werth, *On the sensitivity of ion traps for spectroscopic applications*. Applied physics, 1979. **20**(4): p. 295-298.
11. Fortson, E.N., F.G. Major, and H.G. Dehmelt, *ULTRAHIGH RESOLUTION $dF=0$, $+1$ (He^3)⁺ HFS SPECTRA BY AN ION-STORAGE COLLISION TECHNIQUE*. Physical Review Letters, 1966. **16**(6): p. 221-225.
12. Hager, J.W., *A new linear ion trap mass spectrometer*. Rapid Communications in Mass Spectrometry, 2002. **16**(6): p. 512-526.

13. Schwartz, J.C., M.W. Senko, and J.E.P. Syka, *A two-dimensional quadrupole ion trap mass spectrometer*. Journal of the American Society for Mass Spectrometry, 2002. **13**(6): p. 659-669.
14. Jonscher, K.R. and J.R. Yates, *The Quadrupole Ion Trap Mass Spectrometer—A Small Solution to a Big Challenge*. Analytical Biochemistry, 1997. **244**(1): p. 1-15.
15. Londry, F.A. and J.W. Hager, *Mass selective axial ion ejection from a linear quadrupole ion trap*. Journal of the American Society for Mass Spectrometry, 2003. **14**(10): p. 1130-1147.
16. Wilcox, B.E., C.L. Hendrickson, and A.G. Marshall, *Improved ion extraction from a linear octopole ion trap: SIMION analysis and experimental demonstration*. Journal of the American Society for Mass Spectrometry, 2002. **13**(11): p. 1304-1312.
17. Lee, J., et al., *Simulation of duty cycle-based trapping and ejection of massive ions using linear digital quadrupoles: The enabling technology for high resolution time-of-flight mass spectrometry in the ultra high mass range*. International Journal of Mass Spectrometry, 2011. **304**(1): p. 36-40.
18. Wang, X., et al., *Increasing the trapping mass range to $m/z = 109$ —A major step toward high resolution mass analysis of intact RNA, DNA and viruses*. International Journal of Mass Spectrometry, 2012. **328–329**: p. 28-35.
19. March, R.E. and J.F. Todd, *Practical aspects of ion trap mass spectrometry: Chemical, environmental, and biomedical applications*. Vol. 3. 1995: CRC press.
20. Guan, S. and A.G. Marshall, *Stored waveform inverse Fourier transform (SWIFT) ion excitation in trapped-ion mass spectrometry: Theory and applications*. International Journal of Mass Spectrometry and Ion Processes, 1996. **157**: p. 5-37.
21. Campbell, J.M., B.A. Collings, and D.J. Douglas, *A new linear ion trap time-of-flight system with tandem mass spectrometry capabilities*. Rapid Communications in Mass Spectrometry, 1998. **12**(20): p. 1463-1474.
22. Snyder, D.T. and R.G. Cooks, *Ion Isolation in a Linear Ion Trap Using Dual Resonance Frequencies*. Journal of The American Society for Mass Spectrometry, 2016. **27**(12): p. 1906-1913.
23. March, R.E. and J.F.J. Todd, *Practical Aspects of Trapped Ion Mass Spectrometry, Volume IV: Theory and Instrumentation*. 2010: CRC Press.
24. Gilliland, M. and J.M. Ramsey, *Capillary Electrophoresis Electrospray Ionization High Pressure Mass Spectrometry (CE-ESI-HPMS)*. Unpublished, 2017.

25. Fenn, J.B., *Electrospray Wings for Molecular Elephants (Nobel Lecture)*. Angewandte Chemie International Edition, 2003. **42**(33): p. 3871-3894.
26. Whitehouse, C.M., et al., *Electrospray ionization for mass-spectrometry of large biomolecules*. Science, 1989. **246**(4926): p. 64-71.
27. Zhao, Y., et al., *Development and validation of a sensitive liquid chromatographic–tandem mass spectrometric method for the simultaneous analysis of granisetron and 7-hydroxy granisetron in human plasma and urine samples: application in a clinical pharmacokinetic study in pregnant subject*. Biomedical Chromatography, 2016. **30**(2): p. 149-154.
28. Kretschmer, P.M., et al., *A liquid chromatography–tandem mass spectrometry assay for the detection and quantification of trehalose in biological samples*. Journal of Chromatography B, 2016. **1033–1034**: p. 9-16.
29. Black, W.A., et al., *Utilizing Microchip Capillary Electrophoresis Electrospray Ionization for Hydrogen Exchange Mass Spectrometry*. Analytical chemistry, 2015. **87**(12): p. 6280-6287.
30. Mellors, J., et al., *Fully integrated glass microfluidic device for performing high-efficiency capillary electrophoresis and electrospray ionization mass spectrometry*. Analytical chemistry, 2008. **80**(18): p. 6881-6887.
31. McLuckey, S.A. and D.E. Goeringer, *Slow heating methods in tandem mass spectrometry*. Journal of Mass Spectrometry, 1997. **32**(5): p. 461-474.

Chapter 4: Improving the Selectivity of High Pressure Mass Spectrometry

4.1 Introduction

High pressure mass spectrometry (HPMS) has been developed as a strategy to bring rapid, informative chemical analysis into field environments.^{1,2} Portability and quick response times are driving factors in assessing whether a system is suited for rapid threat detection, providing actionable intelligence on a faster timeline than harm from the potential threat.^{3,4} Another important characteristic, however, is selectivity.⁵ A misidentification or a false positive, due to poor selectivity, can result in enacting of costly response protocols for a threat that is not actually present.

The loss in resolution of HPMS due to collisional broadening causes more compounds to appear isobaric, meaning they have the same observed mass-to-charge ratio. This overlap of observed m/z values is especially problematic when multiple potential interferences are present such as in an industrial setting. This can lead to situations where the number of analytes increases the number of peaks beyond the resolving capabilities of the instrument, resulting in many unresolved peaks.⁶ In other cases, it is difficult to disentangle the sources of each peak, causing misidentification due to the chimeric spectrum.⁷ A powerful tool for differentiating isobars is tandem mass spectrometry where target analytes are isolated, fragmented and then reanalyzed via MS. The fragmentation pattern yields extra information based on the chemical structure of the analyte that can be used to help identify the original compound.⁸⁻¹⁰ To maximize

the information gained from this technique, however, it is important to reach high fragmentation efficiencies such that all fragments can be readily analyzed.

Another strategy for improving the selectivity of a mass spectrometer is to couple a separation technique to the front end of the mass spectrometer. Gas chromatography (GC) has been demonstrated as a flexible, powerful technology appropriate for miniaturization and portability¹¹⁻¹³ and has been widely coupled to mass spectrometers.^{14, 15} Although this implementation adds complexity and power costs to a portable HPMS instrument, it provides several advantages. First, instrumental selectivity is improved based on the chemical information obtained from retention times measured during the GC separation. Second, it becomes possible to analyze complex mixtures that would otherwise be unidentifiable.

Investigated in this chapter are methods for improving the selectivity of an HPMS system by maximizing the fragmentation efficiency of collision-induced dissociation (CID) and by coupling a high pressure mass spectrometer to a GC separation. To maximize CID efficiency, the parameters studied are pseudopotential well depth (controlled by drive RF frequency and trap size), buffer gas pressure, and buffer gas identity. These parameters are investigated primarily in regards to their effects on fragmentation efficiency. The compatibility of a GC separation with HPMS detection is explored using a complex mixture of chemical warfare agent simulants (CWASs).

4.2 Improving CID Efficiency

Fragmentation efficiency in CID is important for a variety of reasons. CID does not have a perfect conversion efficiency so the signal from any resulting fragments could potentially fall

below detection levels, resulting in no gain in chemical identification.¹⁶ Higher fragmentation efficiencies therefore should lead to more fragment ions and improve the detection limits of the second MS stage. This improved sensitivity can be critical for analytes with low initial concentrations. Furthermore, there are cases where a single level of tandem mass spectrometry is insufficient for confident chemical identification, and further stages are needed for species differentiation. An advantage of tandem mass spectrometry in an ion trap is that the steps can be successively repeated as needed as long as sufficient signal strength remains. High CID efficiencies then can result in multiple stages of tandem mass spectrometry analysis,¹⁷ unlocking different fragmentation pathways at each stage and yielding additional information about the chemical of interest. This unique advantage of ion traps is highly desirable for portable instrumentation.

Several key variables differ between HPMS CID and CID in a conventional ion trap. For HPMS, smaller traps and higher RF drive frequencies are used compared to traditional instrumentation. The decreased ion trap size and increased RF drive frequency have competing effects on the pseudopotential well depth where smaller traps reduce it and higher RF drive frequencies increase it.¹⁸ Compared to a conventional instrument, the HPMS trap size is reduced by a factor of 20x, and hence the pseudopotential well depth decreases by a factor of 400x from the original and still commonly used Finnigan design with $r_0 = 1.00$ cm.¹⁹ The RF drive frequency enhancement for standard HPMS operation, however, is only 7-10x (7-10 MHz vs 1 MHz), meaning that overall, the calculated pseudopotential well depth should be reduced by a factor of >4x.²⁰

In addition to the trap size and RF frequency, the pressure increase in buffer gas also plays a role in determining the CID efficiency. Despite miniaturization, the ~1000x increase in

pressure means that an ion will experience an increased number of collisions with a neutral buffer gas molecule on an average movement between the center and edge of the ion trap. This means that ions are far less likely to simply eject from the trap before encountering sufficient collisions to cause fragmentation. The neutral buffer gas molecules are primarily nitrogen and oxygen in HPMS as opposed to helium, and their properties, such as mass, play a part in how collisions add energy to the excited ions.²¹ Despite these fundamental differences, as seen in Chapter 3, the CID process can be carried out in largely the same manner of operation.

4.2.1 Role of Pseudopotential Well Depth

The pseudopotential well depth, as described by Dehmelt, characterizes the amount of kinetic energy an ion may have without escaping the confines of the trap.¹⁸ Resonant excitation, as used to induce fragmentation in CID, employs the same principle as resonant ejection: the amplification of the secular motion of trapped ions by resonant interaction with a supplemental AC voltage applied to the endcap.²² Note that resonant amplification of the secular motion to kinetic energies beyond the pseudopotential well depth will result in ejection of the ion. If, however, collisions with neutral buffer gas molecules inhibit this motion sufficiently, the ion will be contained within the trap. Each of these collisions, in part, converts kinetic energy into other forms, including internal energy stored in the vibrational modes of the trapped ion. The vibrational internal energy may reach high enough levels to overcome and break chemical bonds within the ion. Due to the mechanism of energy distribution through a collision, it is practically difficult to add a total amount of internal energy to an ion greater than the kinetic energy of that ion. Thus, there is a direct correlation between the pseudopotential well depth and the maximum internal energy deposited into a CID target. In other words, the pseudopotential well depth

defines the balance between resonant ejection and resonant excitation, which governs the efficiency of fragmentation.

The pseudopotential well depth for an ion is proportional to both the ion's q_z value and to the drive RF voltage (Equation 1.7). Factors that go into an ion's q_z include the ion's mass-to-charge ratio, the drive RF frequency and voltage, as well as the trap size (Equation 1.3). For our purposes, it is desirable to hold q_z constant to preserve the mass range, so the drive RF frequency and voltage while factoring in trap size are adjusted accordingly. When the drive RF frequency is increased, an increase in RF voltage is needed in order to maintain the q_z of the trapped ion. This higher voltage leads to an increase in the pseudopotential well depth. With respect to the critical dimensions of an ion trap, as the trap size decreases, the RF voltage required to preserve the ion's q_z value also decreases. Thus, the pseudopotential well depth will decrease as the ion trap is miniaturized.

Figure 4.1 shows a collection of heat maps of the fragmentation of N,N-dimethylaniline (m/z 121) at 1 Torr of air buffer gas in a SLIT with $x_0 = 270 \mu\text{m}$, $y_0 = 5 \text{ mm}$. The activation occurs with the molecular ion (m/z 121) at $q_z = 0.4$ in all panels. The color scale on this heat map represents the relative intensity of fragment ions, normalized such that the initial intensity of the precursor ion is set to a value of 1.0 and the intensity color scale varies from blue (0) to red (0.3). The horizontal axis is the mass axis, and the vertical axis displays the voltage of supplemental AC applied during the excitation step. In panel A, $\Omega = 16.4 \text{ MHz}$. Here, the unfragmented molecular ion can be seen centered at m/z 121. With around $5 V_{\text{p-p}}$ of supplemental AC, there is noticeable fragmentation, particularly at m/z 106 and slight fragmentation at m/z 91. The most intense fragmentation peak, however, accounts for only $\sim 8\%$ of the initial ion intensity. By $6 V_{\text{p-p}}$.

V_{p-p} applied supplemental AC, the peak intensities decrease as the precursor ions overcome the pseudopotential well depth.

In Figure 4.1B, the fragmentation heat map of N,N-dimethylaniline with $\Omega = 19.1$ MHz is shown. In contrast to the 16.4 MHz data, fragmentation into the m/z 106 peak is already occurring by $\sim 4 V_{p-p}$ supplemental AC and by $4.5 V_{p-p}$ supplemental AC, the fragment at m/z 91 is already present. With $6 V_{p-p}$ supplemental AC, the total intensity of all ions begins to lessen due to ions exceeding the pseudopotential well depth. The most intense fragment ion is the m/z 91 peak, occurring with $\sim 5.5 V_{p-p}$ supplemental AC. It has $\sim 18\%$ of the initial intensity of the precursor ion, a substantial improvement over the $\sim 8\%$ observed with 16.4 MHz RF drive frequency applied.

Another heat map of the fragmentation of N,N-dimethylaniline is shown in Figure 4.1C. Again, the experimental conditions are held constant except for drive RF frequency. Here, $\Omega = 20.9$ MHz was applied and fragmentation, primarily into the m/z 106 ion, is present by $\sim 4 V_{p-p}$ supplemental AC and is maximized by around $5 V_{p-p}$ supplemental AC. By this point, however, the fragment at m/z 91 appears and remains past $\sim 7 V_{p-p}$ supplemental AC applied, where the ion signal begins to decrease. The most intense fragment ion throughout these spectra is the m/z 91 fragment at $\sim 6 V_{p-p}$ supplemental AC, corresponding to $\sim 30\%$ of the signal of the initial precursor ion. This conversion efficiency is a sizable gain over the previous experiments at lower drive RF frequencies. The highest total conversion efficiency occurs when both m/z 91 and 106 fragments are present (at $\sim 5 V_{p-p}$) where $\sim 40\%$ conversion ($\sim 20\%$ efficiency of each ion) is seen.

Through Figure 4.1, it can be clearly seen that the maximum conversion efficiency increases significantly as the drive RF frequency increases. This strongly suggests that increasing

the drive RF frequency increases the pseudopotential well depth if q_z is maintained, serving to more stably trap the excited and fragmented ions. An interesting trend, however, is seen by looking at the onset voltages for the fragment at m/z 106. This ion fragments more easily at lower voltages of supplemental AC as the drive RF frequency increases (note the scale change in the vertical axis in panel C). If drive RF frequency were only affecting the CID process through deepening the pseudopotential well depth at a given q_z value, there would be no clear explanation for this trend. One possible explanation is the increased drive RF frequency is likely affecting the trapped ions through the fidelity of the secular frequency. The secular motion is better defined when there are more drive RF periods between ion-neutral collisions, meaning that increasing drive RF frequency increases this ratio and improves the fidelity of the secular motion. This would enhance the resonant characteristics, increasing the kinetic energy of ions at lower supplemental AC voltages. This in turn leads to higher internal energies and earlier fragmentation. Another explanation may also be possible. Experimentally, the excitation time was held constant for each frequency tested. As the drive RF frequency increases, so does the secular frequency and the corresponding resonant supplemental AC. Thus, in the same amount of excitation time, there are actually more periods of resonant excitation at higher drive frequencies, possibly accelerating the ions more effectively.

Another trend emerges from the lower mass fragments in Figure 4.1. The fragment at m/z 77 is strongly apparent ($\sim 12\%$) in panel C, noticeably present ($\sim 7\%$) in panel B, and only subtly visible ($\sim 1\%$) in panel A. This fragment emergence with frequency increase is likely the result of enhanced internal energy deposition, causing more of the ion to form. It is also possible that a decreased low mass cutoff at higher frequencies improves the ability to detect the lower mass-to-charge ion. Regardless of the reason, the increased frequency of drive RF enhances the

conversion efficiency of CID and in turn increases the amount of chemical information available for identification purposes. Both of these effects are important for enhancing the selectivity of the HPMS system.

Figure 4.2 shows another series of fragmentation heat maps of N,N-dimethylaniline (m/z 121) in 1 Torr of air buffer gas in a SLIT with $x_0 = 170 \mu\text{m}$ and $y_0 = 5 \text{ mm}$. This trap is significantly smaller ($\sim 37\%$ reduction in radius, $\sim 60\%$ reduction in volume) than that used to generate Figures 4.1. At the same frequency of drive RF, the pseudopotential well depth will be significantly shallower for an ion with the same q_z . In panel A, with a drive RF frequency of 19.1 MHz, there is a small amount of m/z 106 ($\sim 7\%$ relative to the initial precursor ion population) around 3 $V_{\text{P-P}}$ supplemental AC. This peak is difficult to identify in this representation, but can be seen in the raw data. By 4 $V_{\text{P-P}}$ supplemental AC, almost all ions escape from the trap with almost no fragmentation occurring. This is in stark contrast to the 270 μm trap where, with the same drive RF frequency, fragmentation occurs with m/z 106 and 91 ions appearing (Figure 4.1B).

Figure 4.2B displays another fragmentation heat map of N,N-dimethylaniline in 1 Torr of air in a SLIT with $x_0 = 170 \mu\text{m}$ with $\Omega = 20.9 \text{ MHz}$. Fragmentation is observed beginning with 3 $V_{\text{P-P}}$ supplemental AC, and by $\sim 5 V_{\text{P-P}}$ most ions are lost to resonant ejection. The most intense fragment signal comes from the m/z 106 peak with just over 3 V supplemental AC. There is $\sim 13\%$ of the signal intensity at this point relative to the intensity of the isolated precursor ion. The same trend seen with the larger trap, where the increased drive RF frequency results in significantly more efficient CID, continues here. The drive frequency in this case is also the same as that used in Figure 4.1C, but with a smaller trap. As expected, the smaller trap, due to a shallower pseudopotential well depth, has significantly reduced fragmentation efficiency.

In Figure 4.2C, a fragmentation heat map of N,N-dimethylaniline with $\Omega = 25.0$ MHz, the highest tested drive frequency, is shown. Fragmentation into ions at both m/z 91 and m/z 106 is observed with as little as 3 V_{p-p} supplemental AC. Almost all ions are lost to ejection before 7 V_{p-p} AC is applied. The most intense fragment signal is observed with the m/z 106 peak at around 4 V_{p-p} AC. The conversion efficiency at that point is $\sim 27\%$ compared to the initial precursor ion intensity. This represents a sizable increase in efficiency over the results shown in panel B, improved by the deeper pseudopotential well depth from the increase drive RF frequency.

From the experimental conditions used to generate Figures 4.1 and 4.2, it is possible to calculate the expected pseudopotential well depth for each combination of trap size and drive RF frequency. The measured conversion efficiencies for each of these points is plotted against the calculated pseudopotential well depth in Figure 4.3. As noted before, voltages are adjusted such that ions are activated with $q_z = 0.4$ in all cases. With this strategy, increased rf drive frequency deepens the pseudopotential well depth, as do larger trap dimensions. Open circles represent points from the SLIT with $x_0 = 270$ μm while closed circles show data from the SLIT with $x_0 = 170$ μm . The color of the data point represents the drive RF frequency used, ranging over 16.0-25.0 MHz. There are several trends that emerge from this plot. The first is that the conversion efficiency and pseudopotential well depth across the entire data set are not highly correlated. Instead, each trap size has a distinct group of data points. Both data sets appear linear with the conversion efficiency higher for a given trap when the drive RF frequency, and thus pseudopotential well depth, is increased. Compared to the trap with $x_0 = 270$ μm (open circles), the smaller SLIT has a much lower calculated pseudopotential well depth at the frequencies used, but very comparable conversion efficiencies. This trend suggests that while

pseudopotential well depth does affect the conversion efficiency, drive RF frequency plays a more important role. One reason as discussed earlier is that higher drive frequencies can increase the ratio of periods of drive RF to collisions between ion and neutrals, improving the fidelity of the secular motion. This enhanced definition of secular motion leads to increased acceleration due to the improved resonance between supplemental AC and secular ion motion. Alternatively, faster drive frequencies may also be able to capture a higher percentage of fragment ions simply by changing phases fast enough to trap ions further away from the center of the trap.

The parameters of both ion trap size and drive RF frequency are shown to impact the maximum CID efficiency, in the same direction as expected. At the same drive RF frequency, larger traps demonstrated higher fragmentation efficiencies, but higher drive RF frequencies for the same size traps also increased fragmentation efficiencies. If the conversion efficiency were limited solely by the pseudopotential well depth, all six points on this plot would be expected to appear along the same trend line. Instead, the different clusters demonstrate that the pseudopotential well depth cannot account for all of the gains in efficiency from the higher drive RF frequency.

4.2.2 Role of Pressure

The operating pressure for HPMS (1 Torr) is several orders of magnitude higher than that in conventional ion trap mass spectrometry (1 mTorr). With the increase in neutral buffer gas molecules present, the resulting increase in ion-neutral collisions is likely to have significant effects on the behavior of trapped ions, especially during CID. One such effect is the dispersal of the secular motion based on drive RF. The fidelity of secular ion motion is governed in part by the number of periods of drive RF per collision between ion and buffer gas.²³ With more

collisions, the secular behavior is less well-defined, leading to a reduction in the resonant characteristics used to induce resonant excitation. With less resonant overlap, more supplemental AC potential would be required to cause ion acceleration. Additionally, collisions between trapped ions and neutral buffer gas molecules play a significant role in ion cooling where ions which have excused far from the center of the trap may lose kinetic energy and be returned to stable trapping at the middle of the trap.²⁴ This collisional cooling could help trap fragment ions that would otherwise be lost.

Figure 4.4 shows a series of fragmentation heat maps of trichlorobenzene (molecular ion at m/z 180) at various pressures in a CIT with $r_0 = 500 \mu\text{m}$ and $\Omega \approx 7 \text{ MHz}$. Note that the trichlorobenzene is a byproduct of heating ($\sim 65 \text{ }^\circ\text{C}$) a sample of 1,3-dichlorobenzene. In panel A, the operating pressure is 500 mTorr of air and fragments at m/z 110 and 145 are produced as the result of successive chlorine atom losses. The lower intensity peaks present in the plot ($\sim m/z$ 130, 165) appear to be unidentified adducts. The similar appearance voltages (~ 4 and $5 V_{\text{P-P}}$ respectively) for these peaks as compared to the identified ions suggests that they are well bonded adducts. Given their apparent mass shifts, either oxygen (+16) or water (+18) would provide suitable explanations. The isolated precursor ion (m/z 180) is observed to be completely eliminated by $\sim 5 V_{\text{P-P}}$ supplemental AC due to the combination of resonant ejection and fragmentation. The ion fragment at m/z 145 develops at $\sim 4 V_{\text{P-P}}$ and completely ejects at $\sim 8 V_{\text{P-P}}$ supplemental AC, maximizing at $\sim 5.8 V_{\text{P-P}}$ with $\sim 93\%$ of precursor ion intensity. The ion fragment at m/z 110 develops with $> \sim 7 V_{\text{P-P}}$ supplemental AC and appears to be tapering off by the $10 V_{\text{P-P}}$ maximum output of the signal generator.

In Figure 4.4B with 1 Torr of air buffer, the trichlorobenzene molecular ion (m/z 180) is preserved through $\sim 9 V_{\text{P-P}}$ supplemental AC. The fragment at m/z 145 does not develop until

$\sim 7 V_{P-P}$ is applied and completely ejects at $\sim 10 V_{P-P}$ supplemental AC, maximizing at $\sim 8 V_{P-P}$ with $\sim 65\%$ of the isolated precursor ion's intensity. The fragment at m/z 110 does not develop until $\sim 8 V_{P-P}$ supplemental AC is applied. Figure 4.4C shows the same system but at 1500 mTorr of air buffer gas. In this case, very little fragmentation is seen and the precursor ion remains trapped over the tested voltage range (Note: $10 V_{P-P}$ is the maximum output of the function generator used for supplemental AC). There is the beginning of fragmentation, seen by some signal at m/z 145 at just over 9V with a slight reduction of signal from the molecular ion at m/z 180.

From the series of heat maps in Figure 4.4, it was observed that pressure clearly plays a role in fragmentation efficiency. Qualitatively, based on the voltage where each fragment appeared, it was observed that more voltage is required to induce fragmentation as the pressure increases. Figure 4.5A quantifies this through a survival yield plot for the trichlorobenzene precursor ion (m/z 180) over pressures spanning 250 mTorr to 1500 mTorr. With all other conditions held constant, the precursor ion is diminished by 50% with only around $3 V_{P-P}$ supplemental AC at 250 mTorr, but at 1250 mTorr the same reduction requires close to $9 V_{P-P}$. The monotonic trend shows that as pressure increases, it requires more voltage to cause the same total amount of fragmentation and/or ejection. A representation of this trend is shown in Figure 4.5B using the 50% survival rate excitation voltage for each pressure. This effect may be caused by several factors. First, the increased number of collisions on an average trip between the center and edge of the trap may cause fewer ions to be lost to resonant ejection before fragmenting. Second, the increased number of collisions per periodic motion may be disrupting the resonant behavior, dampening the acceleration of the ions. This second factor can be overcome by a

stronger field of supplemental AC, inducing the same amount of acceleration despite the weakening of the resonant characteristics.

The complement of the survival rate for the precursor ion is the conversion efficiency of the precursor ion into fragment ions. Figure 4.6 shows the appearance curves at various pressures of the ion at m/z 145 that corresponds to a loss of chlorine from trichlorobenzene. The general trend is at lower pressures, lower excitation voltages are needed to produce the ion. In this case, the ion is present at 250 mTorr with no excitation voltage applied while it takes over 8 V_{P-P} before a significant peak occurs at 1500 mTorr. The conversion efficiency also increases with pressure over the range explored. The maximum conversion efficiency at 250 mTorr is slightly below 25% by integrated peak intensity. At 500 mTorr and 1 Torr, however, conversion efficiencies of around 40% (by integrated peak intensity) are achieved. At 1500 mTorr, the maximum efficiency is not reached within the 10-volt output limit of the function generator. The phenomenon of improved conversion efficiency with higher pressures is likely a result of the increased number of collisions between the center and edge of the trap, causing two major effects. First, precursor ions tend to collide with a neutral closer to the center of the trap, preventing them from exiting the trapping boundaries before fragmentation. Second, newly formed fragment ions, even near the edges of the trap, are more efficiently cooled to the center of the trap.

As can be seen most readily at 250 mTorr (black squares) in Figure 4.6, there appear to be two local maxima (near 3 and 5.5 V) in regards to conversion efficiency as a function of excitation voltage. This may also be seen somewhat at 500 mTorr (blue circles) with maxima near 4.6 and 5.6 V. This could be the result of structural isomers, each of which have the same mass-to-charge ratio, but different energies of activation to undergo fragmentation. In this case,

since the trichlorobenzene precursor ion was formed by the addition of chlorine to 1,3-dichlorobenzene, there is likely a mixture of 1,2,3-trichlorobenzene and 1,3,4-trichlorobenzene present and thus two activation energies. No 1,3,5-trichlorobenzene is likely to be present due to the directing chemistry of halogen substituents. This analysis is an example of how tandem mass spectrometry can be used beyond the simple analysis of mass-to-charge ratios.

Figure 4.7 shows the appearance curve of the ion at m/z 110 at various pressures. At 250 mTorr, the fragment is continuously present at low concentrations though a maximum appears to be between ~ 6 and $7 V_{P-P}$ supplemental AC. At 500 mTorr, there are significantly more fragment ions present, maximizing at $\sim 9 V_{P-P}$. At 1000 mTorr, increased fragmentation occurs at increased voltages, but it is unclear if a maximum is achieved before the $10 V_{P-P}$ limit of the power supply is reached. At 1500 mTorr, there is no fragmentation induced over this voltage range. These trends are generally the same as those with the appearance of the m/z 145 ion: as pressure increases, the voltage required to induce fragmentation increases and the maximum conversion efficiency improves.

The findings of these experiments are consistent with expectations. As pressure increases, the collisions between trapped ions and neutral buffer gas molecules seem to disrupt the secular motion of the ions, reducing resonant behavior. Alternatively, the increased pressure corresponds to a lower mean free path, meaning less time for acceleration of the ion, resulting in less kinetic energy available per collision to convert into internal energy. Thus, higher voltages can accelerate the ions more quickly between collisions, overcoming the increase in pressure. The larger number of collisions at higher pressures also appear to enhance the effects of ion cooling,

increasing the number of fragment ions successfully trapped. This effect improves the maximum CID efficiencies observed at higher pressures.

4.2.3 Role of Buffer Gas

It is also known that the nature, in addition to number, of ion-neutral collisions can have significant impact on CID behavior. There are relevant differences between the air molecules used in HPMS and the helium atoms in conventional operation, starting with the mass of the species. The mass of the neutral buffer gas is extremely important in governing the amount of energy involved in a collision in the center-of-mass reference.²⁵ Higher mass of the neutral corresponds to higher kinetic energies involved in the collision. Mechanics, such as elasticity, of the collision are also relevant in the amount of kinetic energy converted into internal energy.²⁶ In highly elastic collisions, kinetic energy is largely conserved. In highly inelastic collisions, however, significant amounts of kinetic energy can be transferred into other modes, such as vibrational energy. A correlation between elasticity and polarizability has been described previously.²⁷ It was determined that in a collision between highly polarizable species, a long-lived collisional complex is formed, leading to more efficient transformation of kinetic energy to internal energy.

Helium is the usual buffer gas used in mass spectrometry at low pressures. Helium, as seen in Table 4.1, is both very small and not very polarizable when compared to nitrogen and oxygen, the primary components in air which is the preferred buffer gas for HPMS. This means that each collisional event in helium will have relatively lower amounts of kinetic energy and also a relatively lower percentage of energy transfer. Therefore, the rate of energy deposition, as well as the total amount of energy deposited without resonant ejection, are likely to be higher in

air. In comparison, argon, which is also shown in the table, is commonly used as a collision gas for CID in triple quadrupole experiments because of its larger size and higher polarizability.²⁸ There have also been instances of injecting heavy gases into ion traps in order to improve fragmentation efficiency.^{29, 30}

Figure 4.8 shows two heat maps of intensity across mass-to-charge and excitation amplitude for N,N-dimethylaniline with helium and air buffer gases. In panel A, the operating pressure was 2 Torr of helium buffer gas. This result can be contrasted with panel B, which shows the fragmentation pattern of N,N-dimethylaniline in 1 Torr of air buffer gas, but the same conditions otherwise. This demonstrates the importance of buffer gas identity for CID. In panel A, even with 2 Torr of helium, no significant fragmentation of N,N-dimethylaniline was seen before complete resonant ejection occurred, with around 9 V_{p-p} of supplemental AC. Even at such a high pressure, which should aid fragmentation based on Section 4.2.2 of this work, all precursor ions were shown to overcome the trapping potentials before fragmenting. In only 1 Torr of air, however, a significant amount of fragmentation is observed in panel B, indicated by the points at m/z 77, 91, and 106 with 4-7 V_{p-p} of supplemental AC potential. Because of the larger average mass of air buffer gas molecules, there is a significantly larger amount of center-of-mass energy available in each ion-neutral collision. Furthermore, due to the increased polarizability of the oxygen and nitrogen gas molecules, the collisions were also more inelastic and converted more of that kinetic energy into internal and inducing fragmentation.

This trend of enhanced fragmentation with more massive, more polarizable neutral buffer gas molecules follows expectations from theory. Furthermore, HPMS uses air as the preferred buffer gas rather than helium primarily due to portability concerns. The use of air as a buffer gas

does cause a loss in resolution, but the improvement in fragmentation efficiency aids greatly in the recovery of instrument selectivity.

4.3 Gas Chromatography – High Pressure Mass Spectrometry

The coupling of separations techniques with mass spectrometry has been used to improve selectivity and make possible the analysis of complex mixtures in many fields, from proteomics³¹ to food monitoring.³² Gas chromatography has already been established as a suitable technique for miniaturization and exists in portable forms.¹¹⁻¹³ Using a mass spectrometer with a GC in the field can further enhance selectivity and identification of target analytes. Typical field GC instrumentation is designed to operate separations on the time scale of a few minutes with flow rates at a few standard cubic centimeters per minute (sccm). The time scale of a single HPMS mass spectrum is on the order of 10 milliseconds, appropriately fast enough to provide ample averaging and peak sampling over a GC peak that may only be a second or so broad. The pumps in HPMS systems are also capable of handling a gas load of a few sccm. Gas chromatography, therefore, is a promising partner for HPMS devices in harsh environments.

The possibility of using a high pressure MS as a detector for GC was investigated by coupling an HPMS to an Agilent 7890 GC. Although the 7890 is a laboratory-based instrument, the separation conditions used were similar to those typically used in portable instruments, serving as a suitable stand-in for a portable instrument. The 7890 has dual column capability and a 15-meter long Rxi-5ms (Crossbond 5% diphenyl/95% dimethylpolysiloxane) stationary phase column was connected to each injector port. One column was connected to the integrated flame ionization detector (FID) of the GC while the other column was coupled through the oven wall to the heated inlet of a fully integrated HPMS system (908 Devices) with a Faraday cup detector.

The results were collected by software provided by 908 Devices as a series of mass spectra. Signal intensity as calculated by this software is normalized and plotted over time to create a chromatogram.

The following separations were performed with flow rates of 2.0 sccm through the analytical columns. Injection volume was 1.0 μL into a 40/1 split to waste. The temperature in the oven was constant at 40 $^{\circ}\text{C}$ for the first 30 s of the scan, followed by a ramp of 20 $^{\circ}\text{C}/\text{min}$ up to 150 $^{\circ}\text{C}$. The test mixture was a selection of chemical warfare agent simulants (CWASs). Pure samples of dimethyl methylphosphonate, chloroethyl ethyl sulfide, diethyl methylphosphonate, diethyl malonate, triethyl phosphate, and methyl salicylate were each added in 10 μL aliquots to 1 mL of mixed hexanes solvent.

Figure 4.9 depicts two chromatograms of the same sample described above, using helium as the carrier gas. The top trace is signal from the FID, and the bottom trace is the calculated signal from the HPMS detector. Peak identification was made by a combination of mass spectral data and the comparison of retention times to injections of standards. The first, unlabeled peaks around 1 min correspond to solvent. The order of elution was: 1, dimethyl methylphosphonate; 2, chloroethyl ethyl sulfide; 3, diethyl methylphosphonate; 4, diethyl malonate; 5, triethyl phosphate; 6, methyl salicylate. Triethyl phosphate was detected by FID, but not by HPMS. An injection of triethyl phosphate standard solution was also not detected by HPMS. Likely, the conditions used by the mass spectrometer were simply inappropriate for trapping that particular compound. There is a slight shift to longer retention times from the FID chromatogram to the HPMS chromatogram. This is probably the result of different amounts of time between injection and data accumulation with the different detectors and slightly different column lengths. Peak heights are varied due to the different response factors of the detectors. FID

response factor is primarily a function of carbon concentration, so the number of carbons per molecule affects peak heights. HPMS response factor, on the other hand, is primarily a function of ionization efficiency. With HPMS detection, peak 3 is seen to have a tailing feature which is likely the result of insufficient heating of the transfer line or mass spectrometry chamber, causing temporary adsorption of the analyte.

Helium is a standard carrier gas for GC, however, it would require a compressed gas cylinder if used in the field. This would not only increase the size and weight of the instrument but also limit the potential useable lifetime of the instrument depending on the cylinder size. Nitrogen is an attractive alternative as a carrier gas as it can be generated readily from air, though at the cost of increased power consumption. Figure 4.10 shows the same CWAS mixture separation with nitrogen as the carrier gas. Elution order was preserved and all components, including triethyl phosphate (5), were successfully detected via HPMS. Retention times may be slightly shifted based on the time between injection and data accumulation. Due to the mass spectral broadening of peaks using nitrogen rather than helium, the signal to noise ratio in that domain was reduced, causing diminished calculated intensity, and therefore inferior peak shape in the chromatographic domain as well.

This mixture represents a selection of species that simulate dangerous chemical warfare agents, spanning several classes and therefore requiring different response protocols. The ability to quickly differentiate them is paramount to enacting the correct defensive actions and would not have been possible without this separation technique. While mixtures in the field are likely to be comprised of components other than CWA threats and solvents, these compounds are also likely to be far more chemically diverse and more easily separated on a GC. The successful

coupling of a GC with its separation powers with chemical identification powers of the HPMS expands the usefulness of the HPMS system.

4.4 Conclusions

Selectivity is a defining attribute of a successful instrument in the field of rapid threat detection. Although HPMS has the inherent advantage of relying on the selective technique measuring mass-to-charge ratios, high pressures have been known to degrade resolution and selectivity. In this chapter, it was demonstrated that CID could be tuned for high efficiency fragmentation and that gas chromatography could be readily coupled to HPMS. Both of these techniques serve to enhance the instrumental selectivity.

The efficiency of CID was shown to rely on key variables including ion trap size, drive RF frequency, neutral buffer gas pressure, and neutral buffer gas identity. Reducing ion trap size at a constant q_z reduces the pseudopotential well depth, lowering CID efficiency. As predicted, increasing drive RF frequency raises CID efficiency, but does so by more than expected from pseudopotential well depth calculations alone. Higher neutral buffer gas pressures were shown to aid CID efficiency. The use of air, rather than helium, was also shown to be beneficial to inducing fragmentation with high efficiency. Gas chromatography was shown to be a compatible technique with HPMS. The successful coupling was demonstrated, and separations of chemical warfare agent simulants were shown using both helium and nitrogen as carrier gases.

Further improvements in several of these factors could further aid in instrumental selectivity. Higher drive RF frequencies have been shown to improve resolution at a constant pressure or enable analysis at higher pressures. This trend may also aid CID conversion

efficiencies. Miniaturization of the gas chromatography system can also be investigated, preparing the integrated to device for use in field situations.

4.5 Tables & Figures

	He	N ₂	O ₂	Ar
Mass (amu)	4.002	28.01	32.00	39.95
Polarizability (10 ⁻²⁴ cm ³)	0.205	1.740	1.581	1.641

Table 4.1. Table showing masses and polarizabilities of common buffer gases for CID.³³

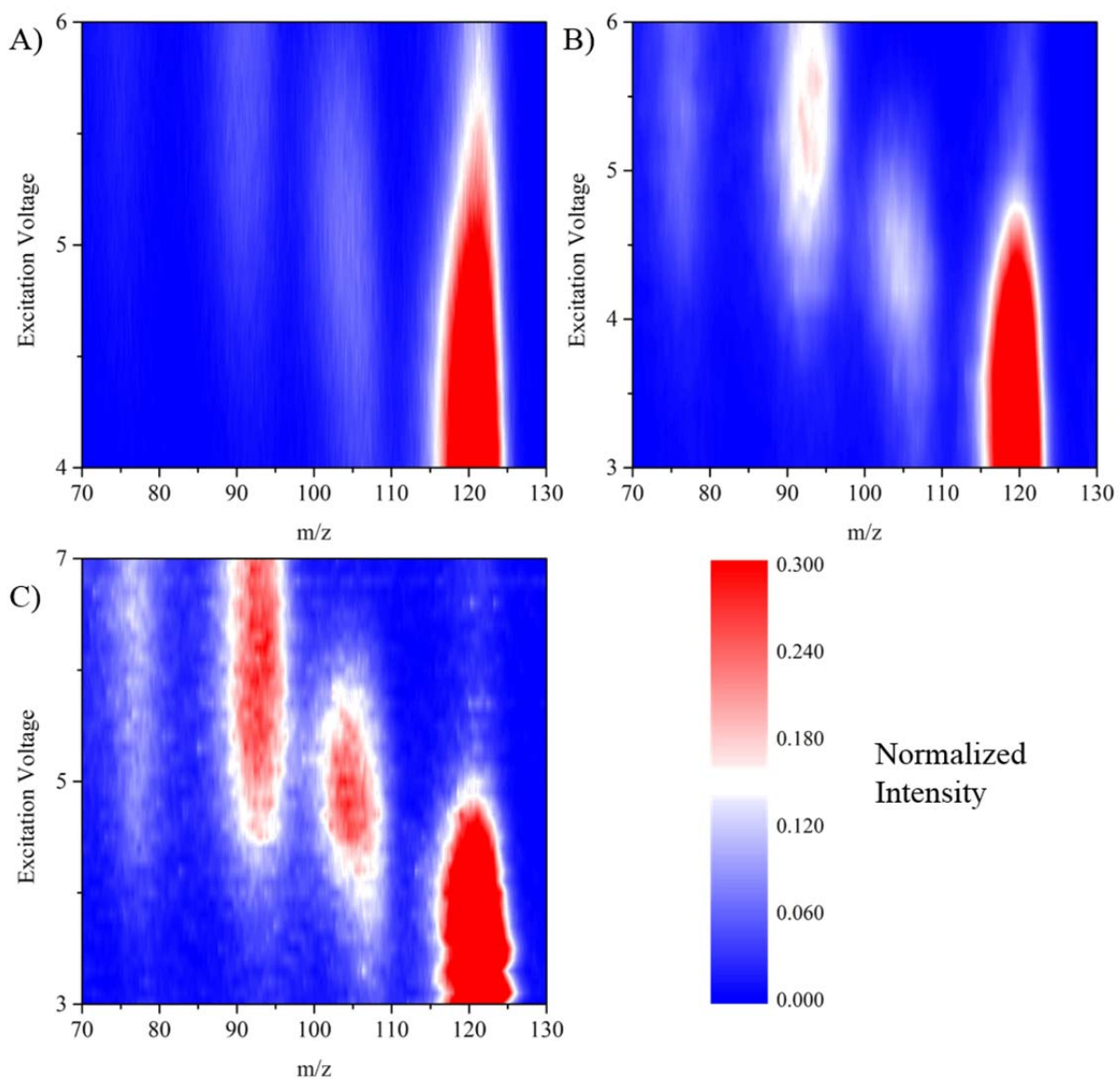


Figure 4.1. Fragmentation heat map patterns for N,N-dimethylaniline in 1 Torr air in SLIT with $x_0 = 270 \mu\text{m}$, $y_0 = 5 \text{ mm}$ and varying drive RF frequencies. The molecular ion at m/z 121 dissociates into fragments at m/z 77, 91, and 106. In all cases, excitation is performed with the precursor ion at $q_z = 0.4$. The drive frequencies are as follows: A) $\Omega = 16.4 \text{ MHz}$ B) $\Omega = 19.1 \text{ MHz}$ C) $\Omega = 20.9 \text{ MHz}$.

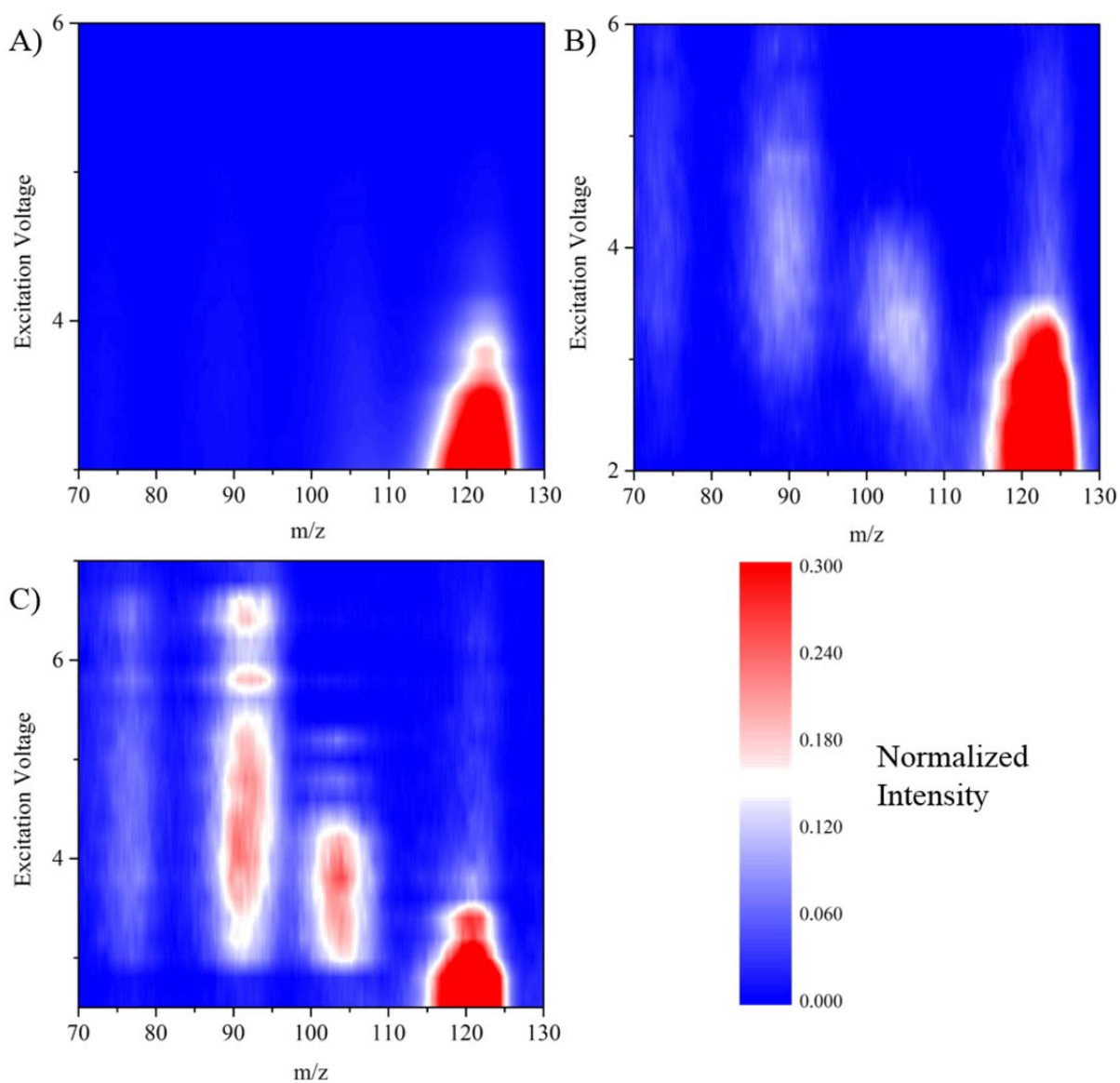


Figure 4.2. Fragmentation heat map patterns for N,N-dimethylaniline in 1 Torr air in SLIT with $x_0 = 170 \mu\text{m}$, $y_0 = 5 \text{ mm}$ varying drive RF frequencies. The molecular ion at m/z 121 dissociates into fragments at m/z 77, 91, and 106. In all cases, excitation is performed with the precursor ion at $q_z = 0.4$. The drive frequency is as follows: A) $\Omega = 19.1 \text{ MHz}$ B) $\Omega = 20.9 \text{ MHz}$ C) $\Omega = 25.0 \text{ MHz}$.

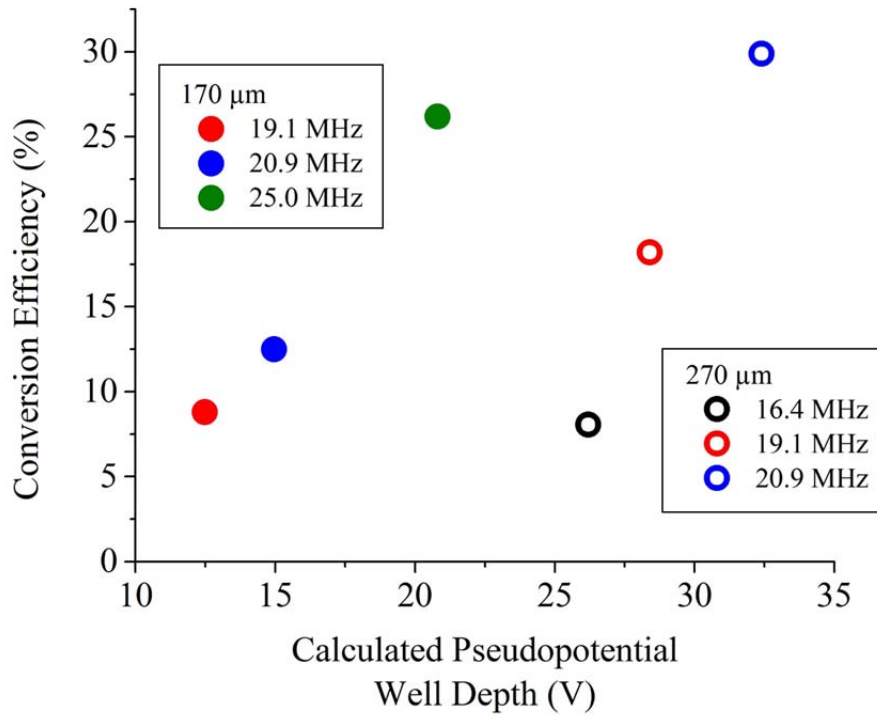


Figure 4.3. Plot showing conversion efficiency measured from Figures 4.1 and 4.2 against calculated pseudopotential well depths of the ions, which are activated with $q_z = 0.4$. Data points from the trap with $x_0 = 270 \mu\text{m}$ are shown in open circles while points from the trap with $x_0 = 170 \mu\text{m}$ are shown with closed circles. The frequency at each data point is shown by the color of the point, ranging from 16.4 MHz (black) to 25.0 MHz (green).

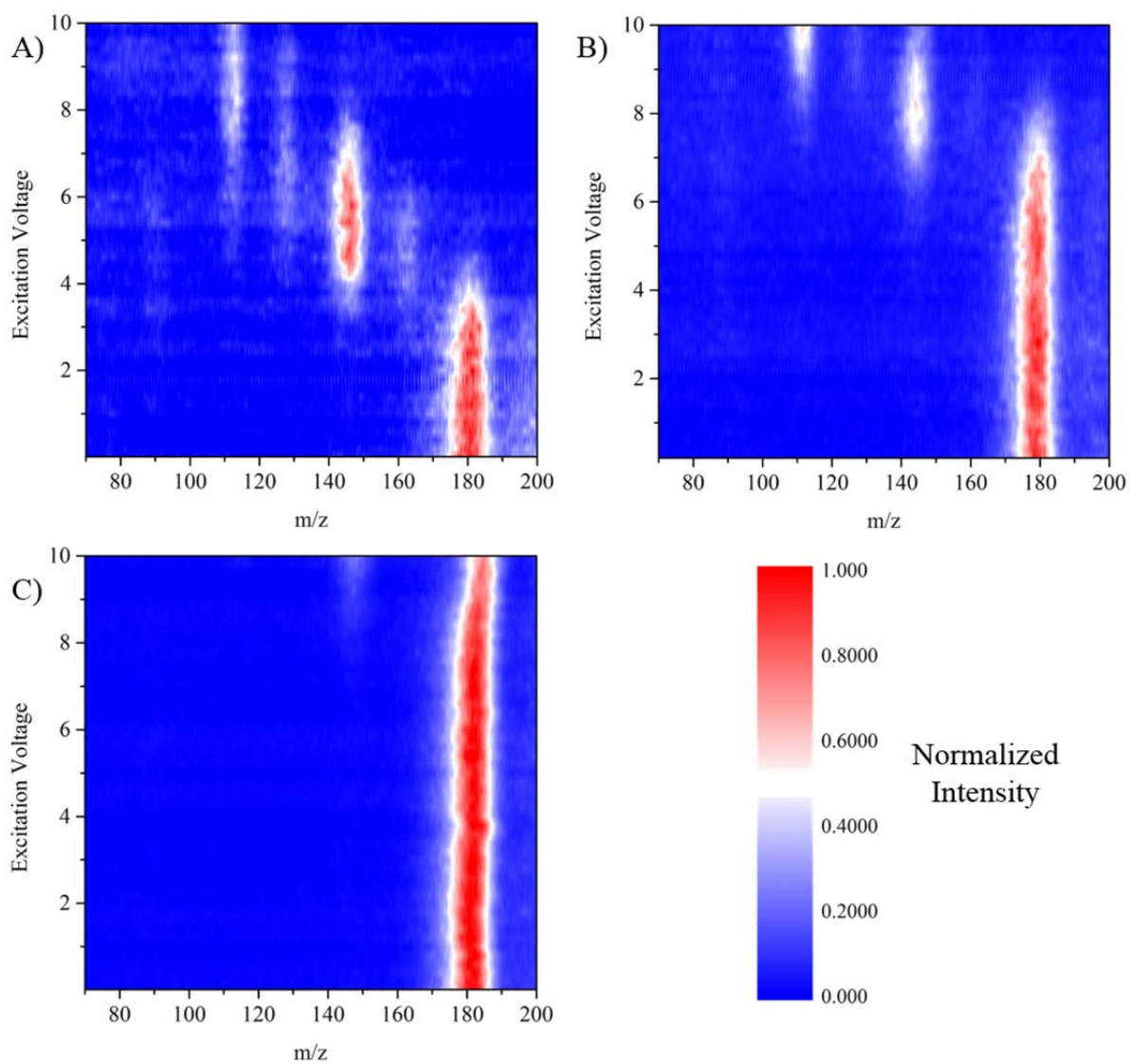


Figure 4.4. Fragmentation heat maps showing trichlorobenzene at different pressures in a CIT with $r_0 = 500 \mu\text{m}$. Losses of chlorine leads to fragments at m/z 110 and 145. The buffer gas pressure is A) 500 mTorr B) 1000 mTorr C) 1500 mTorr air.

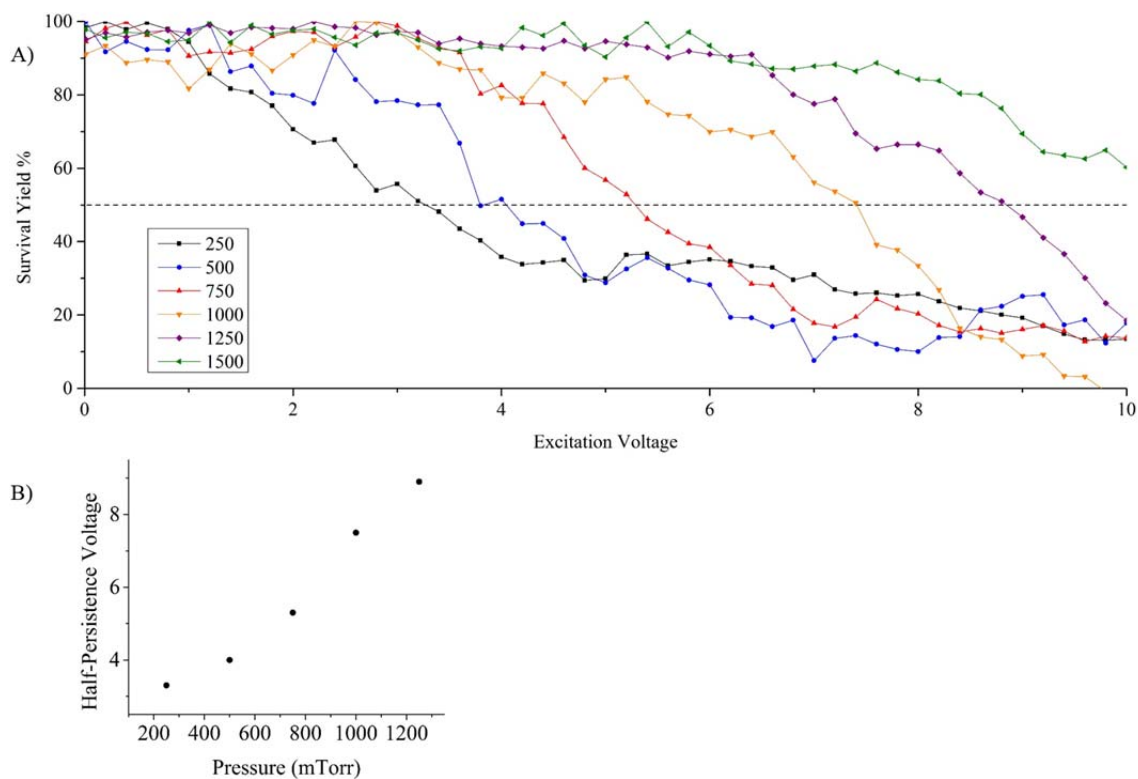


Figure 4.5. A) Plot showing the survival yield of the trichlorobenzene precursor ion at m/z 180 at various supplemental AC voltages under various pressures. The horizontal dashed line shows the 50% survival rate for reference. B) Plot showing the half-persistence voltage, which is the excitation voltage at which half of the precursor ion still remains, for each pressure.

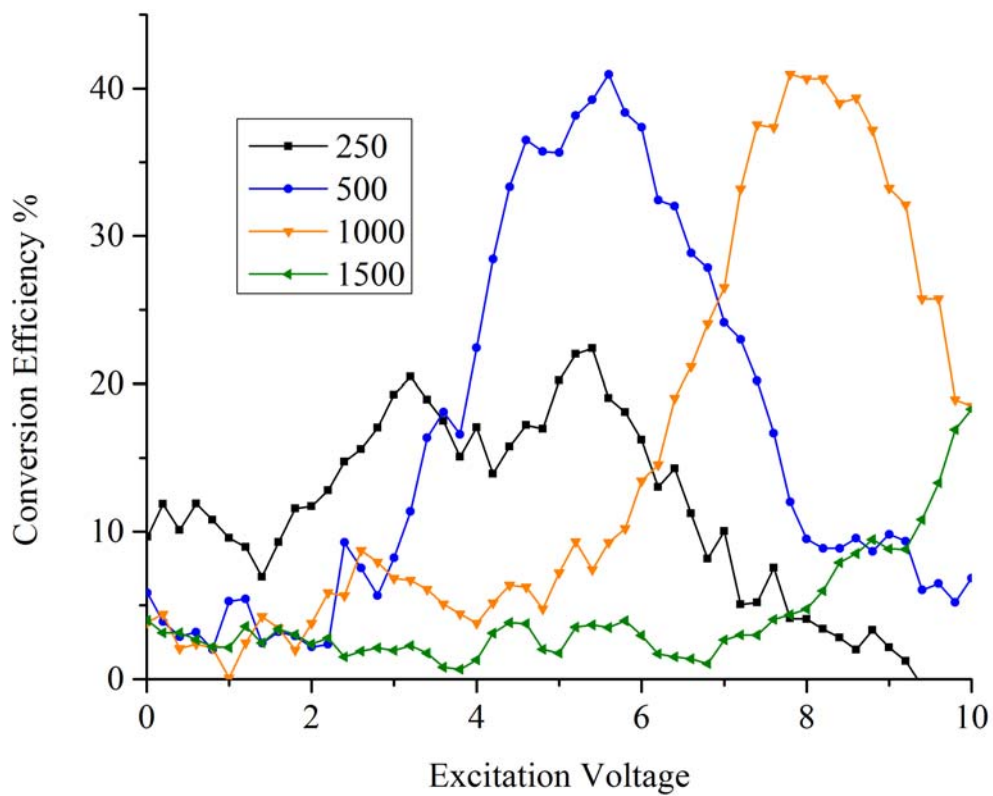


Figure 4.6. Appearance curve plot showing the conversion efficiency of the precursor ion into a fragment ion at m/z 145 at different supplemental AC excitation voltages under different pressures.

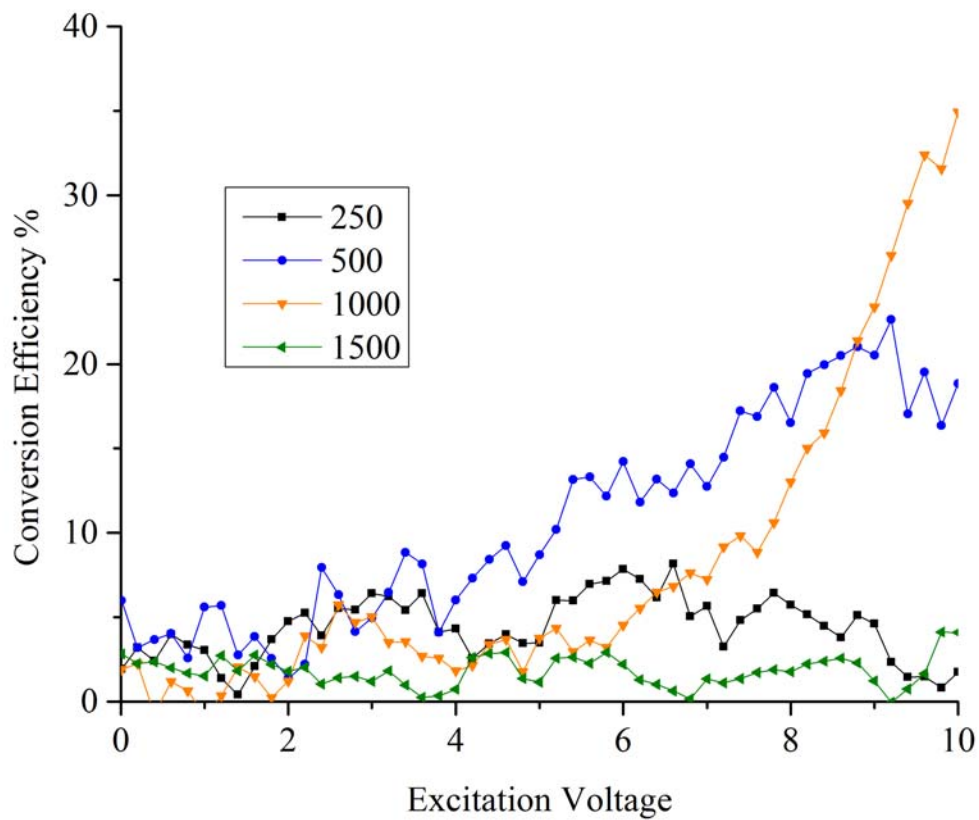


Figure 4.7. Appearance curve plot showing conversion efficiency of parent ion into the fragment ion at m/z 110 with supplemental AC excitation voltage under various pressures.

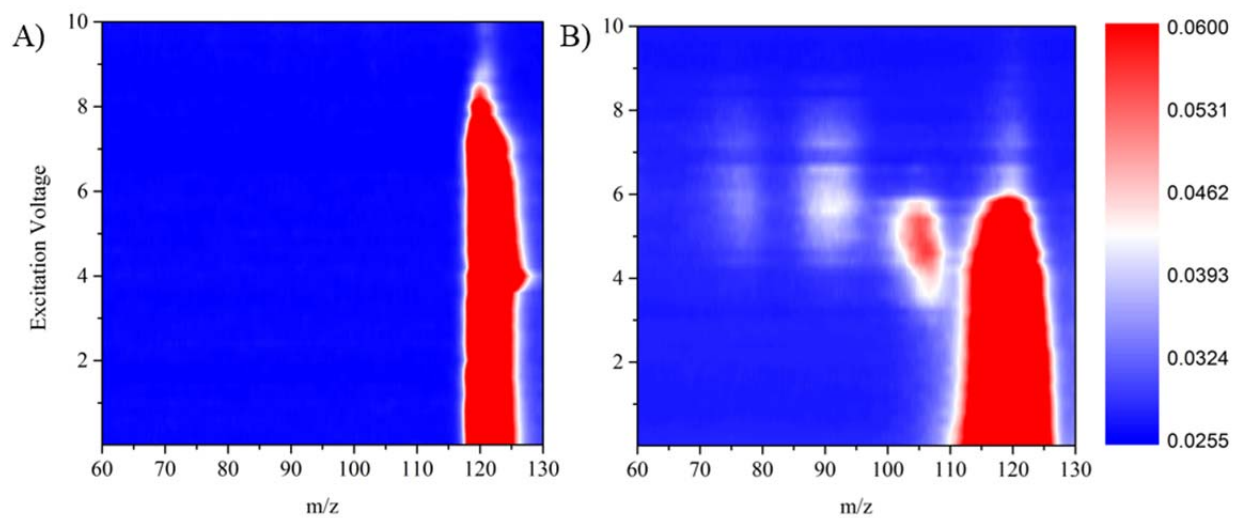


Figure 4.8. Fragmentation heat maps of N,N-dimethylaniline (molecular ion m/z 121) with different buffer gases. Panel A shows the lack of fragmentation with 2 Torr helium buffer gas. Panel B shows ready fragmentation (fragment ions at m/z 77, 91, 106) with 1 Torr air buffer gas.

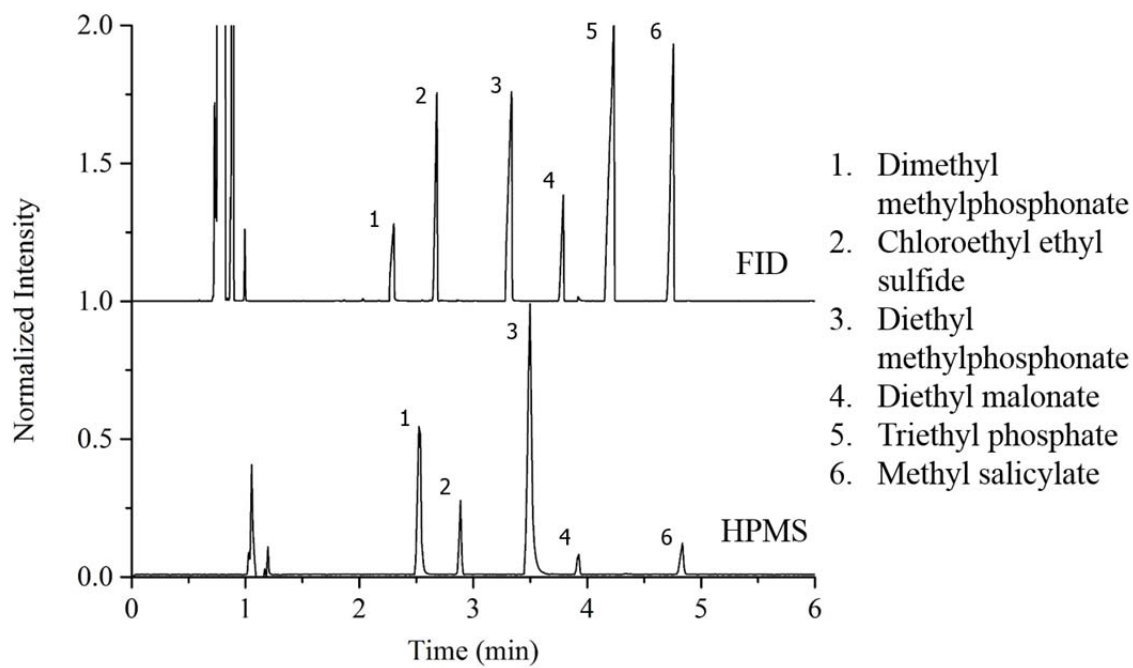


Figure 4.9. Chromatogram of a mixture of chemical warfare agent simulants detected by FID and by HPMS with helium carrier gas.

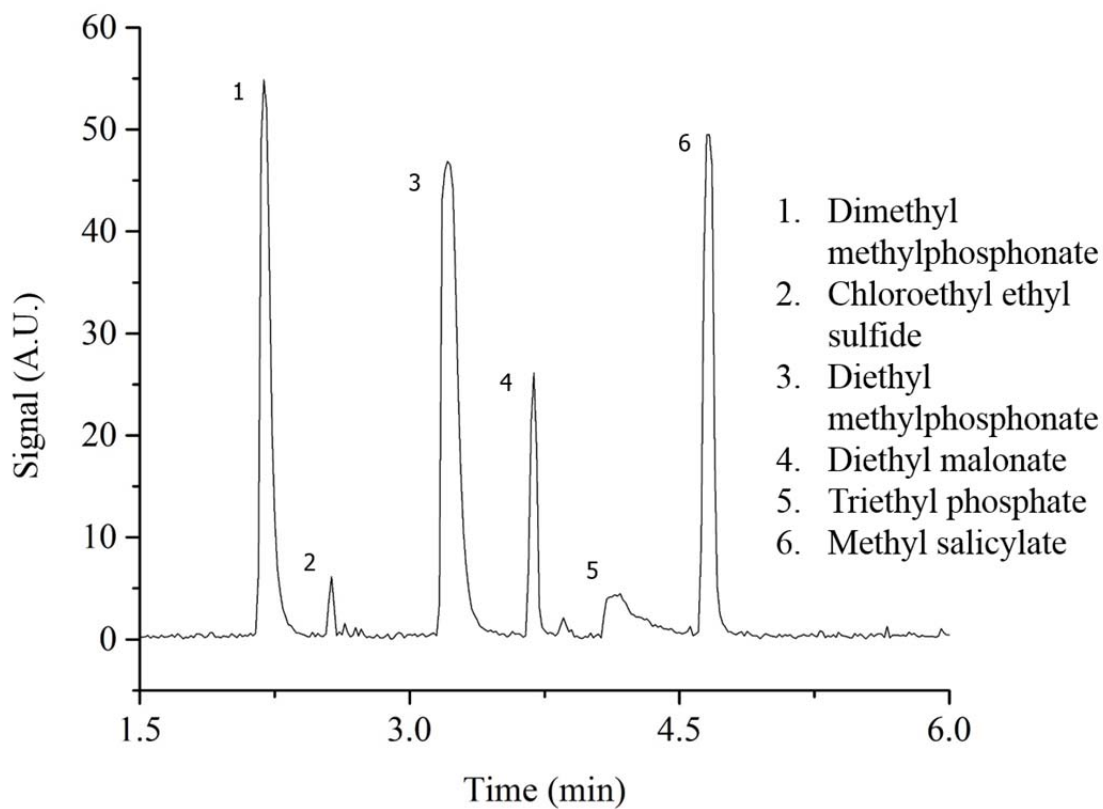


Figure 4.10. Chromatogram of a mixture of chemical warfare agent simulants by HPMS using nitrogen carrier gas.

4.6 REFERENCES

1. Blakeman, K.H., et al., *High pressure mass spectrometry of volatile organic compounds with ambient air buffer gas*. *Rapid Communications in Mass Spectrometry*, 2017. **31**(1): p. 27-32.
2. Blakeman, K.H., et al., *High Pressure Mass Spectrometry: The Generation of Mass Spectra at Operating Pressures Exceeding 1 Torr in a Microscale Cylindrical Ion Trap*. *Analytical Chemistry*, 2016. **88**(10): p. 5378-5384.
3. Burnworth, M., S.J. Rowan, and C. Weder, *Fluorescent Sensors for the Detection of Chemical Warfare Agents*. *Chemistry – A European Journal*, 2007. **13**(28): p. 7828-7836.
4. Contreras, J.A., et al., *Hand-Portable Gas Chromatograph-Toroidal Ion Trap Mass Spectrometer (GC-TMS) for Detection of Hazardous Compounds*. *Journal of the American Society for Mass Spectrometry*, 2008. **19**(10): p. 1425-1434.
5. Mayhew, C.A., et al., *Applications of proton transfer reaction time-of-flight mass spectrometry for the sensitive and rapid real-time detection of solid high explosives*. *International Journal of Mass Spectrometry*, 2010. **289**(1): p. 58-63.
6. Hsu, C.S., et al., *Petroleomics: advanced molecular probe for petroleum heavy ends*. *Journal of Mass Spectrometry*, 2011. **46**(4): p. 337-343.
7. Houel, S., et al., *Quantifying the Impact of Chimera MS/MS Spectra on Peptide Identification in Large-Scale Proteomics Studies*. *Journal of Proteome Research*, 2010. **9**(8): p. 4152-4160.
8. Waridel, P., et al., *Evaluation of quadrupole time-of-flight tandem mass spectrometry and ion-trap multiple-stage mass spectrometry for the differentiation of C-glycosidic flavonoid isomers*. *Journal of Chromatography A*, 2001. **926**(1): p. 29-41.
9. Ferreres, F., R. Llorach, and A. Gil-Izquierdo, *Characterization of the interglycosidic linkage in di-, tri-, tetra- and pentaglycosylated flavonoids and differentiation of positional isomers by liquid chromatography/electrospray ionization tandem mass spectrometry*. *Journal of Mass Spectrometry*, 2004. **39**(3): p. 312-321.
10. Kushnir, M.M., et al., *Assessing analytical specificity in quantitative analysis using tandem mass spectrometry*. *Clinical Biochemistry*, 2005. **38**(4): p. 319-327.

11. Defiant, <http://www.defiant-tech.com/frog-4000.php>. Accessed November 2016.
12. Defiant, <http://www.defiant-tech.com/canarythree.php>. Accessed November 2016.
13. Calidus, <http://www.falconfast.net/calidus-and-enhancements/calidus-gc>. Accessed November 2016.
14. Eckenrode, B.A., *The application of an integrated multifunctional field-portable GC/MS system*. Field Analytical Chemistry & Technology, 1998. **2**(1): p. 3-20.
15. Meuzelaar, H.L.C., et al., *Advances in field-portable mobile GC/MS instrumentation*. Field Analytical Chemistry & Technology, 2000. **4**(1): p. 3-13.
16. Thomson, B.A., et al., *Improved Collisionally Activated Dissociation Efficiency and Mass Resolution on a Triple Quadrupole Mass Spectrometer System*. Analytical Chemistry, 1995. **67**(10): p. 1696-1704.
17. Ekroos, K., et al., *Charting molecular composition of phosphatidylcholines by fatty acid scanning and ion trap MS3 fragmentation*. Journal of lipid research, 2003. **44**(11): p. 2181-2192.
18. Dehmelt, H., *Radiofrequency spectroscopy of stored ions I: Storage*. Advances in Atomic and Molecular Physics, 1967. **3**: p. 53-72.
19. Stafford, G., *Ion trap mass spectrometry: a personal perspective*. Journal of the American Society for Mass spectrometry, 2002. **13**(6): p. 589-596.
20. Stafford Jr, G.C., et al., *Recent improvements in and analytical applications of advanced ion trap technology*. Int. J. Mass Spectrom. Ion Processes, 1984. **60**(1): p. 85-98.
21. March, R.E., *An Introduction to Quadrupole Ion Trap Mass Spectrometry*. J. Mass Spectrom., 1997. **32**(4): p. 351-369.
22. Charles, M.J., S.A. McLuckey, and G.L. Glush, *Competition between resonance ejection and ion dissociation during resonant excitation in a quadrupole ion trap*. Journal of the American Society for Mass Spectrometry, 1994. **5**(12): p. 1031-1041.
23. Whitten, W.B., P.T. Reilly, and J.M. Ramsey, *High-pressure ion trap mass spectrometry*. Rapid Commun. Mass Spectrom., 2004. **18**(15): p. 1749-52.

24. Hager, J.W., *A new linear ion trap mass spectrometer*. Rapid Communications in Mass Spectrometry, 2002. **16**(6): p. 512-526.
25. Mitchell Wells, J. and S.A. McLuckey, *Collision-Induced Dissociation (CID) of Peptides and Proteins*, in *Methods in Enzymology*. 2005, Academic Press. p. 148-185.
26. Vachet, R.W. and G.L. Glish, *Effects of heavy gases on the tandem mass spectra of peptide ions in the quadrupole ion trap*. Journal of the American Society for Mass Spectrometry, 1996. **7**(12): p. 1194-1202.
27. McLuckey, S.A., *Principles of collisional activation in analytical mass spectrometry*. Journal of the American Society for Mass Spectrometry, 1992. **3**(6): p. 599-614.
28. Dawson, P.H., *The collision-induced dissociation of protonated water clusters studied using a triple quadrupole*. International Journal of Mass Spectrometry and Ion Physics, 1982. **43**(2): p. 195-209.
29. Doroshenko, V.M. and R.J. Cotter, *Pulsed Gas Introduction for Increasing Peptide CID Efficiency in a MALDI/Quadrupole Ion Trap Mass Spectrometer*. Analytical Chemistry, 1996. **68**(3): p. 463-472.
30. Morand, K.L., K.A. Cox, and R.G. Cooks, *Efficient trapping and collision-induced dissociation of high-mass cluster ions using mixed target gases in the quadrupole ion trap*. Rapid Communications in Mass Spectrometry, 1992. **6**(8): p. 520-523.
31. Prasad, B., et al., *Ontogeny of Hepatic Drug Transporters as Quantified by LC-MS/MS Proteomics*. Clinical Pharmacology & Therapeutics, 2016. **100**(4): p. 362-370.
32. Shamsipur, M., N. Yazdanfar, and M. Ghambarian, *Combination of solid-phase extraction with dispersive liquid-liquid microextraction followed by GC-MS for determination of pesticide residues from water, milk, honey and fruit juice*. Food Chemistry, 2016. **204**: p. 289-297.
33. Haynes, W.M., *CRC handbook of chemistry and physics*. 2014: CRC press.

Chapter 5: Conclusions and Future Directions

5.1 Conclusions

Mass spectrometry (MS) is an inherently selective technique due to its ability to measure the mass-to-charge ratio of analytes and, as a result, has led to the development of fieldable and hand portable mass spectrometers. Selectivity is an important characteristic of these devices for rapid threat detection where false positives can be tactically costly and cause loss of trust in the instrument. High pressure mass spectrometers (HPMS) operate at ≥ 1 Torr and are suitable for portable use.^{1,2} There is a degradation of resolution due to the pressure, however, causing more species to appear isobaric. Two major strategies for enhancing the selectivity of HPMS were investigated in this work: tandem mass spectrometry and coupling a separation step (gas chromatography) to a HPMS. Tandem mass spectrometry is a common strategy to enhance chemical information about compound structure in low pressure ion traps. It is also a promising technique for portable devices as it can be implemented via collision-induced dissociation with no additional cost to the device's size, weight, or power (SWaP).³ Gas chromatography is another technique commonly used with benchtop mass spectrometry. It is useful in generating additional chemical information from retention times and is often necessary for analysis of complex mixtures.

Initial implementation of tandem mass spectrometry focused on understanding how trapped ions in HPMS systems with cylindrical ion trap (CIT) and stretched length ion trap (SLIT) geometries behave compared to ions trapped in low pressure, hyperbolic traps. This is of

importance as selectively isolating a precursor ion, exciting that ion, and analyzing it all require understanding its behavior within the ion trap. The initial experiments investigated stability diagrams that plot the parameter space between the RF drive voltage and the supplemental DC voltage applied to the ring electrode for trapping of ions. It was found there were minimal pressure effects on the stability region in a CIT between 500 and 1500 mTorr. The observed mass windows at these pressures, however, were extended well past those at 1 mTorr for both a CIT and a SLIT. Furthermore, the experimental and simulated stability regions demonstrated that SLITs were behaving as two-dimensional traps, unlocking valuable information about the behavior of the ions inside the trap. Analysis of resonant ejection behavior showed that resonant characteristics, especially double resonance, were greatly damped as the pressure of neutral buffer gas molecules increased. Resonant ejection was still effected at higher pressures but required higher voltages of supplemental AC. This trend is important for understanding how to resonantly excite for collision-induced dissociation at high pressures.

Current HPMS instrument orientation features a direct line of sight between the ionization source and the detector, either an electron multiplier or Faraday cup. Faraday detectors are ultimately the preferred detector for a portable instrument due to their ability to operate at high pressures. As the Faraday cup is a current integrating detector, the exposure to ions and/or electrons present during the ionization portion of the HPMS scan function can result in excessive charge build-up, causing a large background signal later in the scan function. Therefore, the ability to control ion transport within the trap was explored, such that spatially differentiating the regions of ion injection and ejection in a SLIT would eliminate the direct line of sight between detector and ionization source. This was investigated by manipulating the electric field of the trap either by using a tapered SLIT geometry or by adding supplemental electrodes with DC

potentials between the ring electrode and endcaps. The tapered SLIT ring electrode, when combined with a DC bias, created a small potential gradient along the length of the SLIT, causing ions to preferentially move to one side. Adding supplemental electrodes along the length of the SLIT, however, created a much stronger potential field gradient and improved ion control within the trap.

Targeted ion isolation is important for implementing tandem mass spectrometry such that fragmentation of only one species at a time is occurring. Three mass selective strategies were demonstrated here: apex isolation, multi-frequency excitation isolation, and partial instability scan isolation. Each was sufficient for isolating specific mass-to-charge species in the ion trap, with multi-frequency excitation being the most effective while partial instability scans were the easiest to implement. The isolation techniques set the stage for the last studied form of ion manipulation: resonant excitation. Collision induced dissociation through resonant excitation was successfully implemented for the fragmentation of various precursor ions including bromobenzene, N,N-dimethylaniline, trichlorobenzene, tryptophan clusters, and the peptide RGEK. The extent of fragmentation was able to be controlled by the amplitude of the applied supplemental AC.

Achieving CID with a high conversion efficiency is critical for low-concentration analytes, such that the resulting fragments can be successfully detected and the maximum amount of chemical information obtained. Optimization of the fragmentation efficiency of CID was shown to be dependent on several variables. Smaller ion trap dimensions limited fragmentation efficiency, presumably due to a decrease in the pseudopotential well depth.⁴ Increasing the drive RF frequency is known to deepen the pseudopotential well when q_z is held constant (by increasing RF signal amplitude). While commensurate tradeoffs in size reduction

and drive RF frequency lead to an unchanged pseudopotential well depth, the increased drive frequency was found to overcompensate for smaller trap dimensions in terms of CID efficiency. Increasing buffer gas pressure also improved the maximum conversion efficiency by providing ample collisions to convert the ion's kinetic energy into internal energy. In addition, buffer gas identity played a role, as more massive and polarizable species were able to more efficiently deposit internal energy into a trapped ion.

Gas chromatography (GC) has been shown to be a valuable tool when connected to mass spectrometers as it provides additional chemical information based on retention time, and it simplifies resulting mass spectra. A commercial GC was coupled to a breadboard HPMS system to demonstrate the feasibility of a GC-HPMS system. Here, a mixture of six chemical warfare agent simulants, which could not be analyzed by HPMS alone, was successfully separated and detected with GC-HPMS.

These studies demonstrated that HPMS systems, which are portable, sensitive devices, can be enhanced by the implementation of tandem mass spectrometry and coupling to gas chromatography. Both of these techniques enhance the selectivity and limit false positive rates, while being appropriate for portable instrumentation with fast detection times.

5.2 Future Directions

The results in this work have helped improve the understanding of HPMS systems with respect to improving chemical identification, but in many cases there are continuation lines of study that could lead to even further understanding. There are further opportunities for characterization of trapped ions at high pressure with stability diagram and resonant behavior

analysis and for improvement of instrumental capabilities with maximizing CID efficiency, miniaturizing GC components, and advancing axial control of trapped ions in SLITs.

The primary focus of stability region investigation in these initial studies was pressure effects. These were measured in both SLIT and CIT at high (1 Torr) and low (1 mTorr) pressures but focused on only one size and geometry for each. Variations in trap geometry, such as spacer thickness and r_0/z_0 ratio, have recently been investigated as to their effect on resolution.⁵ These physical changes are known to change the electric field contributions within the trap and therefore the stability conditions. Thus, further investigation of the stability regions for different electrode designs and geometries and the possible higher order fields generated should provide information on how they impact trapped ions. These variations would manifest in differently shaped regions, possibly with areas of instability within the region.⁶

Another experimental parameter to explore is pressure using higher resolution increments than shown here. The work here shows the general pressure trends but finer pressure step sizes may reveal significant information about how ion-neutral collisions affect ion stability. This could be from ions either gradually overcoming pseudopotential well depths or having sufficiently disrupted secular motion resulting in measurable ion loss at a threshold value. Furthermore, although the drive RF frequency is expected to fundamentally govern the size and sharpness of the stability region, these effects have not been experimentally measured and are worth pursuing.

Increasing the drive RF frequency can improve resolution in HPMS devices. A tradeoff, however, is that to maintain low voltage and power requirements, a reduction in trap size, and thus ion capacity, is necessary. This diminished capacity severely affects low abundance or poorly detected ions where high fragmentation efficiency is needed to successfully detect the

resulting fragment ions. Thus, further improvements of CID in HPMS systems are highly desirable. As discussed in this work, decreased ion trap size and increased drive frequency have competing effects on the pseudopotential well depth. When compared to the original and still commonly used Finnigan ion trap design with $r_0 = 1.00$ cm, the experimental trap sizes investigated here were reduced by a factor of 20-60x. The pseudopotential well depth is expected to drop by the square of the reduction in trap size. The drive RF frequency enhancement, however, was only ~ 10 -25x, (improving the pseudopotential well depth by the square of this factor) meaning the calculated pseudopotential well depth is still significantly reduced resulting in an overall loss in sensitivity. Based on the data shown here, however, pushing to higher frequencies should provide a significant boon to CID conversion efficiencies, even if trap size is decreased as well. Experiments with a drive RF frequency of 60 MHz improved resolution⁷ and so when coupled with CID, should result in improved CID efficiency and resolution. Therefore, it would be beneficial to explore a greater range of trap sizes and drive RF frequencies.

In terms of improving the sensitivity of an HPMS system, it would be greatly beneficial to have differentiated regions for ion injection and ejection. This configuration would limit the number of background ions reaching the detector and improve the signal to noise. Results from incorporating supplemental electrodes between the ring electrode and end cap showed it is possible to preferentially accumulate ions in a region of interest. Expanding on this idea by increasing the number of supplemental electrodes along the y-axis of SLITs is one strategy for generating significantly more control. For example, electric fields from additional supplemental electrodes could be used to move packets of ions up and down along the y-axis, inducing collisions with neutral buffer gases and effecting CID. Due to the excitation being along the length axis, the pseudopotential well depth in the z-axis would no longer be a defining limitation,

and CID efficiency could be improved with this method. With different voltages applied to the various supplemental electrodes along the y-axis, it would also be possible to store separate packets of ions in different regions of the trap. This lateral ion separation would effectively create a SLIT array with the only barrier between the elements being electric fields. In this fashion, all elements could use the same drive RF on the ring electrode, but could also be arbitrarily adjusted in length or merged as needed. One advantage from an array would come from using multiple ion sources with different species. With the flexibility of these array structures, the differentiated ion packets could be controllably mixed for ion-ion reactions in the gas phase, which has been a promising field of study for many years.⁸⁻¹⁰ Furthermore, the advantages from adding multiple supplemental electrodes within the SLIT geometry are not expected to be limited to high pressure, and their use could expand to conventional laboratory settings as well.

Lastly, traditional GCs are bulky and power-hungry, primarily due to heating requirements of the oven. The development of miniature gas chromatography using microelectromechanical system (MEMS) technology has been an area of research for a number of years.¹¹ These devices typically etch GC columns into silicon wafers, which can then be coated with stationary phases suitable for gas separations on the order of 30 seconds. To that end, work has begun in this lab towards developing appropriate miniaturized gas chromatography components for coupling with a portable HPMS system. With these microfabricated columns and heaters, it is possible to create small, low-power devices that are ideal for portable instrumentation. The successful coupling demonstrated here between the HPMS with a commercial GC suggests that the coupling of the HPMS with a MEMS GC is feasible.

5.3 REFERENCES

1. Blakeman, K.H., et al., *High pressure mass spectrometry of volatile organic compounds with ambient air buffer gas*. Rapid Communications in Mass Spectrometry, 2017. **31**(1): p. 27-32.
2. Blakeman, K.H., et al., *High Pressure Mass Spectrometry: The Generation of Mass Spectra at Operating Pressures Exceeding 1 Torr in a Microscale Cylindrical Ion Trap*. Analytical Chemistry, 2016. **88**(10): p. 5378-5384.
3. Johnson, J.V., et al., *Tandem-in-space and tandem-in-time mass spectrometry: triple quadrupoles and quadrupole ion traps*. Analytical Chemistry, 1990. **62**(20): p. 2162-2172.
4. Todd, J.F.J., G. Lawson, and R.F. Bonner, *CHAPTER VIII - QUADRUPOLE ION TRAPS A2 - DAWSON, PETER H*, in *Quadrupole Mass Spectrometry and its Applications*. 1976, Elsevier. p. 181-224.
5. Chernookiy, D., *Optimization of the Cylindrical Ion Trap Geometry for Mass Analysis at High Pressure*. Dissertation, University of North Carolina at Chapel Hill, 2016.
6. Dawson, P.H. and N.R. Whetten, *Non-linear resonances in quadrupole mass spectrometers due to imperfect fields I. The quadrupole ion trap*. International Journal of Mass Spectrometry and Ion Physics, 1969. **2**(1): p. 45-59.
7. Blakeman, K.H., *Development of High Pressure Mass Spectrometry for Handheld Instruments*. Dissertation, University of North Carolina at Chapel Hill, 2015.
8. McLuckey, S.A. and T.-Y. Huang, *Ion/Ion Reactions: New Chemistry for Analytical MS*. Analytical Chemistry, 2009. **81**(21): p. 8669-8676.
9. McLuckey, S.A., G.E. Reid, and J.M. Wells, *Ion Parking during Ion/Ion Reactions in Electrodynamic Ion Traps*. Analytical Chemistry, 2002. **74**(2): p. 336-346.
10. Xia, Y., et al., *Mutual storage mode ion/ion reactions in a hybrid linear ion trap*. Journal of the American Society for Mass Spectrometry, 2005. **16**(1): p. 71-81.
11. Haghighi, F., Z. Talebpour, and A. Sanati-Nezhad, *Through the years with on-a-chip gas chromatography: a review*. Lab on a Chip, 2015. **15**(12): p. 2559-2575.